

1

Flow Research Report No. 470

Sponsored by  
Defense Advanced Research Projects Agency (DoD)  
Defense Small Business Innovation Research Program

AD-A206 360

**AN INVESTIGATION OF V/STOL JET INTERACTIONS  
IN A CROSSFLOW  
- FINAL REPORT -**

**Suresh Menon, Principal Investigator**

ARPA Order No.  
Issued by U.S. Army Missile Command Under  
Contract # DAAH01-88-C-0865  
Contract Period: 26 September 1988 through 30 March 1989

February 1989

Approved for Public Release;  
Distribution Unlimited

The views and conclusions contained in this document are those of the authors and should not be interpreted as representing the official policies, either expressed or implied, of the Defense Advanced Research Projects Agency or the U.S. Government.

**FLOW RESEARCH, INC.**  
21414 - 68th Avenue South  
Kent, Washington 98032  
(206) 872-8500

**DTIC**  
**ELECTE**  
APR 05 1989  
S C H D

89 1 01 001



89APMD-6007  
March 29, 1989

Commander  
U.S. Army Missile Command  
ATTN: AMSMI-RD-DP-TT/Mr. Hugh Carson  
Redstone Arsenal, AL 35898-5244

Reference: Submittal of Phase I Final Report on "An Investigation of V/STOL  
Jet Interactions in a Crossflow" Contract No. DAAH01-88-C-0865

Dear Mr. Carson:

Enclosed please find one copy of the revised Phase I Final Report on the above-mentioned contract. The requested revisions have been made, and the report has been distributed per the contract requirements. Also included is a DD Form 250.

Please feel free to call me at (206) 872-8500 if you have any questions.

Sincerely,

A handwritten signature in cursive script, appearing to read "Suresh Menon".

Suresh Menon  
Senior Research Scientist

SM:bb

Enclosures

cc: Commander, U.S. Army Missile Command, AMSMI-RD-CS-R  
Commander, U.S. Army Missile Space and Intelligence Center, AIAMS-YDL  
Commander, U.S. Army Missile Command, AMSMI-RD-RE  
Director, Defense Advanced Research Projects Agency, ASTO/Gertsma  
Director, Defense Advanced Research Projects Agency, TIO  
Defense Technical Information Center, DTIC-DDR

**Flow Research, Inc.**

AD-A206 360

Form Approved  
OMB No 0704-0188

REPORT

INGS

1a. REPORT SECURITY CLASSIFICATION Unclassified		3. DISTRIBUTION/AVAILABILITY OF REPORT Approved for Public Release; Distribution Unlimited	
2a. SECURITY CLASSIFICATION AUTHORITY		5. MONITORING ORGANIZATION REPORT NUMBER(S)	
2b. DECLASSIFICATION/DOWNGRADING SCHEDULE		7a. NAME OF MONITORING ORGANIZATION DCASMA, Seattle	
4. PERFORMING ORGANIZATION REPORT NUMBER(S) Flow Research Report Number 470		7b. ADDRESS (City, State, and ZIP Code) Bldg. 5D Naval Station Seattle, Washington 98115-5010	
6a. NAME OF PERFORMING ORGANIZATION Flow Research, Inc.	6b. OFFICE SYMBOL (If applicable)	9. PROCUREMENT INSTRUMENT IDENTIFICATION NUMBER Contract No. DAAH01-88-C-0865	
6c. ADDRESS (City, State, and ZIP Code) 21414 - 68th Avenue South Kent, Washington 98032		10. SOURCE OF FUNDING NUMBERS	
8a. NAME OF FUNDING/SPONSORING ORGANIZATION U.S. Army Missile Command	8b. OFFICE SYMBOL (If applicable) W31P4Q	PROGRAM ELEMENT NO.	PROJECT NO.
8c. ADDRESS (City, State, and ZIP Code) AMSMI-PC-BFA Redstone Arsenal, AL 35898-5280		TASK NO.	WORK UNIT ACCESSION NO.
11. TITLE (Include Security Classification) An Investigation of V/STOL Jet Interactions in a Crossflow (Unclassified)			
12. PERSONAL AUTHOR(S) Suresh Menon			
13a. TYPE OF REPORT Final Report	13b. TIME COVERED FROM 9/26/88 TO 3/30/89	14. DATE OF REPORT (Year, Month, Day) 1989, March	15. PAGE COUNT 70
16. SUPPLEMENTARY NOTATION			
17. COSATI CODES		18. SUBJECT TERMS (Continue on reverse if necessary and identify by block number)	
FIELD	GROUP	V/STOL Aerodynamics, Impinging Jets, Large-Eddy Simulation, Unsteady Flow, Ground Effect, Moving Ground, Crossflow, Oblique Impingement, Moving Ground	
19. ABSTRACT (Continue on reverse if necessary and identify by block number) The fluid dynamics of the flow field generated by a V/STOL aircraft in ground effect is very complex. To optimize the design of these aircraft and to predict their performance in ground effect requires a good understanding of the impinging jet-induced flow field. Presently, experimental studies are the main avenue followed to understand V/STOL flows. However, it is quite difficult to obtain detailed measurements in the flow field since the flow is turbulent, globally unsteady, and highly three-dimensional. Numerical simulation provides an opportunity to study the detailed flow physics as a function of space and time. Due to current computer limitations, the complete flow field around a V/STOL aircraft in ground effect is still difficult to solve. However, some flow domains, such as the impinging jet flow, can be studied. Furthermore, numerical simulations have the advantage of providing information on flow properties that are quite difficult to measure experimentally, such as the instantaneous pressure field in turbulent flows and vorticity in the shear layers. Thus, numerical simulations can complement experimental investigations and may provide a computational tool to understand the dynamics of the V/STOL flow fields. (cont. on next page)			
20. DISTRIBUTION/AVAILABILITY OF ABSTRACT <input checked="" type="checkbox"/> UNCLASSIFIED/UNLIMITED <input type="checkbox"/> SAME AS RPT. <input type="checkbox"/> DTIC USERS		21. ABSTRACT SECURITY CLASSIFICATION Unclassified	
22a. NAME OF RESPONSIBLE INDIVIDUAL Hugh C. Carson		22b. TELEPHONE (Include Area Code) (205) 876-7215	22c. OFFICE SYMBOL

**19. Abstract (cont.)**

Recently, a numerical simulation code was developed to study the interaction of the effects of a row of normal impinging jets. This model essentially simulates the hovering configuration of a V/STOL aircraft. The numerical code solves the unsteady, three-dimensional incompressible Navier-Stokes equations using the technique of large-eddy simulations, which resolves all the length scales above the grid resolution and models the contribution of the small scales by a subgrid eddy viscosity model. Using both coherent (axisymmetric and azimuthal) and random excitation of the impinging jet, the evolution of the large-scale structures in the flow field was investigated and the results were shown to agree quite well with experimental data.

In the present Phase I study, this numerical code was extended to include other realistic V/STOL configurations, such as an obliquely impinging jet and an impinging jet in crossflow with and without a moving ground plane. These configurations model the V/STOL aircraft in pitch and in forward motion. These modifications were successfully achieved and preliminary simulations using axisymmetric forcing of the impinging jet were carried out to demonstrate the capability of the numerical code. Even with the coarse mesh (and thus low Reynolds number) simulations, the results show good qualitative agreement with experimental observations. For example, the oblique impinging jet simulation showed that a significant portion of the jet flow is carried in the forward direction and the stagnation point on the ground plane is offset from the jet centerline. The shift in the stagnation point from its location for a normal impinging jet was determined to agree quite well with experimental observations, and the presence of vorticity in the oblique stagnation streamline was demonstrated which also agrees with past observations. The upwash fountain resulting from the collision of the wall jets on the ground is skewed in the forward direction due to the obliqueness of the impinging jets. This would result in a nonuniform pressure on the undersurface of the V/STOL aircraft and thus cause a nonuniform lift-off effect.

The simulation of the impinging jet in crossflow showed the formation of the counterrotating streamwise vortices, which has been observed in many experiments. However, it was shown that the presence of the adjacent impinging jet (which is absent in all experiments) can significantly modify the dynamics of the vortical motion in the flow field. Significant, three-dimensional vortex stretching occurs in this flow and the redistribution of the total vorticity in the flow field occurs in a complex manner. The simulation with the ground plane moving at the same velocity as the crossflow results in the elimination of the wall boundary layer. As a consequence, the size and the structure of the vortex ahead of the impinging jet is drastically reduced, which is similar to experimental observations.

The results presented in this Phase I study indicate that the primary technical objectives of the study were successfully achieved and a numerical simulation capability now exists that can be utilized to understand the dynamics of a variety of flight configurations of the V/STOL aircraft in ground effect in a systematic manner. This simulation code can complement experimental studies of such flow fields and may help in optimizing the design and performance of V/STOL aircraft.

## TABLE OF CONTENTS

LIST OF FIGURES	iv
1. INTRODUCTION	1
2. PHASE I TECHNICAL OBJECTIVES	4
3. NUMERICAL MODEL	5
3.1 Governing Equations	5
3.2 Boundary Conditions	7
3.2.1 Normal Impinging Jet	7
3.2.2 Modifications to Model an Inclined Impinging Jet	7
3.2.3 Modifications to Model Normal Impinging Jets in Crossflow	8
3.2.4 Modifications to Model Crossflow with Moving Ground Plane	8
3.3 Numerical Method	8
4. APPROACH TO NUMERICAL SIMULATIONS	11
4.1 Relevance of Grid Resolution	11
4.2 Initialization	12
4.2.1 Steady-State Profile	12
4.2.2 Coherent Forcing	13
5. RESULTS OF SIMULATIONS	14
5.1 The Oblique Impinging Jet	14
5.2 The Normal Impinging Jet without Crossflow	27
5.3 The Normal Impinging Jet in Crossflow	31
5.3.1 Forward Motion after Hovering	31
5.3.2 Forward Motion without Hovering	38
5.4 The Normal Impinging Jet in Crossflow with Moving Ground Wall	48
6. CONCLUSIONS AND RECOMMENDATIONS	60
REFERENCES	63



Accession For	
NTIS GR&I	<input checked="" type="checkbox"/>
DTIC TAB	<input type="checkbox"/>
Unannounced	<input type="checkbox"/>
Justification	
By	
Date	
Availability Codes	

A-1

## LIST OF FIGURES

Figure 1.	Schematic of an array of three-dimensional impinging jets	6
Figure 2.	The inclined impinging jet and the impinging jet in crossflow	9
Figure 3.	Three-dimensional perspective of the total vorticity $ \omega $ in the inclined impinging jet for the unforced case.	15
Figure 4.	Time sequence of the propagation of the starting vortex in the inclined impinging jet.	15
Figure 5.	Time sequence of the propagation of the starting vortex in the inclined impinging jet.	17
Figure 6.	Three-dimensional perspective of the total vorticity $ \omega $ in the inclined impinging jet at the end of six forcing cycles.	18
Figure 7.	Time sequence of the $x$ -vorticity contours in the $y$ - $z$ plane at $x = 0$ for the last forcing cycle.	19
Figure 8.	Time sequence of the $y$ -vorticity contours in the $x$ - $z$ plane at $y = 0$ for the last forcing cycle.	21
Figure 9.	Comparison of the velocity vector fields, pressure gradient, and pressure contours in the $y$ - $z$ plane at $t = 24.375$ .	22
Figure 10.	Velocity vector fields in the $y$ - $z$ plane at $t = 24.375$ .	24
Figure 11.	Pressure contours in the $x$ - $y$ plane at $t = 24.375$ .	24
Figure 12.	Velocity profiles in the flow field.	25
Figure 13.	Pressure variation on the ground plane.	26
Figure 14.	Three-dimensional perspective of the total vorticity $ \omega $ for the normal impinging jet.	29
Figure 15.	Vorticity contour fields for the normal impinging jet at $t = 9.4$ .	29
Figure 16.	Velocity vector fields for the normal impinging jet at $t = 9.4$ .	30
Figure 17.	Pressure contours in the $x$ - $y$ plane at $t = 9.4$ .	30
Figure 18.	Three-dimensional perspective of the vorticity fields for the normal impinging jet with crossflow (case A) at $t = 13.1$ .	32
Figure 19.	Vorticity contour fields for normal impinging jet with crossflow (case A) at $t = 13.1$ .	34
Figure 20.	Velocity vector fields and pressure contours for the normal impinging jet with crossflow (case A) at $t = 13.1$ .	35

## LIST OF FIGURES (cont.)

Figure 21. Comparison between velocity profiles in the flow field for the normal impinging jet at $t = 9.4$ and the normal impinging jet with crossflow at $t = 13.1$ .	37
Figure 22. Vorticity fields for the normal impinging jet with crossflow (case B) at $t = 3.8$ .	39
Figure 23. Velocity vector fields in the $y$ - $z$ plane for normal impinging jet with crossflow (case B) at $t = 3.8$ .	40
Figure 24. Three-dimensional perspective of the vorticity for normal impinging jet with crossflow (case B) at $t = 13.1$ .	42
Figure 25. Vorticity contours in the flow field for the forced normal impinging jet with crossflow (case B).	43
Figure 26. Velocity vector field in the flow field for the forced normal impinging jet with crossflow (case B).	45
Figure 27. Pressure contours in the flow field for the forced normal impinging jet with crossflow (case B).	47
Figure 28. Velocity profiles in the flow field for the forced normal impinging jet with crossflow (case B).	49
Figure 29. Ground pressure variation for the forced normal impinging jet with crossflow (case B).	50
Figure 30. Three-dimensional perspective of the vorticity field for the normal impinging jet with crossflow and with moving ground plane at $t = 13.1$ .	52
Figure 31. Vorticity and velocity fields in the $y$ - $z$ plane for the normal impinging jet with crossflow and with moving ground plane at $t = 13.1$ .	53
Figure 32. Vorticity and velocity fields in the $x$ - $z$ plane for the normal impinging jet with crossflow and with moving ground plane at $t = 13.1$ .	54
Figure 33. Pressure contours in the $x$ - $y$ plane for the normal impinging jet with crossflow and with moving ground plane at $t = 13.1$ .	57
Figure 34. Comparison between the velocity profiles for the cases with and without the moving ground plane for the normal impinging jet with crossflow at $t = 13.1$ .	58
Figure 35. Comparison between the ground pressure variation for the cases with and without moving ground plane for the normal impinging jet with crossflow at $t = 13.1$ .	59

## 1. INTRODUCTION

The fluid dynamics of impinging jets associated with vertical/short takeoff and landing (V/STOL) aircraft operating near the ground is very complex. An impinging jet flow field is a combination of free jet flow, vortical flow in curved shear layers, stagnation point flow, and wall jet flow. In addition, the effects of compressibility, hot gas exhaust, and heat transfer, as well as complex interactions between the airframe and the ground, can complicate the flow field. The complexity of the flow field is further compounded when the aircraft is in forward motion near the ground and also when the aircraft executes a pitch-up or pitch-down motion during transition in and out of ground effect. Clearly, an accurate prediction of the aerodynamic forces and moments on the aircraft is not possible without understanding the associated flow physics.

The flow fields associated with the various operating modes of V/STOL aircraft, such as hovering and transition in and out of ground effect, are quite different from each other. Many of the complex phenomena associated with these flow fields are poorly understood, thereby restricting our ability to optimize the aircraft design. For example, lifting jets entrain air, which leads to induced suction pressures on the aircraft undersurface. When the aircraft is hovering near the ground, further entrainment is caused by the wall jets. This significantly increases the suckdown force on the aircraft. The problem becomes more complicated when there are multiple jets interacting near the ground, as with the exhausts of a twin-engine V/STOL aircraft. The wall jets caused by the impinging jets collide and form an upwash or a fountain that impinges on the aircraft undersurface. This upwash creates an upload that partially offsets the suckdown force. In actual flight conditions, however, the upwash of the hot jet exhaust will create other problems such as hot gas ingestion by the engine intakes and aircraft skin damage caused by the corrosive effect of the hot combustion products in the exhaust and by the entrainment of ground surface particles by the wall jets. In general, the complex flow field associated with multiple jets in ground effect is not very well understood.

Most of the research that has been directed toward understanding V/STOL-related flow fields has been experimental.<sup>1-5</sup> Such studies, however, addressed mostly global features and time-averaged measurements. Measurements in the flow field associated with impinging jets is extremely difficult due to the high levels of turbulence in the globally unsteady three-dimensional flows. Characterization of these flows would require measurements using three-dimensional arrays of sensors, such as hot wire sensors, which are limited by the fact that they cannot discriminate flow reversal from forward flow and/or are prone to probe interference. Thus, it is clear that measurements in the flow field of three-dimensional impinging jets will require new measurement techniques such as double-pulse holography or scanning two-color LDA, which are currently being developed.

Numerical simulation provides an opportunity to study the detailed flow physics as a function of space and time. Although the complete flow field around a V/STOL aircraft cannot yet be resolved adequately, state-of-the-art supercomputers can be used to study some local flow domains such as the impinging jet. In addition, numerical simulation has the additional advantage of providing the instantaneous distribution of all the flow variables over the entire computational domain. Thus, it allows "measurements" of flow properties not possible experimentally, and can provide simultaneous "flow visualization" and "measurements" in arbitrary planes. Furthermore, numerical simulation allows independent control of flow parameters such as initial condition, free stream turbulence, and excitation frequency and amplitude. These parameters can be more easily introduced and controlled in a numerical simulation than in laboratory experiments.

In this Phase I study, we investigated the configurations of a V/STOL aircraft in pitch while hovering and in forward motion during takeoff and transition. The dynamics of the flow in the fountain caused by the collision of the wall jets will be affected by the orientation of the impinging jet and also by the forward motion of the aircraft. The consequent changes in the lift-off effect on the V/STOL aircraft can be quite significant. A detailed understanding of the dynamics of the flow field is essential to optimize the design of the aircraft. To study the complex flow field associated with this configuration in ground effect, a numerical simulation technique must be developed that can be used to understand the physics of the flow. The demonstration of such a numerical predictive capability was the primary objective of this Phase I study.

In the past, extensive experimental and numerical studies of normal impinging jets have been carried out.<sup>3,5-10</sup> Studies of inclined impinging jets have also been carried out in the past.<sup>5, 11-13</sup> The earliest work by Taylor<sup>14,15</sup> was an analytical and experimental study of an oblique impinging jet. He showed that for two-dimensional impinging jets, the maximum (stagnation) pressure at the impingement point is the same for all angles of incidence but that the area over which the high pressure acts, as well as the downward force exerted on the plate, are reduced significantly as the angle becomes small. He also developed analytical expressions for the amount of mass that is transported in the downstream direction. Later experimental study by Donaldson and Snedeker<sup>5</sup> of normal and oblique impinging jets provided data on the mean flow characteristics such as velocity and pressure. They also determined the azimuthal distribution of the wall jet and showed that the mass and momentum flux is concentrated near the centerplanes but is skewed depending upon the angle of incidence. The stagnation streamline is also offset from the jet physical centerline due to oblique impingement.

In numerical studies, Rubel<sup>16,17</sup> investigated the oblique impingement of jets using an inviscid, rotational flow model formulated in terms of vector and scalar potentials and the vector vorticity. He showed that the oblique impingement of a round jet creates a fully three-dimensional flow field for which a streamfunction formulation is inappropriate. It was also shown that whereas normal impingement of a jet produces a stagnation line with zero vorticity, the oblique impingement of the jet results in a shift in the stagnation line and as a consequence, the stagnation streamline becomes rotational. In an earlier study, Hayes<sup>18</sup> showed that in the vicinity of a nearly axisymmetric rotational stagnation region, the vorticity exhibits an inverse square root variation with the vertical distance. The numerical computations agreed with this prediction.

Numerical and experimental studies of jets in crossflow have been going on for a long time<sup>1,4,19-25</sup> due to a wide variety of engineering applications for this type of flow. Examples of practical applications include film cooling of turbine blades, transverse fuel injection in combustors, pollutant dispersal from smoke stacks, and V/STOL aircraft in ground effect. Most of the above-mentioned studies concerned the effects of free jets in crossflow, although their relevance to V/STOL applications are quite clear. Recently, a numerical study of an impinging jet in crossflow was carried out using a QUICK scheme.<sup>26</sup> However, this investigation focused on a very weak crossflow and thus does not give a complete picture of the flow field. This is due to the fact that the dynamics of the jet interaction with a crossflow depends quite significantly on the ratio of the jet velocity to the crossflow velocity.<sup>4</sup>

In all the experimental studies mentioned above, the crossflow toward the jet was generated in a wind tunnel with a fixed ground plane. However, to model a realistic V/STOL aircraft in forward motion, the ground plane should also be in relative motion. Thus, the effect of a moving ground plane must be understood before the experimental data can be correlated with actual flight data. Recent experiments<sup>27,28</sup> have studied the effect of a moving ground plane either by using a moving ground

belt or by moving the impinging jet itself. These studies clearly showed that there are significant differences between the flow fields around an impinging jet when the ground is fixed and when it is moving. For example, it was shown that the vortex strength ahead of the jet is reduced by as much as 50 percent in lateral penetration when the ground is moving, due to the elimination of the wall boundary layer. In addition, actual flight test data indicates that there is less lift increase during approach and landing than that determined from wind-tunnel measurements with a fixed ground plane. To evaluate these differences experimentally is quite difficult and expensive since special test facilities are required to simulate the moving ground plane. However, studying the effect of motion of the ground plane computationally is a relatively simple matter and can be accomplished through appropriate modifications to the wall boundary conditions. Numerical investigation of this configuration of a V/STOL aircraft in forward motion has not been carried out before. The results presented in this report appear to be the first attempt to model the effect of a moving ground plane.

In this Phase I study, a numerical investigation of oblique impinging jets and impinging jets in crossflow with and without a moving ground plane has been carried out. This involved the modification of a three-dimensional Navier-Stokes solver that was recently developed to study impinging jets.<sup>9,10</sup> The problem considered in our previous investigations contained the essential features of twin jets impinging normally on the ground, simulating the hovering configuration of a V/STOL aircraft. The computer code solves the unsteady three-dimensional incompressible Navier-Stokes equations using the technique of large-eddy simulation (LES). The technique of LES is well known and has been used to study various types of flow fields in the past. In terms of computational accuracy, this technique lies between the Reynolds-Averaged Navier-Stokes (RANS) and the direct numerical simulations (DNS) techniques. The RANS technique essentially solves the time-averaged Navier-Stokes equations using turbulence modeling to include the effect of turbulent fluctuations. This approach does not take into account the wide variation in the length scales in the turbulent flow field and only a global steady-state solution can be obtained. In contrast, the DNS technique attempts to resolve all the length scales in the flow field and uses no modeling. Temporal as well as spatial accuracy is maintained in the DNS simulations. Even with state-of-the-art supercomputers, however, only a few orders of length scales can be resolved and thus the DNS technique is limited to very low Reynolds numbers. On the other hand, the technique of LES resolves all the length scales above the grid resolution using a time- and space-accurate numerical scheme, and the contribution of scales smaller than the grid resolution are modeled by prescribing a sub-grid eddy viscosity model that characterizes the energy cascade into the unresolvable scales. In principle, given a reasonable grid resolution, relatively high Reynolds number flows can be studied using the LES technique.

The application of the LES technique to V/STOL-related flow fields as described in the previous investigations<sup>9,10</sup> was the first attempt to use LES to study this type of complex flow field. In these studies, the dynamics of the evolution and the propagation of large coherent structures in the impinging jet shear layer and in the wall-bounded jet was studied in detail. The effect of introducing a disturbance at the jet exit plane on the evolution of the coherent structures was determined. The effects of axisymmetric, azimuthal, and random perturbation were investigated.<sup>9,10,29</sup> Good agreement with experimental data was obtained, as described earlier.<sup>9,10</sup>

In this study, some modifications to the basic LES code were necessary to model an obliquely impinging jet and an impinging jet in crossflow with and without a moving ground plane. These modifications were successfully accomplished and some numerical simulations were carried out to demonstrate the capability of the modified LES code. This report documents the findings of this study.

## 2. PHASE I TECHNICAL OBJECTIVES

The primary technical objectives of this Phase I study are given below:

- Modify the existing three-dimensional code to numerically simulate inclined impinging jets.
- Modify the code to numerically simulate impinging jets in a crossflow with and without a moving ground plane.
- Demonstrate the capability of the numerical code to simulate inclined impinging jets and impinging jets in a crossflow.

As discussed in the following sections, these Phase I objectives were successfully achieved.

### 3. NUMERICAL MODEL

The numerical code used in this study was originally designed to solve the problem of a row of jets impinging vertically from a horizontal plate onto a ground plane. Before presenting the details of the modifications required for this Phase I study, we will briefly describe the basic numerical scheme.

#### 3.1 Governing Equations

The governing equations of the numerical scheme are the three-dimensional, incompressible Navier-Stokes equations and the continuity equation. Following classical LES approach, the flow variables are decomposed into a large-scale, resolvable part and a subgrid-scale, unresolvable part. The equation governing the large-scale motion is obtained by applying a cell-volume averaging to the Navier-Stokes equations and to the continuity equation. The resulting equations are

$$\bar{q}_t + \nabla \cdot [\bar{q}\bar{q}^T - 2(\nu + \nu_s)\bar{S}] = -\nabla P \quad (1)$$

and

$$\nabla \cdot \bar{q} = 0 \quad (2)$$

where  $\bar{q}$  is the resolvable part of the velocity,  $\bar{S}$  is the rate-of-strain tensor, and  $\nu$  is the kinematic viscosity. Here, the subscript  $t$  denotes differentiation with respect to time. The continuity equation [Equation (2)] is then replaced by a Poisson's equation for the "modified" pressure  $P$ , which now contains the terms appearing due to the volume averaging:

$$\nabla^2 P = -\nabla \cdot \bar{q}_t - \nabla \cdot \bar{Q} \quad (3)$$

where

$$\bar{Q} = \nabla \cdot [\bar{q}\bar{q}^T - 2(\nu + \nu_s)\bar{S}] \quad (4)$$

and

$$\nabla \cdot \bar{q}_t = 0 \quad (5)$$

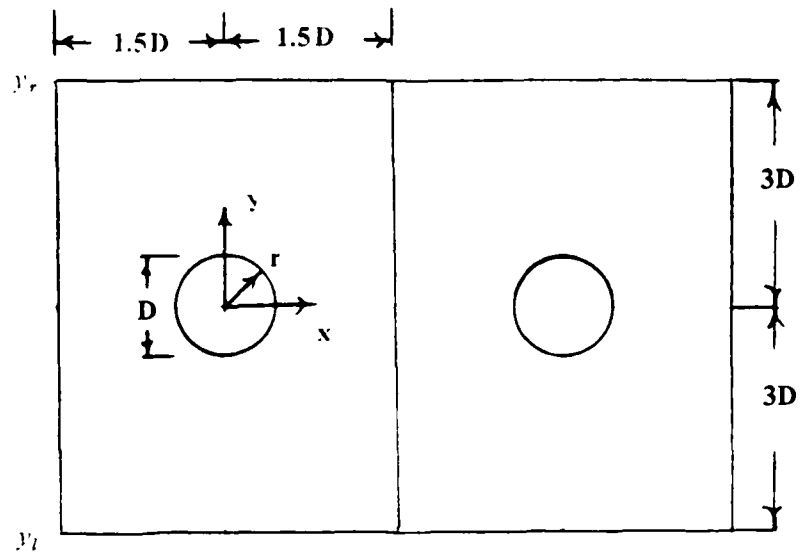
The system of Equations (1) and (4) is equivalent to the original system of Equations (1) and (2) and is used here in place of the original system.

It is assumed that the small-scale structures are universal in character, contain little energy, and are dissipative in nature. A subgrid-scale eddy viscosity,  $\nu_s$ , is defined to model the cascade of energy from the large scale to the small scale, where it is dissipated. The form of the eddy viscosity is similar to the model used by Smagorinsky<sup>30</sup> and Deardorff<sup>31</sup> and is given as

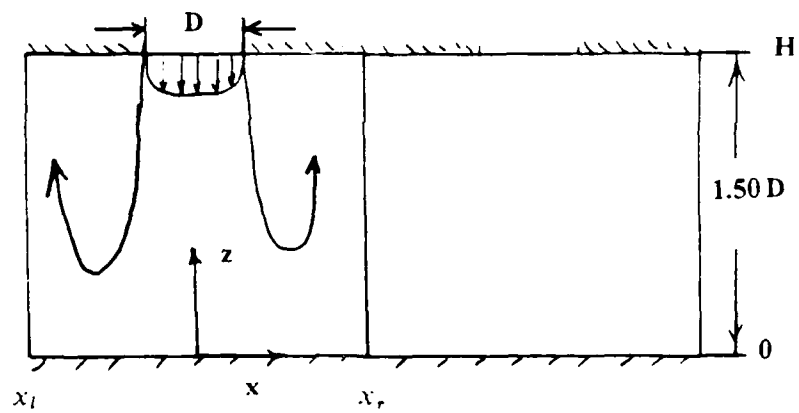
$$\nu_s = (C_1 \Delta)^2 (2S_{ij}S_{ij})^{1/2} \quad (6)$$

where  $C_1$  is a constant and  $\Delta$  is the characteristic length scale of the smallest resolvable eddies. In the present simulations,  $C_1 = 0.1$ , which is the value chosen by Deardorff.<sup>31</sup>

The physical problem investigated in these simulations is an infinite row of impinging jets. Each jet exits from a circular nozzle of diameter  $D$  in a horizontal plate that is parallel to the ground and at a distance  $H$  above it. This plate models the undersurface of the V/STOL aircraft. Figures 1a and 1b show the top and side views, respectively, of the normal impinging jet. A Cartesian frame of reference,  $\vec{x} = (x, y, z)$ , is defined as shown, with the velocities in each coordinate direction defined as  $\vec{q} = (u, v, w)$ .



a. Top view



b. Side view

Figure 1. Schematic of an array of three-dimensional impinging jets.

### 3.2 Boundary Conditions

The filtered Navier-Stokes equations, Equations (1) and (4), are solved subject to appropriate boundary conditions. By virtue of the assumption of an infinite row of impinging jets, periodic boundary conditions are imposed at the boundaries  $x = x_l$  and  $x = x_r$  (see Figure 1). Even when a high-resolution grid is used,<sup>9,10</sup> it is still not fine enough to resolve the viscous sublayer adjacent to the top and bottom walls. Therefore, the solution in the near wall region is patched to the solution at the first computational cell next to the wall by using Spalding's law of the wall.<sup>32</sup> The vertical velocity component ( $w$ ) is specified as zero at both the upper and lower boundaries, except at the jet exit where it is specified as a function of space and time. The other two velocity components ( $u$ ,  $v$ ) are specified as zero at the jet exit.

If there is a crossflow present, the boundary conditions at the outflow boundaries (i.e.,  $y = y_l$  and  $y = y_r$ ) must be modified. For oblique impingement, the conditions at the jet exit plane also must be modified. These differences are highlighted in the following sections.

#### 3.2.1 Normal Impinging Jet

The outflow boundaries at  $y = y_l$  and  $y = y_r$  are artificial boundaries used to limit the computational domain to a finite region. Since the boundary conditions at these locations are not known, approximate boundary conditions are imposed. Zero derivatives for the velocity components  $u$  and  $w$  are imposed at these boundaries (i.e.,  $\partial u/\partial y = 0$ ,  $\partial w/\partial y = 0$ ) and the derivative  $\partial v/\partial y$  was determined from the continuity equation. To solve the Poisson's equation for pressure, Neumann boundary conditions were used on all boundaries. At the top and bottom walls, these conditions were defined by the  $y$ -momentum equation. At the outflow boundaries,  $\partial P/\partial y = 0$  was imposed. However, in some earlier calculations, this weak boundary condition allowed a continuous, nonphysical buildup of the inflow velocity in certain regions of the boundary. The pressure gradient at the outflow boundaries was modified to limit this build up. Also, the existence of a solution to the Poisson's equation for pressure with Neumann boundary conditions requires that the integral over the computational domain of the source terms in that equation be equal to the integral of  $\partial P/\partial n$  over the boundaries, where  $n$  is the outward normal at the boundaries. To satisfy this condition, the value of  $\partial P/\partial n$  was uniformly modified at the outflow boundaries.

Note that these modifications to the pressure at the outflow are not required when there is a crossflow present. With a crossflow, the zero derivative for the pressure mentioned above is used without any condition to limit the inflow velocity since there is no reverse flow at the outflow boundaries.

#### 3.2.2 Modifications to Model an Inclined Impinging Jet

To simulate an obliquely impinging jet, some modifications of the boundary conditions at the jet exit plane were required. In our earlier study, the horizontal velocity components  $u$  and  $v$  were both specified as zero in the plane of the jet exit. To simulate an inclined jet, a nonzero velocity component  $v$  in the  $y$ -direction must be imposed. The required modification is described below.

First, an axial velocity distribution at the circular jet exit of a noninclined jet is specified. We assume that this circular jet is inclined in the  $y$ -direction such that the upper horizontal computational boundary will intersect the jet circular cylinder in an elliptical cross section with its major and minor axes in the  $y$ - and  $x$ -directions, respectively. Figure 2a shows a schematic of this configuration. At the computational mesh points, which fall within this ellipse, the original axial velocity component may now be decomposed into its  $y$ - and  $z$ -components. This velocity distribution is then specified at the jet exit plane and thus simulates the case of an inclined impinging jet.

### 3.2.3 Modifications to Model Normal Impinging Jets in Crossflow

To simulate the effect of crossflow, further modifications to the code were required. We assumed the crossflow to be specified in the positive  $y$ -direction, normal to the plane of the jet axes. To simulate the case of forward motion of the V/STOL aircraft in the negative  $y$ -direction at a given velocity  $v = v_0$ , a positive velocity  $v_0$  in the  $y$ -direction is first imposed on the flow and the boundary so that the problem can be solved in a reference frame in which the aircraft is fixed (see Figure 2b). The governing equation for this case remains unchanged except for the case in which the aircraft is accelerating or decelerating. In this case, there is an additional term,  $dv_0/dt$ , which appears in the  $y$ -momentum equations. While the case of an accelerating (or decelerating) aircraft is of general interest, we did not go into the details of these unsteady effects in this Phase I study. However, the code modification was carried out to include this unsteady term, so that an option exists to study forward acceleration or deceleration while in forward motion. In the present study, this option was used to ramp up the initial transitional period in which the crossflow builds from an initial value of zero to its final desired value.

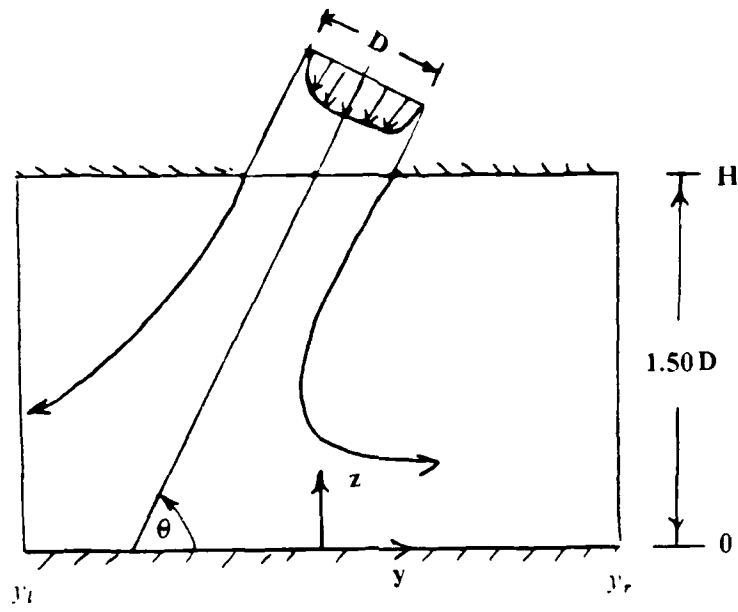
### 3.2.4 Modifications to Model Crossflow with Moving Ground Plane

As mentioned earlier, it is of great interest from an experimental point of view to compare the results of impinging jets in crossflow with a moving ground plane to those with a fixed ground plane. For the case of an impinging jet with crossflow over a fixed ground plane, the modifications described above are applicable. For the case with a moving ground plane, in the reference frame of a fixed aircraft, the ground plane will also move in the positive  $y$ -direction with the velocity  $v = v_0$  (see Figure 2b). This modification has also been successfully accomplished.

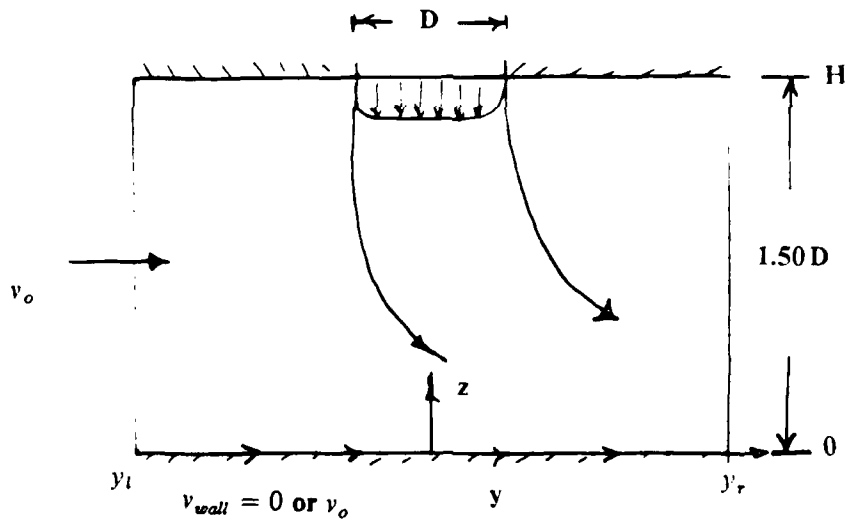
Although the above modifications for the inclined jet and the crossflow have been described separately, the boundary conditions for these configurations can be prescribed together without any problem. Thus, in principle, it is possible to model a V/STOL aircraft in pitch while in forward motion. This flight situation is also very interesting in that the dynamics of the flow field can be modified significantly due to the combined effect of the inclined impinging jet and the forward motion. These aspects of the flow can be studied in more detail in the next phase.

## 3.3 Numerical Method

The governing equations are solved using a staggered computational mesh which alleviates many of the difficulties associated with the solution of incompressible Navier-Stokes equations on a regular mesh. A brief description of the discretization of the various flow variables (i.e.,  $P$ ,  $u$ ,  $v$ , and  $w$ ) on a staggered mesh is given here.



a. The inclined impinging jet



b. The impinging jet in crossflow, with and without a moving ground plane

Figure 2. The inclined impinging jet and impinging jet in cross-flow.

The main computational mesh is the  $P$  mesh. The pressure is defined at the nodal points  $(x_i, y_j, z_k) = (i\Delta x, j\Delta y, k\Delta z)$  of this mesh, which is uniform in the three coordinate directions. The  $u$ -,  $v$ -, and  $w$ -velocity components are defined at the nodal points  $(x_{i+1/2}, y_j, z_k)$ ,  $(x_i, y_{j+1/2}, z_k)$  and  $(x_i, y_j, z_{k+1/2})$  of the  $u$ ,  $v$ , and  $w$  meshes, respectively. These meshes are displaced from the  $P$  mesh by half of one mesh spacing in the  $x$ -,  $y$ -, and  $z$ -directions, respectively. The  $x$ -,  $y$ -, and  $z$ -momentum equations are discretized at the nodal points of the  $u$ ,  $v$ , and  $w$  meshes, respectively, while the discretized Poisson's equation for pressure is obtained at the nodal points of the  $P$  mesh by central differencing of the discretized momentum equations at the neighboring points.

The pressure gradient terms and the diffusive terms of the momentum equations are approximated by central differencing. The use of central differencing to approximate the convective terms leads to nonphysical oscillations at relatively low Reynolds numbers and to divergence of the solution as the Reynolds number is increased. To avoid this problem, the convective terms of the momentum equations are discretized using a three-dimensional version of the QUICK scheme first developed for one-dimensional flows by Leonard<sup>33</sup> and then extended to two dimensions by Davis and Moore.<sup>34</sup> The details of the three-dimensional QUICK scheme used in the present code was described earlier<sup>9</sup> and thus will not be repeated here.

To advance the solution from time  $t^n$  to time  $t^{n+1}$ , where  $t^n = n\Delta t$  and  $\Delta t$  is the incremental time step, the Poisson's equation for pressure

$$\bar{\nabla}^2 P^{n+1/2} = \frac{\bar{\nabla} \cdot \bar{q}^{n+1}}{\Delta t} + \bar{\nabla} \cdot \left( \frac{\bar{q}^n}{\Delta t} - \bar{Q}^{n+1/2} \right) \quad (7)$$

is first solved to evaluate the pressure distribution that will allow the continuity equation to be satisfied at time  $t^{n+1}$ . Here,

$$\bar{Q}^{n+1/2} = \frac{3}{2}\bar{Q}^n - \frac{1}{2}\bar{Q}^{n-1} \quad (8)$$

and  $\bar{\nabla}$  is the central difference approximation of the operator  $\nabla$ . For the continuity equation to be satisfied at time  $t^{n+1}$ , it is necessary to set the first term on the right-hand side of Equation (7) equal to zero. An efficient method for direct solution of the discrete Poisson's equation is used. Once the pressure field is determined, an Adams-Bashforth time-stepping scheme is used to calculate the velocity at the next time level. Therefore,

$$\bar{q}^{n+1} = \bar{q}^n - \Delta t \left( \bar{Q}^{n+1/2} + \bar{\nabla} P^{n+1/2} \right) \quad (9)$$

The finite difference scheme used in these simulations is second-order accurate in both space and time.

#### 4. APPROACH TO NUMERICAL SIMULATIONS

In this study, the primary technical objectives were to implement the modifications to simulate inclined impinging jets and jets in crossflow, and to demonstrate the capability of the numerical scheme to study flow fields associated with such V/STOL flight configurations. Due to the resource and time constraints of the Phase I study, only representative simulations were performed to demonstrate the code's capabilities. As shown below, however, analysis of the computed solutions indicates interesting features that are in good qualitative agreement with past experimental observations.

The approach used in this study was to investigate the motion of large-scale coherent structures in the flow field. There are various reasons for using this approach. Large-scale coherent structures have been extensively observed in free jets<sup>35,36</sup> and in impinging jets.<sup>3</sup> These structures are formed when the unstable jet shear layer rolls up into vortices that pair or merge during their downstream propagation to form the large coherent structures. Due to three-dimensional effects, these structures eventually break down into small-scale turbulent flow. The formation of these structures occurs at a preferred frequency, often called the jet preferred mode, which lies in the Strouhal Number ( $St = fD/U$ ) range of 0.2 to 0.8.<sup>37</sup> It has become well known in recent years that these structures play a major role in the transport of momentum and in noise production.<sup>6</sup> There is also evidence that these structures play a major role in the entrainment process. This is particularly relevant to V/STOL aircraft operating near the ground since the vortical structures may entrain dust from the ground that may in turn be ingested into the engine intakes, possibly causing malfunctions. Understanding the dynamics of the evolution and motion of large-scale coherent structures in impinging jet flows is clearly important in optimizing the design of V/STOL aircraft.

In addition, the LES technique is uniquely suited to the study of the motion of coherent structures since these structures are usually much larger than the grid resolution and thus can be resolved by the numerical scheme. As mentioned earlier, only the scales smaller than the grid resolution need to be modeled, which can be accomplished by using a sub-grid model.

To study the motion of these coherent structures, the jet inflow velocity profile at the jet exit is perturbed by superposing prescribed disturbances. The resulting motion of the flow is then calculated using the LES code. This method of prescribing external excitation was very successful in our earlier studies of normal impinging jets.<sup>9,10,29</sup> In addition, the method of external forcing at a specified frequency suppresses the natural instability of the flow; hence, the dynamics of the coherent structure are controlled by the forcing frequency. This results in a "clean" numerical experiment. Externally excited flows have been studied extensively in the past, both in free jets<sup>35,38,39</sup> and in impinging jets,<sup>3</sup> to understand the dynamics of large-scale coherent motion.

##### 4.1 Relevance of Grid Resolution

To resolve all the relevant scales of motion associated with high Reynolds number flows, a very high grid resolution is required. In our earlier studies,<sup>9,10,29</sup> for example, grid resolutions on the order of 64 x 128 x 32 were used. Computations using such high resolution can only be performed on supercomputers such as the Cray. The numerical code has been developed to take advantage of vector processing architecture and thus is reasonably fast on the Cray.<sup>9,10</sup> In the present Phase I study, however, the primary objectives were to demonstrate that an inclined impinging jet and an impinging jet in crossflow can be modeled by the code. Since coarse grid computations are sufficient to demonstrate this capability, simulations on a supercomputer were not carried out in the Phase I study.

Numerical calculations were performed on the in-house MassComp computer. Due to the memory and speed limitations of this scalar processing computer, only coarse grid computations were performed. Nevertheless, it was desirable that the results of these simulations be useful in understanding the flow field associated with inclined impinging jets and impinging jets in crossflow. Also, wherever possible, the potential for comparison with available experimental data was desirable in order to validate the calculations and to demonstrate the strength of the LES technique. Thus, after some experimentation, a grid of 24 x 64 x 24 was chosen as an optimum compromise, considering the computer speed and resource limitations. The computational domain was modeled to extend from  $-1.5 < x/D < 1.5$ , and  $-3 < y/D < 3$ , and a jet-to-ground distance ( $H/D$ ) of 1.5 was simulated. Since the configurations studied in Phase I involved oblique impingement in the  $y$ - $z$  plane and the crossflow was also prescribed in the  $y$ - $z$  plane, the computational domain in the  $x$ - $z$  plane (i.e., the plane of the fountain) could be reduced by assuming symmetry conditions. Thus, at  $x = 0$ , the symmetry boundary conditions are used and the computational domain in the  $x$ - $z$  plane is reduced to  $0 < x/D < 1.5$ .

In our earlier studies,<sup>9,10</sup> it was determined that the evolution of large-scale structures can be effected by the jet-to-ground distance. For example, when the jet exit plane is close to the ground, the ground plane can act as a damping mechanism on the instability waves in the impinging jet shear layer. The computational domain in the horizontal directions ( $x$ ,  $y$ ) is also important. For example, in the  $x$ -direction, the domain determines the spacing between adjacent impinging jets, which in turn affects the dynamics of the fountain. The effect of varying these parameters can be considered in the next phase using a higher grid resolution.

For the grid resolution used in this Phase I study, a Reynolds number of 300 was assumed based on the jet diameter  $D$  and the unperturbed jet exit velocity  $W$ , both of which were chosen to be unity.

## 4.2 Initialization

Here, we describe the initialization procedure used in the present computations. The initialization for the steady-state computations and the coherently forced computations are described separately.

### 4.2.1 Steady-State Profile

The computations were begun with no flow in the domain. At  $t = 0$ , a jet with a profile of

$$w_0(r) = -W \left[ 1 - \left( \frac{r}{r_j} \right)^6 \right] \quad (10)$$

was introduced at the jet exit. Here,  $W$  is the unperturbed axial jet velocity magnitude, which is specified as 1;  $r_j = D/2$  is the radius of the jet; and  $r$  is the radial coordinate with respect to the jet center. Past studies of free jets indicate that the initial jet velocity profile has a "top-hat" shape.<sup>41</sup> However, to resolve the jet shear layer for the "top-hat" profile requires a very high grid resolution, which was not possible, as mentioned earlier. The profile chosen for the present calculations was an optimum compromise for the grid resolution used.

#### 4.2.2 Coherent Forcing

To study the effect of external excitation on the dynamics of the impinging jets, a perturbation  $w'$  is added to the steady-state profile given in Equation (10). The perturbation is of the form

$$w' = -A w_o(r) \sin(\psi) \quad (11)$$

where  $\psi = 2\pi t/T$ ,  $T$  is the time period of the forcing frequency, and  $A$  is the amplitude of forcing. Typically, the amplitude was varied from 10 to 20 percent of the mean velocity. This is similar to experimental studies of forced impinging jets<sup>3</sup> and to our earlier study of normal impinging jets. A forcing frequency was chosen to correspond to a Strouhal number ( $St = fD/U$ ) of 0.47. Here,  $U = W = 1$  is the reference velocity of the unperturbed jet. The Strouhal number chosen for these simulations is in the jet preferred range.<sup>37</sup> Furthermore, the effect of forcing at this frequency was studied earlier for the case of normal impinging jets.<sup>9,10</sup> In this Phase I study, symmetry conditions were imposed at  $x = 0$  in order to adequately resolve the large-scale structures with the available grid resolution. This implies that only axisymmetric forcing of the jet could be studied. To study the effect of azimuthal or random excitation of the impinging jet,<sup>10</sup> the full jet has to be modeled. This requires a much higher grid resolution and therefore will have to await a future study.

## 5. RESULTS OF SIMULATIONS

In this section, we describe in detail the results of the numerical study carried out in this investigation. This section is divided into four parts dealing with the four flow configurations of interest: the oblique impinging jet, the normal impinging jet without crossflow, the normal impinging jet in crossflow, and the normal impinging jet in crossflow with a moving ground plane.

### 5.1 The Oblique Impinging Jet

The computations of the oblique impinging jet were begun with no flow in the computational domain and at  $t = 0$ . The steady-state jet velocity as prescribed by Equation (10) was imposed at the jet exit.

A starting vortex is shed by the jet during its initial propagation. This vortex impinges on the ground plane and propagates along the ground. For example, Figure 3 shows a three-dimensional perspective of the total vorticity  $|\omega|$  in the jet impinging at an angle of  $60^\circ$  (see Figure 2). Vorticity higher than the level shown will be contained inside the surface shown. Note that in all the three-dimensional perspective views shown in this report, the full computational domain is shown to improve the clarity of presentation. The vorticity in the full jet is generated by forming a symmetric image in the  $-1.5 < x/D < 0$  domain from the computed solution in the  $0 < x/D < 1.5$  domain by using the symmetry conditions at  $x = 0$ . Figure 3 shows the time when the starting vortex ring has impinged on the ground and is propagating along the ground. In our earlier study of normal impinging jets,<sup>9</sup> it was determined that the phase speed of this ring on the ground is initially the same in all radial directions, but as the vortex ring approaches the fountain axes, the rings from the two adjacent wall jets collide and rise into the fountain. This forms the upwash that eventually impinges on the top wall, resulting in the so-called "lift-off" effect. The motion of the vortex in the fountain reduces the phase speed of the vortex ring on the ground plane and, subsequently, the vortex ring starts to twist and eventually breaks up into isolated structures. When the computation was continued with the steady-state profile as given by Equation (10), the flow field eventually reached a steady state.

For the inclined jet, the vortex ring does not propagate uniformly in all directions on the ground plane. Depending upon the angle of impingement, only a relatively small portion of the fluid will be transported in the backward direction. For example, Taylor<sup>15</sup> showed from conservation of momentum parallel to the plate that, for a two-dimensional jet impinging at an angle  $\theta$ , the fraction of the fluid that flows forward is  $\cos^2\theta/2$  and the fraction that flows backward is  $\sin^2\theta/2$ . This implies that for an angle of  $60^\circ$ , only 25 percent of the fluid is transported in the backward direction. In the three-dimensional case, this is not true; the mass flux in the forward and the backward direction can be determined only by integrating the total flux in the azimuthal direction. Rubel<sup>17</sup> derived an expression for the fraction of fluid carried forward in the three-dimensional case and showed that this fraction is  $(1 - \frac{\theta}{\pi} + \frac{\sin 2\theta}{2\pi})$ , which for the present case of  $\theta = 60^\circ$ , gives a value of around 0.805. This value agrees quite well with the experiments of Schach<sup>13</sup> and Taylor.<sup>14</sup>

The dynamics of the vortical structures being transported in the forward and the backward directions can be visualized in Figure 4, which shows a time sequence of the the  $x$ -vorticity contours in the  $y$ - $z$  plane at  $x = 0$ . Figure 4a shows the instant when the jet first impinges on the ground. Further in time, the wall jet is formed in both the forward and backward directions. However, the vorticity on the ring behind the jet is much lower than that ahead of the impingement point. The size of the vortex behind the inclined impinging jet is also smaller than that ahead of the jet and the vortex structure

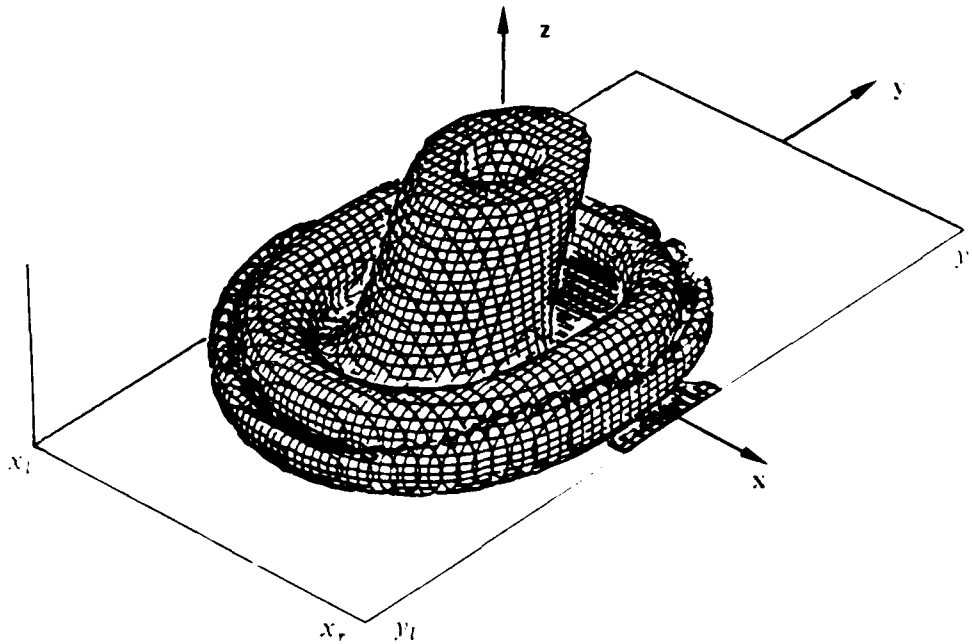


Figure 3. Three-dimensional perspective of the total vorticity,  $|\omega|$  in the inclined impinging jet for the unforced case.

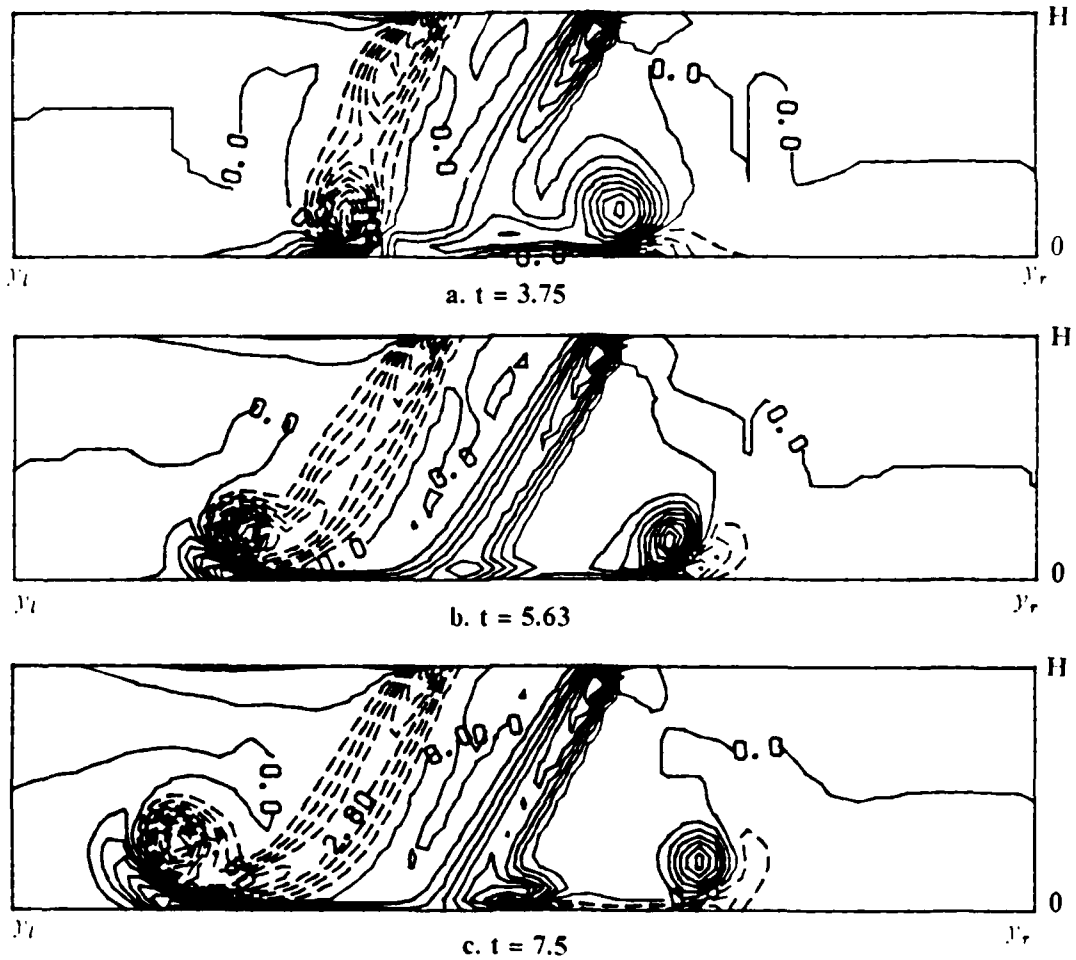


Figure 4. Time sequence of the propagation of the starting vortex in the inclined impinging jet. The  $x$ -vorticity contours in the  $y$ - $z$  plane at  $x = 0$ . Contour interval is 0.7.

appears to be isolated. These figures also clearly show that most of the fluid in the impinging jet is carried in the forward direction. A region of secondary vorticity (of opposite sign) appears ahead of the propagating vortex ring. This is consistent with experimental observation<sup>3</sup> and was also seen in earlier calculations.<sup>9</sup> The details of the secondary vorticity could not be determined due to the lack of adequate grid resolution in the wall region.

Figure 5 shows the corresponding time sequence of the  $y$ -vorticity contours in the  $x$ - $z$  plane at  $y = 0$ . This is a view in the plane of the fountain. The shed vortex ring propagates toward the fountain axis (i.e.,  $x = x_f$ ) as time progresses. If the computations were continued, this vortex ring in the wall jet will collide with the vortex ring in the opposing wall jet and create an upwash in the fountain. This upwash would then spread upward as the vortex rings climb up the fountain and eventually impinge on the top wall. This results in the lift-off effect of the fountain that is of great importance for  $V/STOL$  aircraft operating near the ground.

Due to the time and resource constraints of the Phase I study, however, the simulation was not continued until a steady state was reached. Instead, the solution at the time shown in Figure 3 was perturbed by adding a fluctuation  $w'$ , of the form given in Equation (11), to the steady-state jet profile. A forcing amplitude of  $0.2U$  was employed for these simulations. Simulation was then continued for six cycles of forcing and the results were acquired in detail and analyzed for the last forcing cycle.

Figure 6a shows the three-dimensional perspective of the total vorticity  $|\omega|$  at the end of the last forcing cycle, using the same viewing angle and vorticity level as in Figure 3. Figures 6b and 6c show the  $x$ - and  $y$ -vorticity components (i.e.,  $|\omega_x|$  and  $|\omega_y|$ ), respectively, in a similar three-dimensional perspective. The bulge in the impinging jet is the result of the passage of the shed vortex ring. With a higher grid resolution, the shed vortex ring would be clearly visible, as was shown in earlier calculations.<sup>10</sup> Due to the forcing, the vortex ring is shed at the forcing frequency. The impingement of this vortex ring on the ground is quite similar to that observed for the starting vortex (Figure 3). When the vortex ring propagates on the ground, most of the vorticity is carried in the forward-moving portion of the ring while the vorticity in the ring behind the jet is much weaker. When the vortex rings reach the fountain axes, they collide with the vortex ring from the adjacent wall jet (due to the periodic boundary conditions at  $x/D = 1.5$ ). After the collision, the vortex rings continue to propagate up into the fountain. The lift-off of the vortex ring into the fountain can be seen in Figure 6a. Due to the combined effect of the lift-off into the fountain (in the  $x$ - $z$  plane) and the forward propagation to the outflow (in the  $y$ - $z$  plane), the vortex rings start to twist and eventually break down into smaller structures.

The vorticity shed by the impinging jet is redistributed due to the motion in the three-dimensional space, as can be observed in Figures 6b and 6c. For example, the vorticity in the outflow direction is predominantly  $|\omega_x|$  (Figure 6b), whereas in the plane of the fountain,  $|\omega_y|$  dominates. The region of secondary vorticity on the ground below the primary vortex ring can also be seen. The details of the small-scale structures in the flow field are not very clear in these figures, primarily due to the low grid resolution of the calculations. High-resolution computations of normal impinging jets show more details of the breakdown of the large structures.<sup>9,10</sup>

Figure 7 shows a time sequence of the  $x$ -vorticity contours in the  $y$ - $z$  plane at  $x = 0$  for the entire last forcing cycle. The figures are shown  $\pi/2$  apart in the forcing cycle. In comparing the first and the last figure, it is evident that the sequence of vortex shedding in the jet repeats itself. This is characteristic of external forcing, which suppresses the natural instability of the jet, and the shed

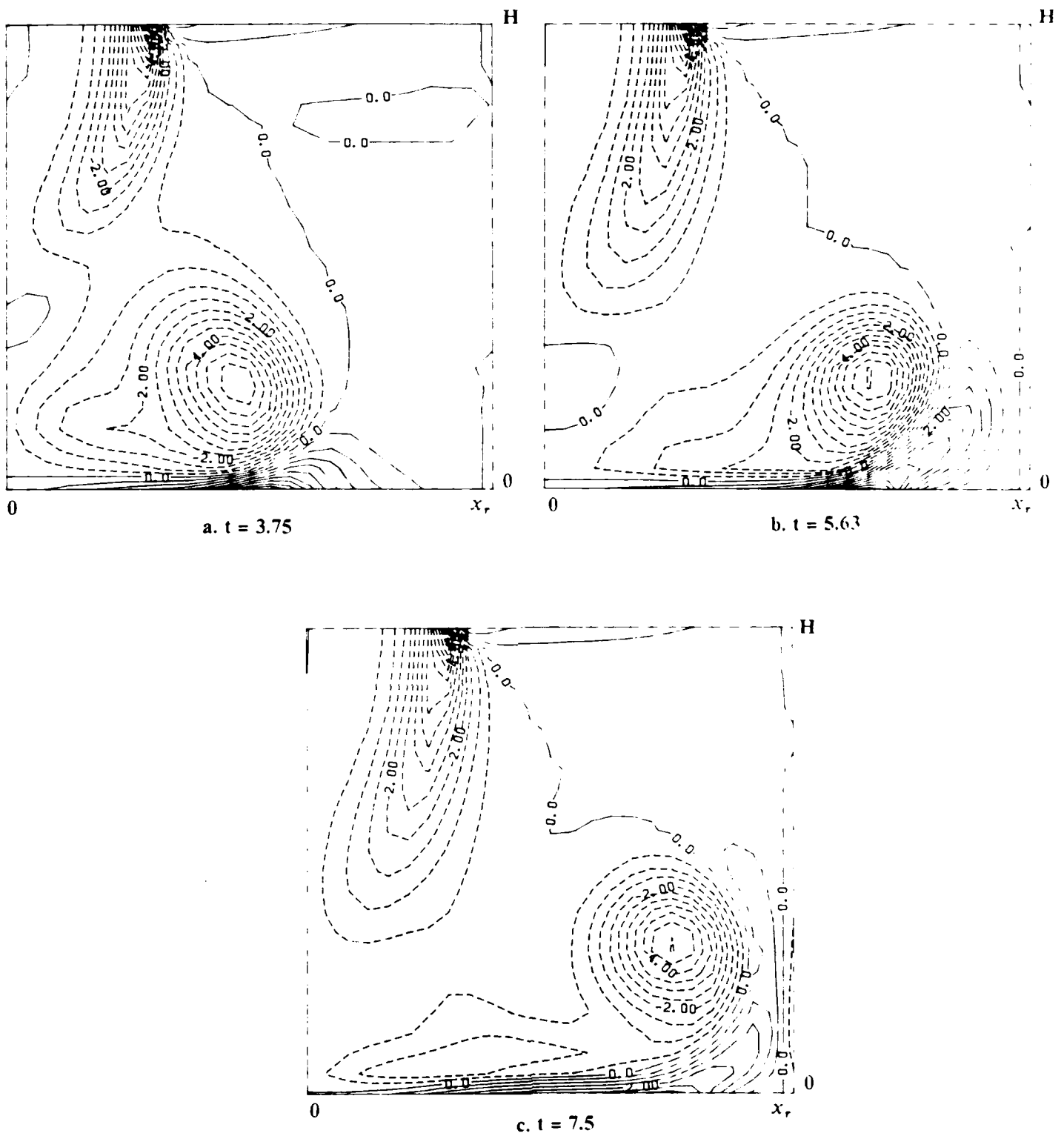
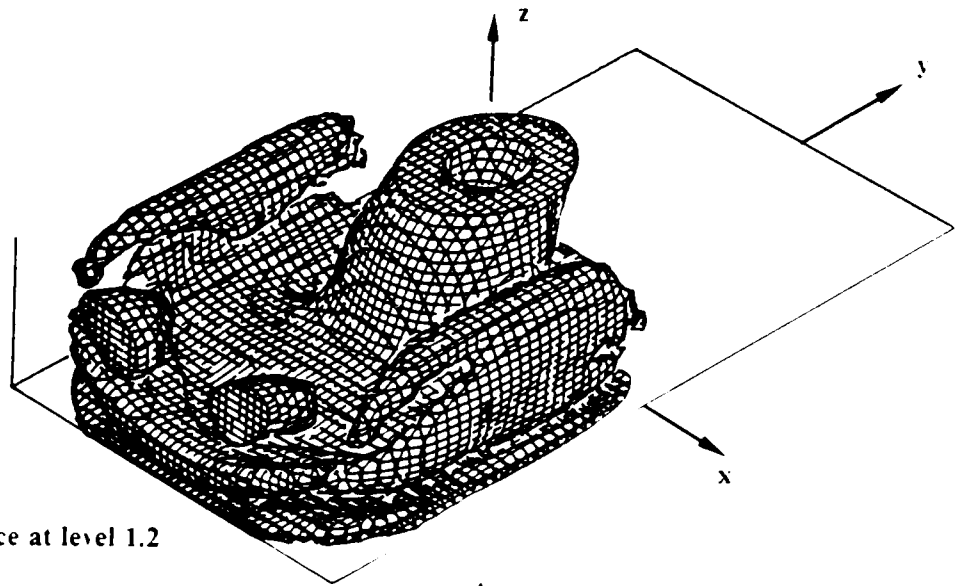
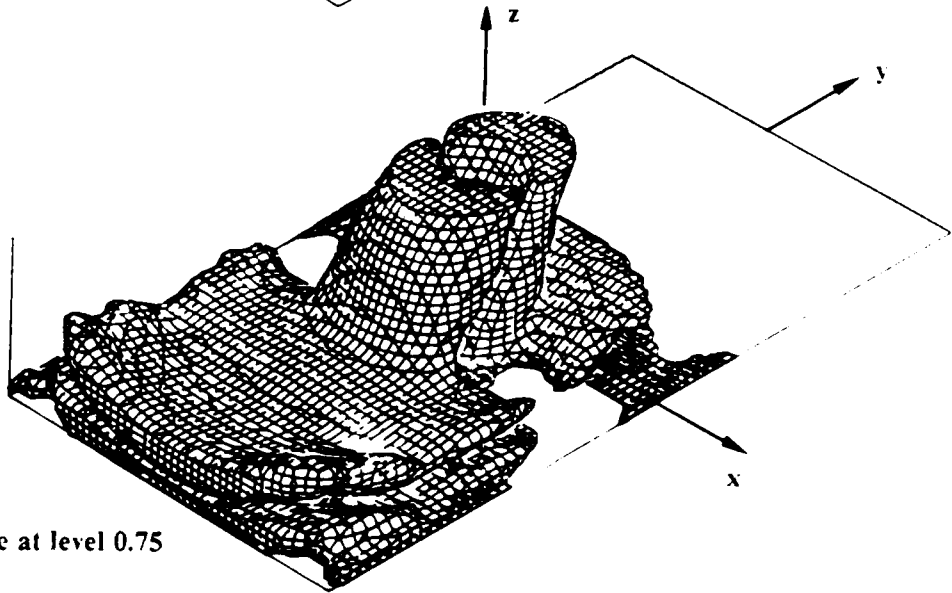


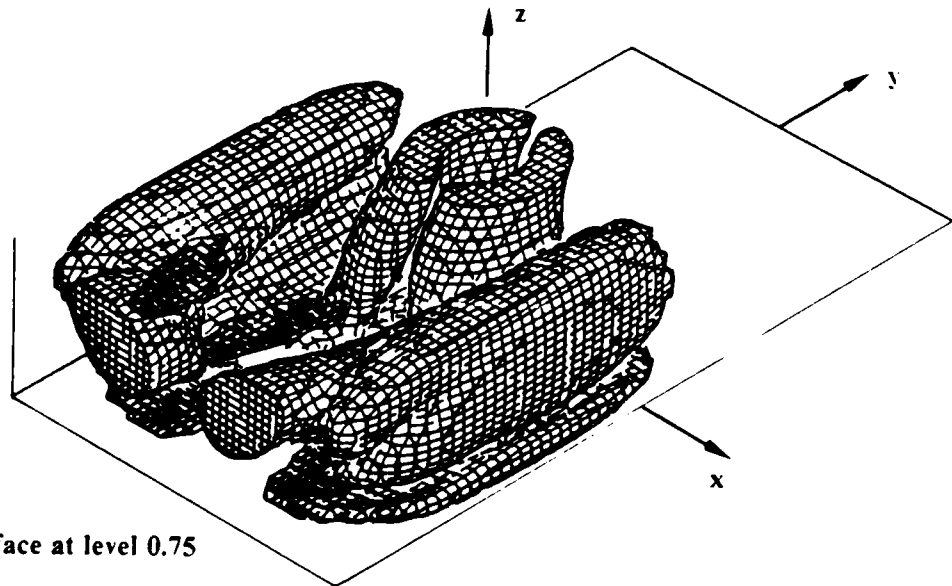
Figure 5. Time sequence of the propagation of the starting vortex in the inclined impinging jet. The  $y$ -vorticity contours in the  $x-z$  plane at  $y=0$ . Contour interval is 0.5.



a.  $3D|\omega|$  surface at level 1.2



b.  $3D|\omega_z|$  surface at level 0.75



c.  $3D|\omega_y|$  surface at level 0.75

Figure 6. Three-dimensional perspective of the total vorticity  $\vec{\omega}$  in the inclined impinging jet at the end of six forcing cycles.

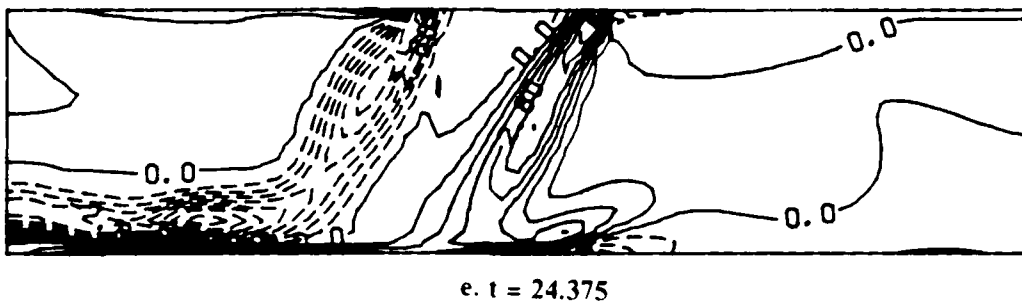
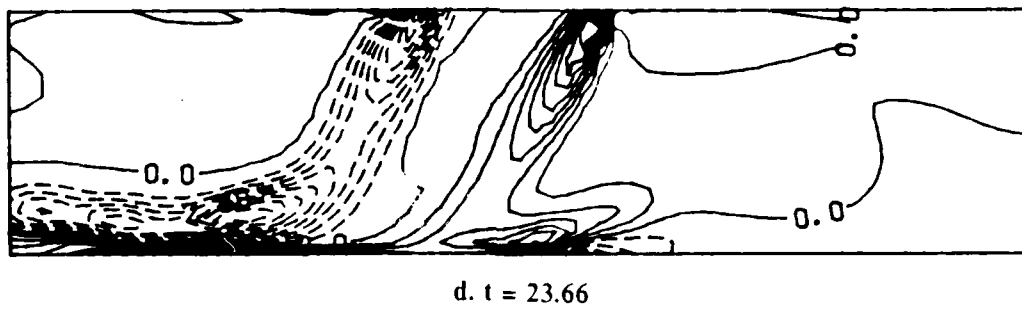
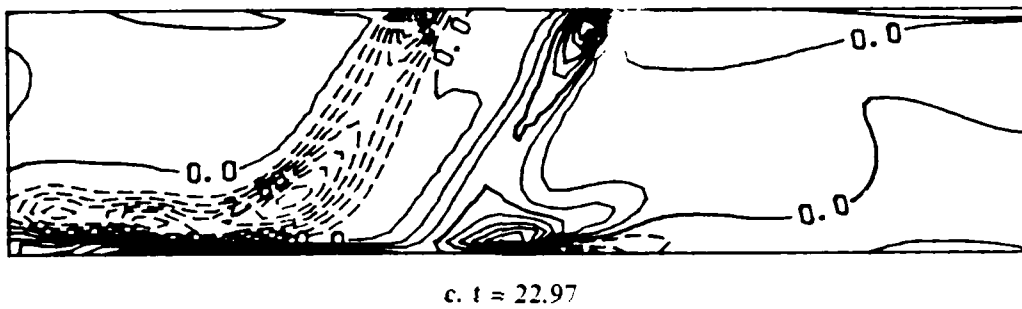
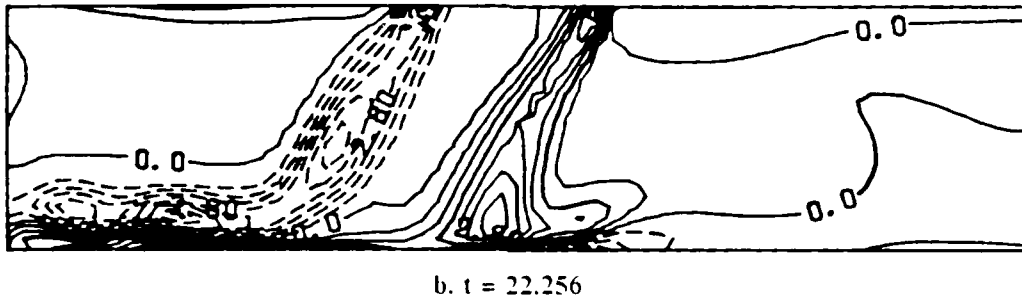
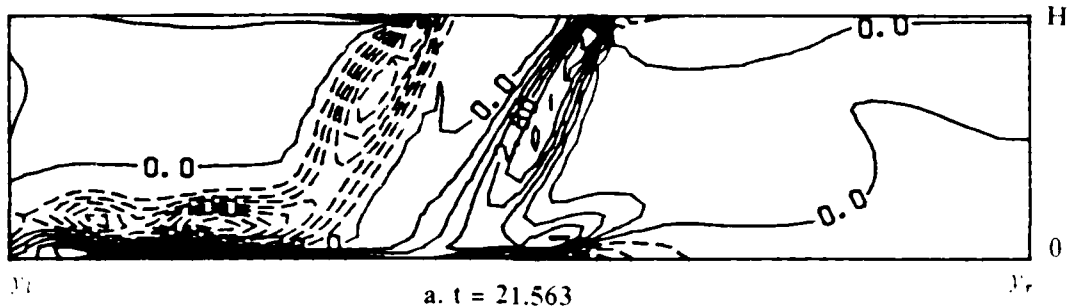


Figure 7. Time sequence of the  $x$ -vorticity contours in the  $y$ - $z$  plane at  $x = 0$  for the last forcing cycle. Contour interval is 0.7.

structures are organized by the forcing frequency. The phase speed of the vortex ring in the jet shear layer can be estimated from this time sequence to be around  $0.6U$ , which agrees with the experimental value obtained for normal impinging jets.<sup>3</sup> This implies that the obliqueness of the impinging jet does not significantly affect the convective speed of the structures in the jet. A region of secondary vorticity ahead of the propagating vortex ring is again observed. It appears that some of this secondary vorticity is due to the forward transport of vorticity from the rear of the jet. This also results in a reduction of the vorticity levels behind the jet (i.e.,  $y/D > 1$ ). The details of the secondary vorticity are not seen clearly in this simulation due to the coarseness of the mesh. In the earlier study,<sup>9</sup> it was demonstrated that the secondary vorticity appears as a result of the unsteady separation of the wall boundary layer caused by an adverse pressure gradient. This behavior has also been determined in experimental studies.<sup>3</sup> The physics of this phenomena should not be affected by the inclination of the jet and thus a similar process of unsteady separation is expected to occur for the inclined jet case. To confirm this, however, high-resolution simulations must be performed. This will be considered in the next phase.

The separation between the structures in the wall jet give a wavelength  $\lambda$  of around  $0.56D$ , which for a forcing frequency  $f$  of  $0.47$ , results in a convective speed of  $U_c = \lambda f = 0.26U$ . This is again similar to that observed in the axisymmetric forcing study of normal impinging jets.<sup>9</sup> This speed is lower than that for an isolated impinging jet<sup>3</sup> and is primarily due to the presence of the fountain, which retards the forward motion of the structures in the outflow direction.

Figure 8 shows the corresponding  $y$ -vorticity contours in the  $x$ - $z$  plane at  $y = 0$ . Due to the symmetry conditions at  $x = 0$ , only half of the full domain in the  $x$ - $z$  plane is shown. This view shows the motion in the fountain region. Notice that the vortex ring propagates on the ground and is then lifted into the fountain. The vorticity in the ring decreases as it moves up in the fountain, primarily due to the three-dimensional spreading. The fountain spreads upward and impinges on the undersurface of the top plate and consequently spreads on the top wall. This impingement process is the primary mechanism for the lift-off effect of the fountain on a V/STOL aircraft. Due to the close proximity of the jet axis to the fountain axis in this simulation, some portion of the fluid in the fountain is entrained into the impinging jet. This would result in a modification of the spreading rate of the impinging jet.

Figure 9 compares the velocity vector field and the pressure field in the  $y$ - $z$  plane at the end of the last forcing cycle. The inclined impingement of the jet is clearly seen (Figure 9a). In addition, it can be observed that the stagnation point on the ground plane does not occur at the  $y = 0$  location (which is the stagnation point for a normal impinging jet), but is offset ahead by a certain distance. This new location of the stagnation point depends upon the angle of impingement. The jet physical centerline is inclined at  $\theta$  to the ground and is ahead of the stagnation streamline. These general features are in good agreement with past experimental observations.<sup>14</sup> Figure 9b shows the velocity vector field in the plane of the fountain ( $x/D = 1.5$ ). Unlike the symmetric fan-like behavior of the upflow in the fountain for the normal impingement case, the upwash is skewed in the direction of inclination of the impinging jet. This implies that the flow impingement on the top wall will also be skewed and thus will probably result in a nonuniform lift force on the aircraft. Comparing the velocity (Figure 9a) and pressure gradient (Figure 9c) vector fields with the corresponding vorticity contours shown earlier (Figure 7e) indicates that there is an adverse pressure gradient ahead of the primary vortex ring. Here, the direction of the vector indicates the direction of increasing pressure. There is also a low-pressure region associated with the core of the shed vortex ring. These low-pressure regions are seen

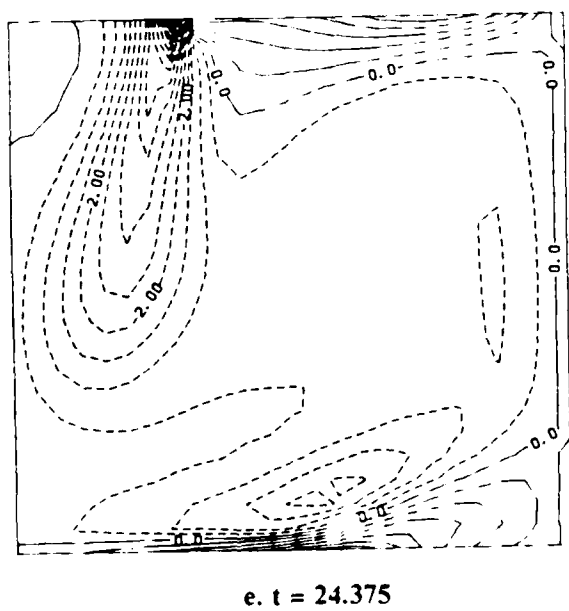
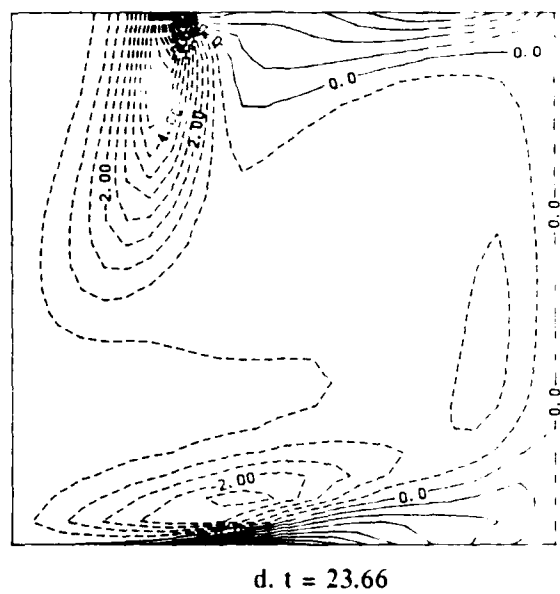
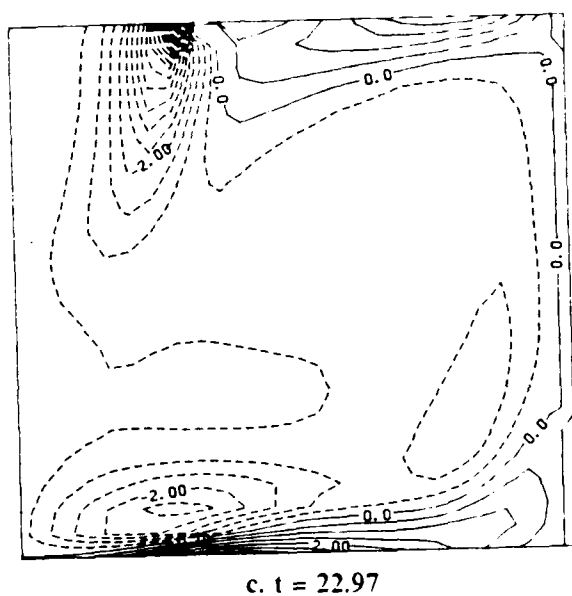
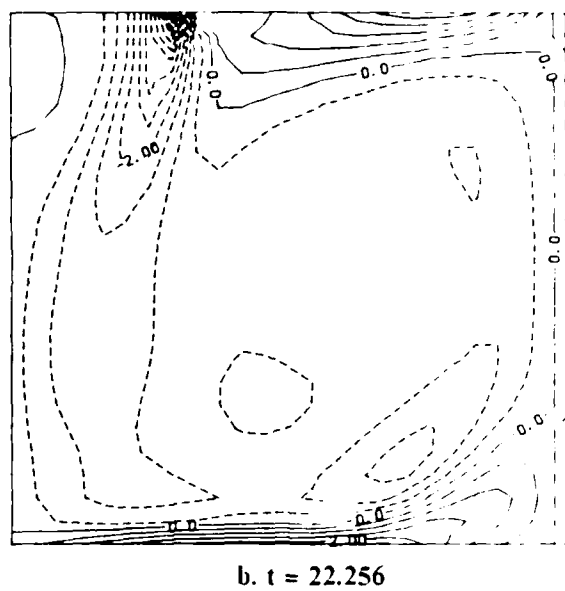
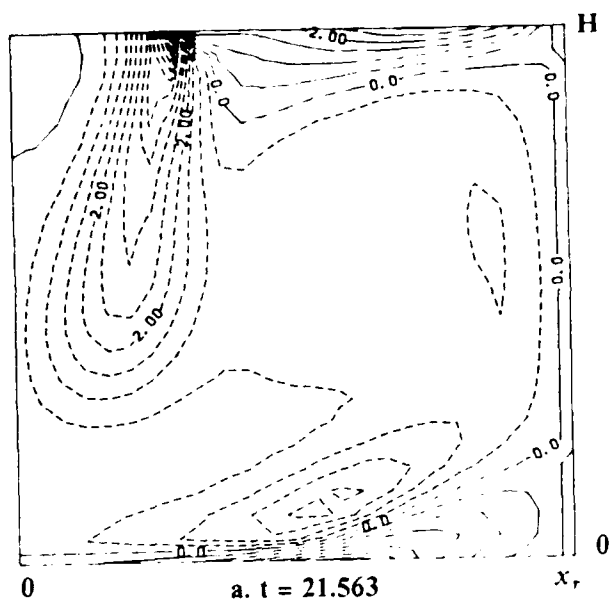


Figure 8. Time sequence of the  $y$ -vorticity contours in the  $x-z$  plane at  $y = 0$  for the last forcing cycle. Contour interval is 0.5.

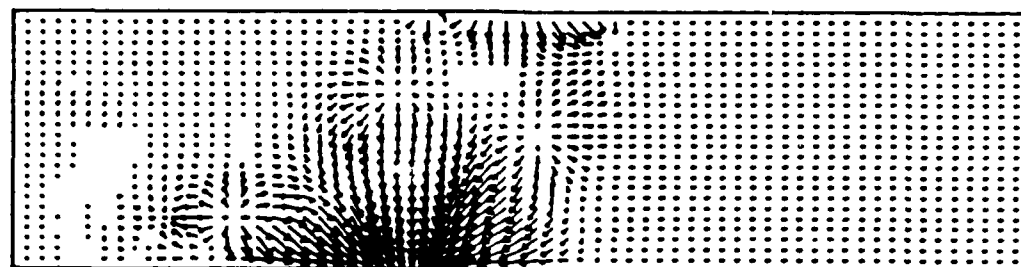
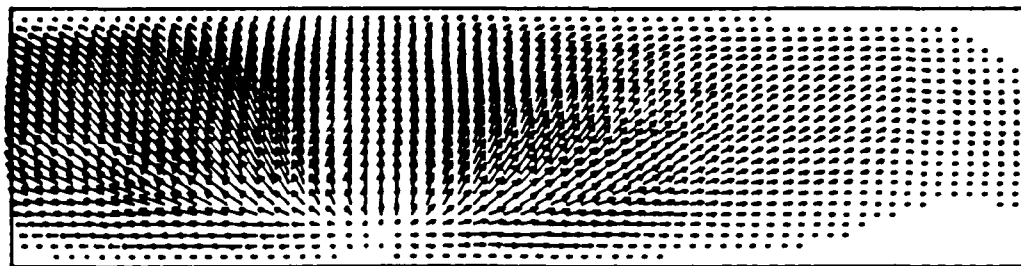
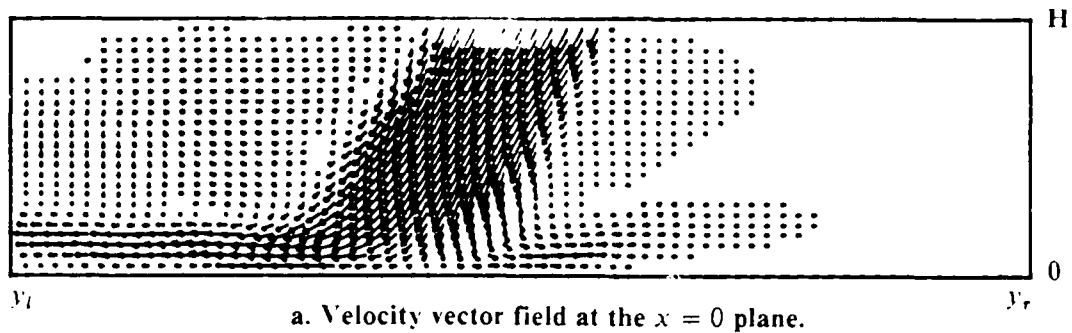


Figure 9. Comparison of the velocity vector fields, pressure gradient and pressure contours in the  $y-z$  plane at  $t = 24.375$

more clearly in the pressure contours in the  $y$ - $z$  plane shown in Figure 9d. The pressure contours on the ground also show that the stagnation pressure is offset from the  $y = 0$  location. This distance can be determined from this figure to be around  $0.57D$ . The pressure contours also show a compression occurring behind the peak location. This behavior was also observed in earlier experiments<sup>5</sup> and in computations.<sup>16</sup>

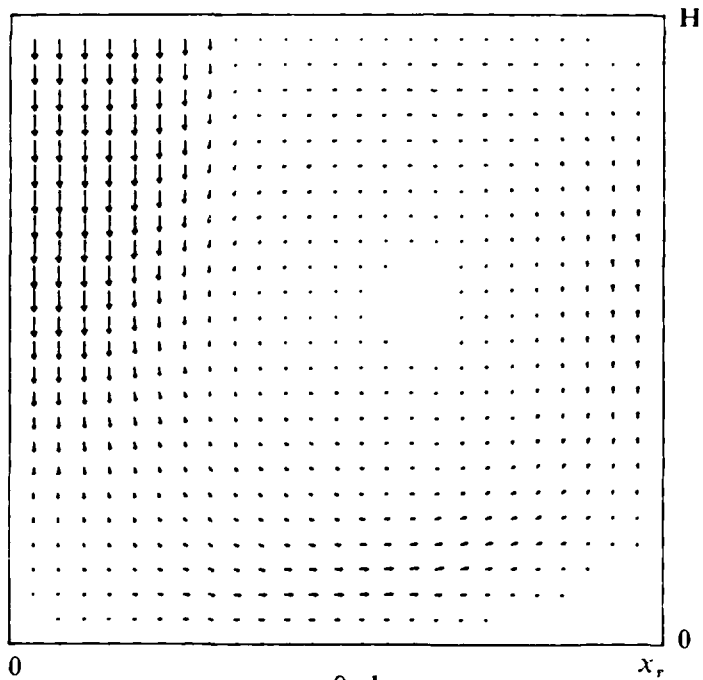
The stagnation streamline can be approximately located by using the stagnation point location on the ground in Figure 9a or 9d and drawing a line at  $60^\circ$  to the ground. Its corresponding location in the vorticity plot (Figure 7e) can then be determined. It can then be shown that there is nonzero vorticity on the stagnation streamline, thereby confirming the previous predictions<sup>18</sup> that oblique impingement results in a stagnation streamline with nonzero vorticity.

Figures 10a and 10b show the velocity vector field in the  $x$ - $z$  plane at  $y = 0$  and  $y/D = 1.5$ , respectively. The comparison of the magnitude of the velocity vectors in the impinging jet (Figure 10a) and in the fountain (Figure 10b) indicates that the fountain is relatively weaker. This is due to obliqueness, which results in a significant velocity component in the positive  $y$ -direction and thus changes the direction of fluid motion in the fountain region. Some of the fluid impinging on the top wall spreads and is entrained into the impinging jet. This spreading and the entrainment process are stronger away from the jet centerline, as seen in Figure 10b. Recirculation of the fluid occurs at this location and is quite strong due to the short jet-to-ground height. If the height  $H$  is increased, this recirculation would be weakened and the effects of entrainment of the fluid into the impinging jet would also be reduced.

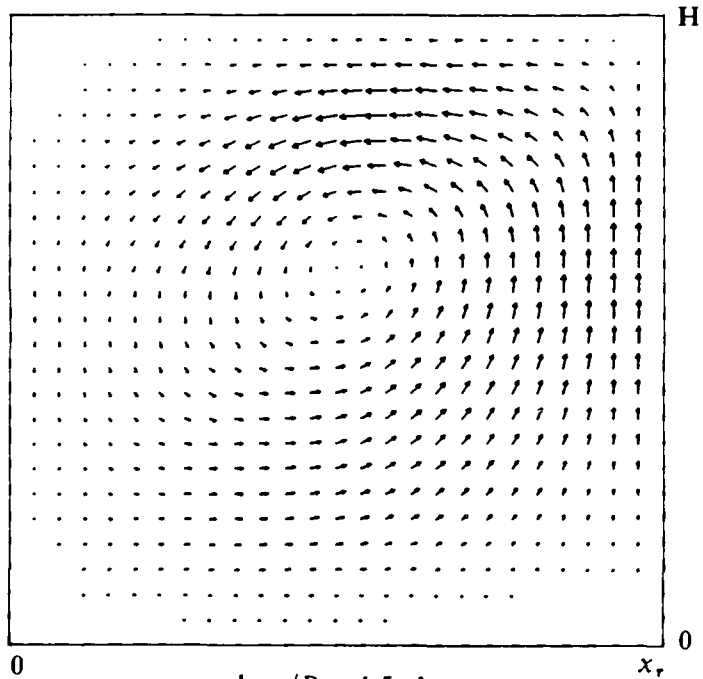
Figure 11 shows the pressure contours on the top plate and the ground plane. The offset between the center of the jet at its exit plane on the top wall (which is a low-pressure region) and the stagnation point on the ground is clearly observable. As seen earlier, the pressure field on the ground is skewed in the direction of the forward motion with some compression occurring behind the peak location. It is possible to estimate the net lift-off on the top plate by integrating the pressure on the plate. From this figure, the offset of the stagnation point for the inclined jet from its location for a normal impingement (at  $y = 0$ ) can be estimated. A value of around  $0.57D$  is again estimated. This computed offset compares quite well with the experimental data of Donaldson and Snedeker<sup>5</sup> who obtained a value of around  $0.588D$  for  $H/D = 1.96$ .

Figure 12 shows typical velocity profiles in the flow field. Figure 12a shows the  $v$ -velocity profiles in the  $y$ - $z$  plane at  $x = 0$ . The profiles one half-cycle apart in the last forcing cycle are shown in this figure. It is clear that in the forward direction (i.e., the negative  $y$ -direction) the wall boundary layer grows toward the outflow. However, in the backward direction (positive  $y$ -direction), the wall jet is quite weak, and very little outflow is occurring near the outflow boundary. This also indicates that most of the fluid is being transported in the forward direction. The effect of forcing is observable only near the wall region.

Figure 12b shows the corresponding  $u$ -velocity profile in the  $x$ - $z$  plane at  $y = 0$ . Due to the close proximity of the fountain axis, the effect of forcing is quite noticeable in these velocity profiles. The growth of the wall jet is again observable. On the top wall, there is a reverse wall jet which is caused by the impingement of the fountain on the top wall. The reverse wall jet also causes the fluid in it to be entrained into the impinging jet and thus modifies the spreading rate of the impinging jet.



a.  $y = 0$  plane.



b.  $y/D = 1.5$  plane.

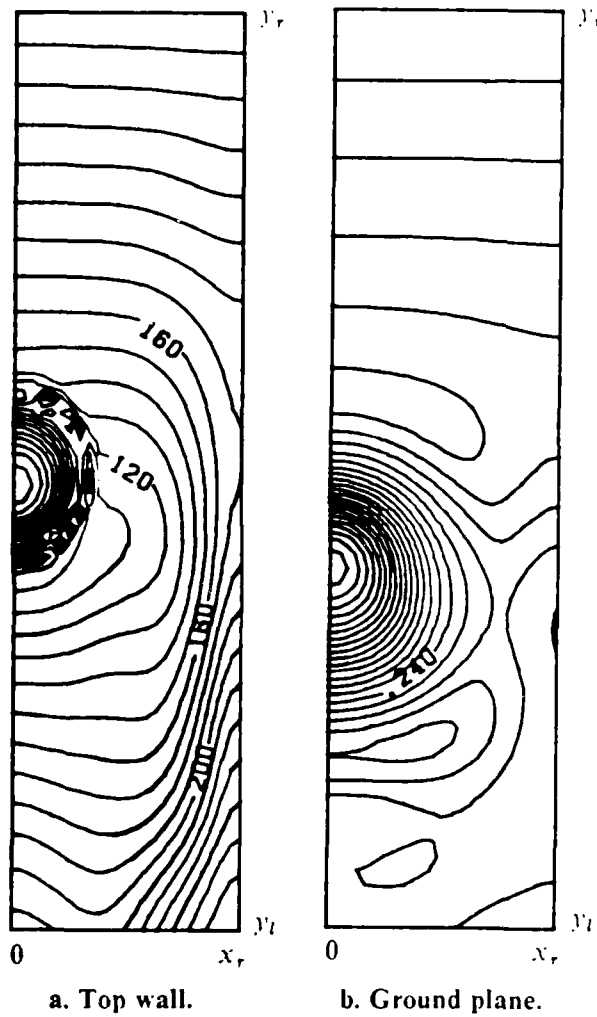
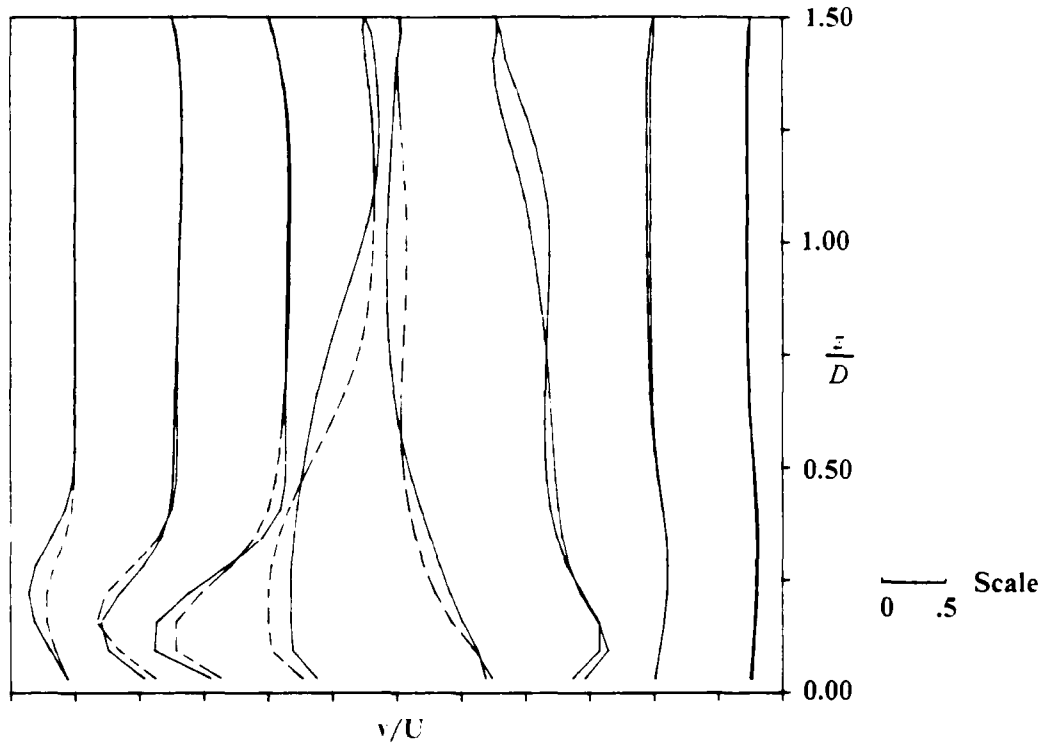


Figure 11. Pressure contours in the  $x-y$  plane at  $t=24.375$ .

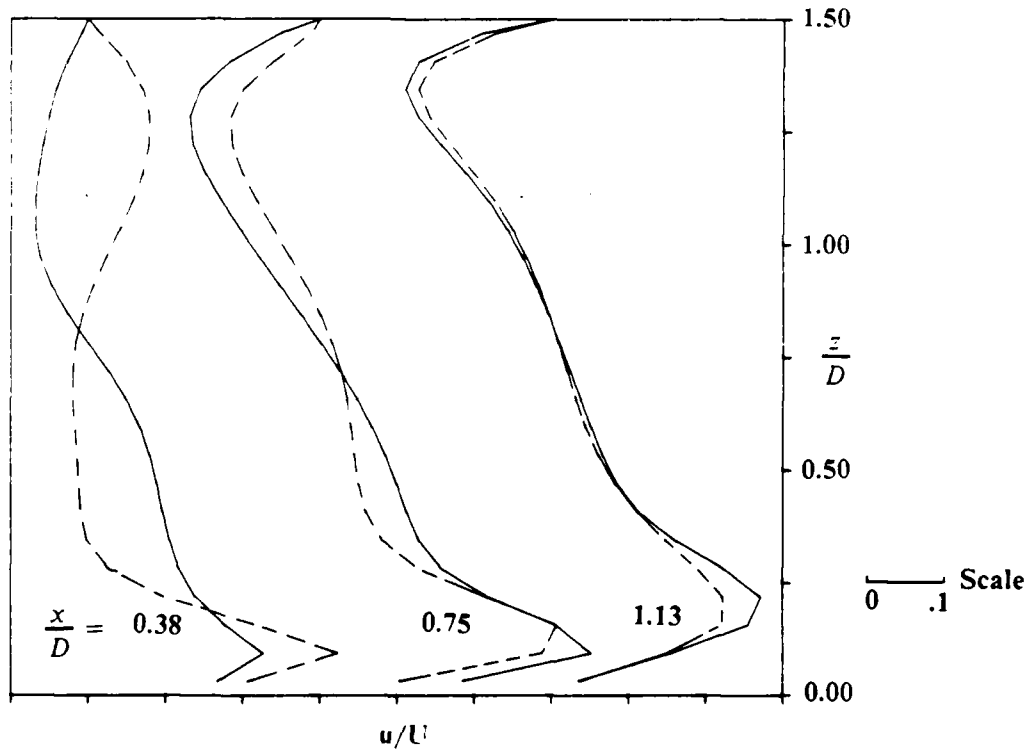
Figure 10. The velocity vector fields in the  $y-z$  plane at  $t=24.375$ .

$\frac{v}{D} = -2.33 \quad -1.67 \quad -1.00 \quad -0.33 \quad 0.33 \quad 1.00 \quad 1.67 \quad 2.33$



a.  $v$ -velocity profiles in the  $y-z$  plane at  $x = 0$ .

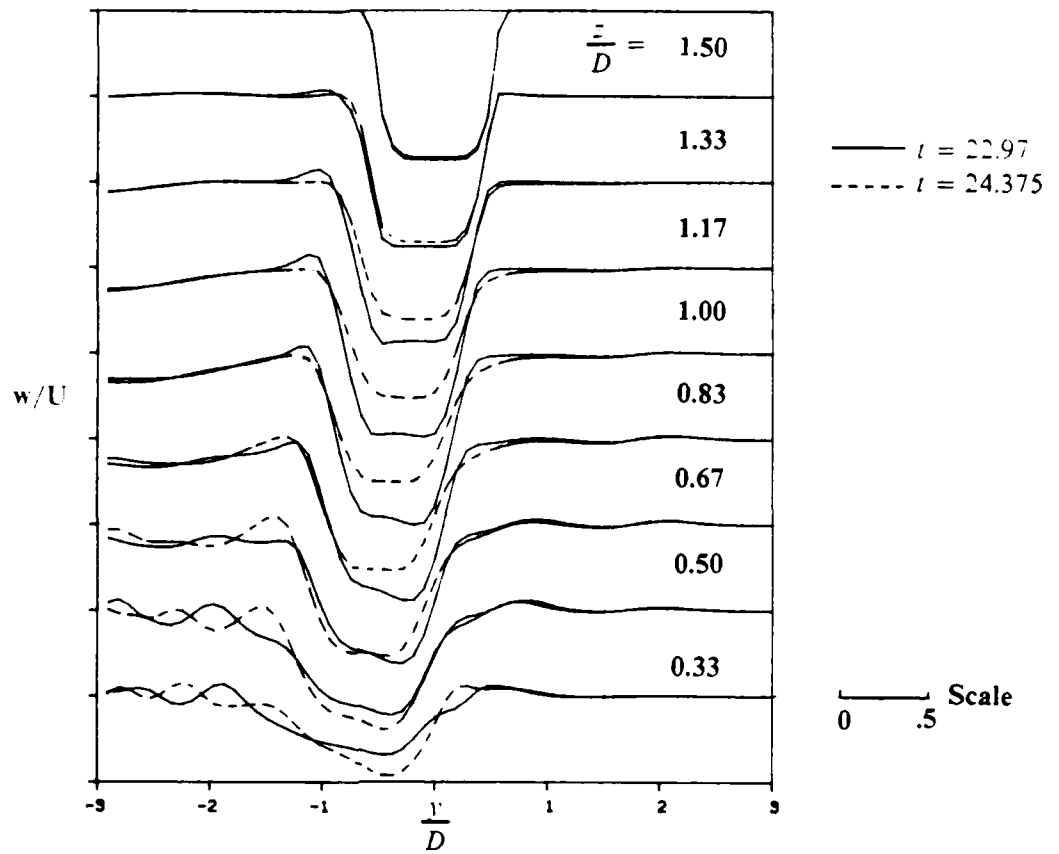
---  $t = 22.97$     —  $t = 24.375$



b.  $u$ -velocity profiles in the  $x-z$  plane at  $y = 0$ .

---  $t = 22.97$     —  $t = 24.375$

Figure 12. The velocity profiles in the flow field.



c.  $w$ -velocity profiles in the  $y-z$  plane at  $x = 0$ .

Figure 12. The velocity profiles in the flow field (cont.).

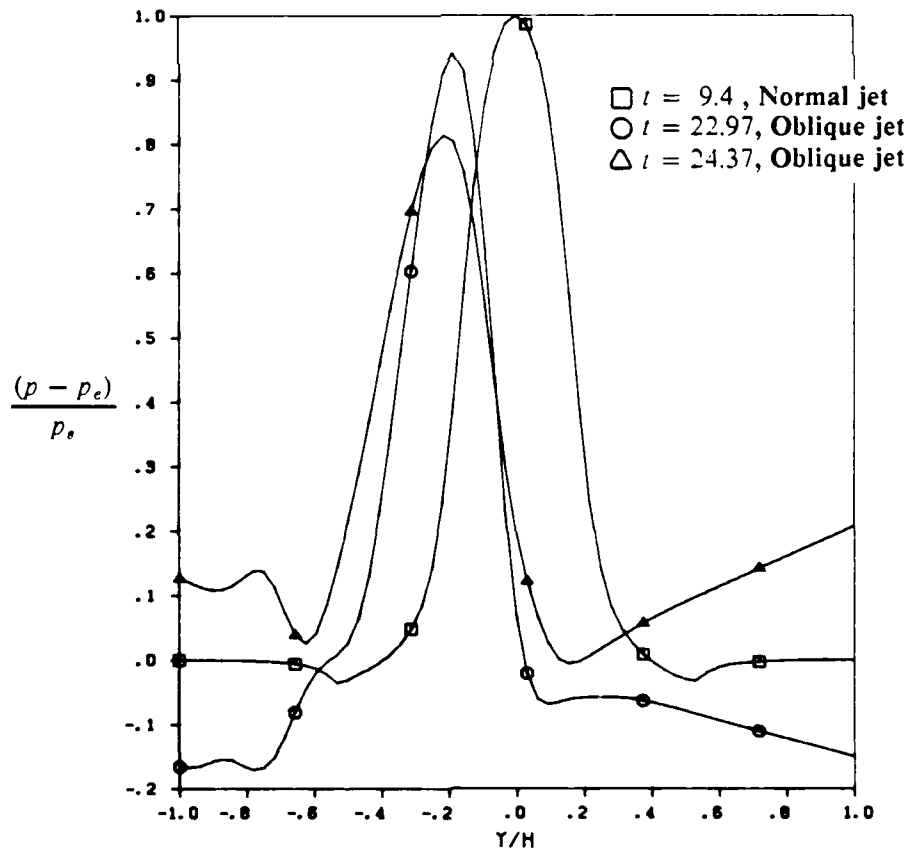


Figure 13. The pressure variation on the ground plane.

Figure 12c shows the  $w$ -velocity component in the  $y$ - $z$  plane at  $x = 0$ . This figure shows the vertical velocity profiles in the impinging jet. The spreading of the impinging jet and the oblique impingement of the jet can be visualized from this figure. The effect of forcing on the profiles near the ground is also seen. Notice that there is some positive  $w$ -velocity close to the wall. This implies an upflow and is indicative of lift-off from the ground associated with the separation and the formation of secondary vorticity ahead of the propagating vortex rings in the wall jet. A similar behavior was observed in the earlier normal impingement study.<sup>9</sup>

In principle, other data such as the jet centerline velocity decay could be reduced from the computed results. However, since the computational grid is Cartesian and the jet centerline is inclined, a complex three-dimensional interpolation of the centerline velocity field from the computed velocities on the computational nodes is required to estimate the centerline velocity. Due to the limited resources of the Phase I study, the development of the interpolation package has been deferred to the next phase.

Finally, Figure 13 shows the variation of the pressure on the ground plane in the  $y$ - $z$  plane at  $x = 0$ . The pressure at the outflow boundary at  $y/D = 3.0$  for the normal impingement case was assumed to represent the *ambient* pressure ( $p_\infty$ ). The pressure is normalized by the pressure for the normal impingement case (to be discussed in Section 5.2.1) by the relation

$$P = \frac{p - p_\infty}{(p_o)_{90} - p_\infty} \quad (12)$$

where  $(p_o)_{90}$  is the stagnation pressure for the normal impingement case. This normalization was carried out to be consistent with the experimental normalization.<sup>5</sup> The pressure variation for the normal impingement is shown in this figure along with the pressure variation for the inclined jet at two instances in the forcing cycle. Only qualitative comparison between the normal and the oblique impingement is intended here since the simulation with normal impingement (described in the next section) was not carried out to steady state. Thus, the higher value of the peak pressure for the normal impingement case is probably due to the transient effects in that simulation. The shift of the stagnation pressure due to oblique impingement can be observed in this figure. The effect of forcing causes the peak pressure to vary with the forcing cycle. However, the location is not changed significantly. Note also that, whereas the pressure distribution is symmetric for the normal impingement case, oblique impingement results in significant asymmetry. There is an unsteady variation of pressure away from the stagnation point, with the forcing causing the favorable pressure gradient (at  $t = 22.97$ ) to become an adverse pressure gradient (at  $t = 24.375$ ).

## 5.2 The Normal Impinging Jet without Crossflow

Since the normal impinging jet was also simulated, a brief discussion of the results for this case is also presented here for completeness. Furthermore, the effect of oblique impingement (Section 5.1) and the effect of crossflow (to be discussed in Sections 5.3 and 5.4) can be understood in greater detail through comparison with the reference case of a normal impinging jet. More detailed analyses of the normal impinging jets have been described earlier.<sup>9,10</sup> In the present study, the simulation was carried out only for a short duration and the steady-state solution was not reached. Thus, only a qualitative interpretation of the computed results is presented here.

The simulation for the normal impingement case was also begun with no flow and with the jet velocity profile given in Equation (10) imposed at the jet exit at  $t = 0$ . Figure 14 shows a three-dimensional perspective of the total vorticity  $|\omega|$  for the normal impingement case at the end of the present simulation. At this time, the starting vortex has just reached the fountain axis and has begun to lift off. The flow field is symmetric in both the  $x$ - $z$  and  $y$ - $z$  planes, as expected, and the secondary vorticity ahead of the primary vortex ring can be seen. Although the perspective viewing angle is different from that shown for the oblique impinging case (Figure 3), comparison between the figures shows the characteristic changes due to oblique impingement.

Figures 15a and 15b show the  $x$ -vorticity in the  $y$ - $z$  plane at  $x = 0$  and the  $y$ -vorticity in the  $x$ - $z$  plane at  $y = 0$ , respectively, at the same point in time shown in Figure 14. The symmetric propagation of the vortex ring in the wall jet (Figure 15a) and the lift-off into the fountain in the  $x$ - $z$  plane (Figure 15b) can be seen. Notice that, due to the proximity of the fountain axes, the vortex ring rises up in the upwash while in the outflow direction it is still propagating on the ground. This eventually results in the breakdown of the ring into smaller structures.

Figure 16 shows representative velocity vector fields in the flow field. Figures 16a and 16b show the velocity fields in the  $y$ - $z$  plane at  $x = 0$  and at  $x/D = 1.5$ , respectively. The vortical motion in the wall jet causes the flow to rotate around the vortex ring and entrain the potential field into the wall jet (Figure 16a). The stagnation point of the impinging jet is located at  $y = 0$ , as expected. Comparing Figures 15a and 16a, it can be seen that the vortex and the velocity field are not at exactly the same location. As shown previously,<sup>9</sup> it is incorrect to infer the vortical motion (which is the result of the velocity gradients) from the velocity field alone. This is an important factor in interpreting the flow field associated with vortical motion.

Figure 16b shows the symmetric fan in the plane of the fountain. The upwash has not yet reached the top wall at this stage of the computations. This figure can be compared with the corresponding case for oblique impingement (Figure 9b) to identify the differences in the upwash due to oblique impingement. Figure 16c shows the velocity vector field in the  $x$ - $z$  plane at  $y = 0$ . The slowing of the wall jet as the fountain axis is reached can be observed. There is another stagnation point at the location where the two wall jets collide that is slightly above the ground, as can also be seen in Figure 16b. The formation of the upwash is also apparent in this figure. Comparison with the corresponding plot for the inclined jet (Figure 10a) shows that there is more recirculation occurring in the normal impingement case. Thus, for this  $H/D$  case, the entrainment of the fluid into the impinging jet due to this recirculation is much stronger for the normal impingement case.

Finally, Figures 17a and 17b show the pressure contours in the  $x$ - $y$  plane at  $z/H = 1$  and  $z/H = 0$ , respectively. On the top plate, the pressure field is nearly uniform in the core of the jet and the pressure increase in the region where the fountain impinges on the top wall can be seen. On the bottom wall, the stagnation point is on the jet centerline, as mentioned earlier. Also, the pressure field is symmetric, unlike the oblique impingement case in which the pressure field on the ground was skewed, with compression occurring behind the stagnation point (Figure 11b).

The results presented above show the characteristic flow field associated with the normal impingement case. Simulations of excited normal impinging jets carried out earlier<sup>9,10</sup> also showed complex vortical motion. In the following sections, we discuss the effect of crossflow on the normal impinging jet.

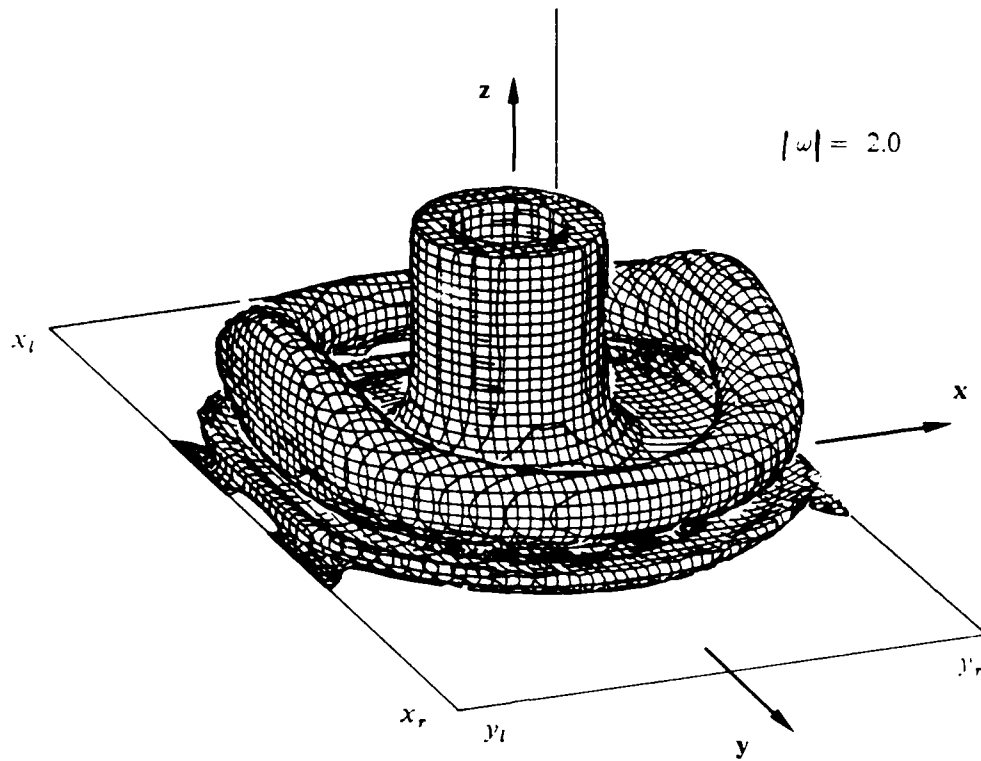
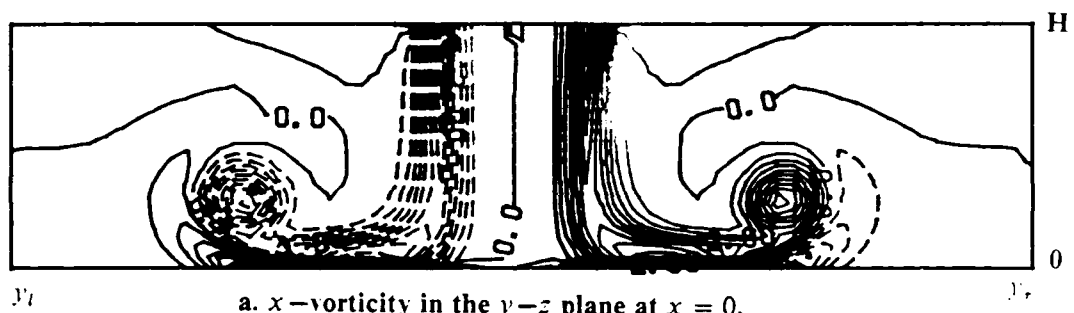
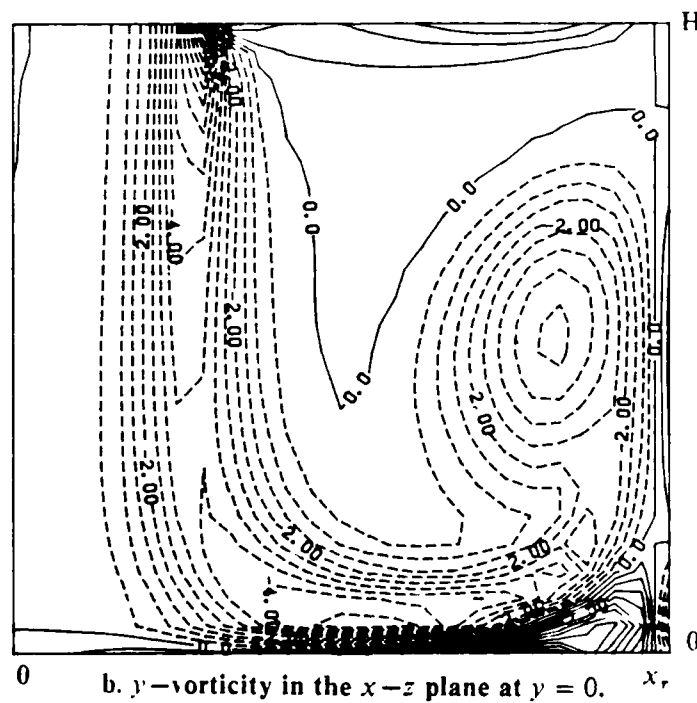


Figure 14. The three-dimensional perspective of the total vorticity,  $|\omega|$  for the normal impinging jet.

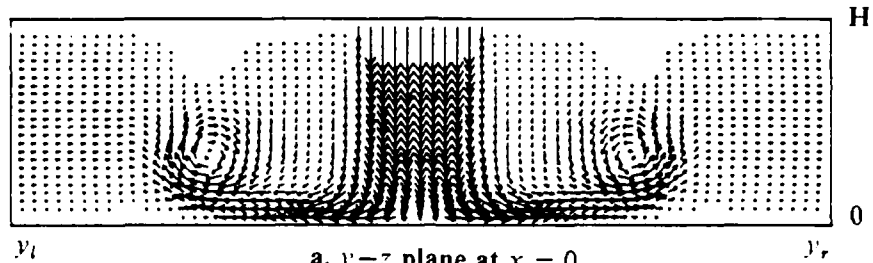


a.  $x$ -vorticity in the  $y$ - $z$  plane at  $x = 0$ .

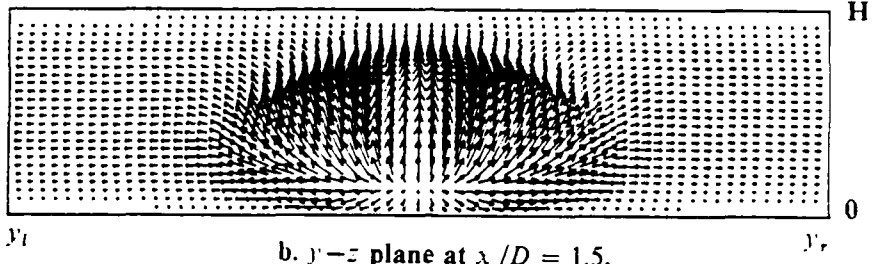


b.  $y$ -vorticity in the  $x$ - $z$  plane at  $y = 0$ .

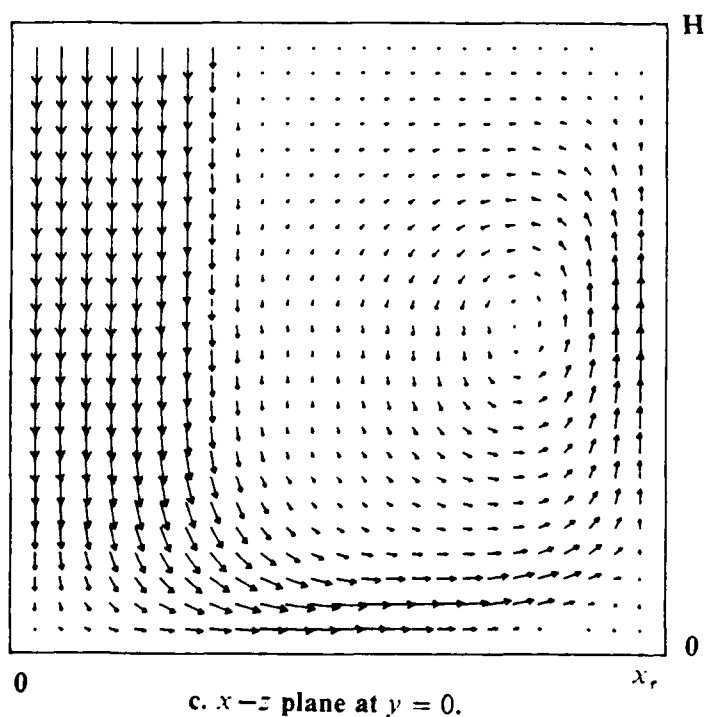
Figure 15. The vorticity contour fields for the normal impinging jet at  $t = 9.4$ . Contour interval is 0.5.



a.  $y-z$  plane at  $x = 0$ .

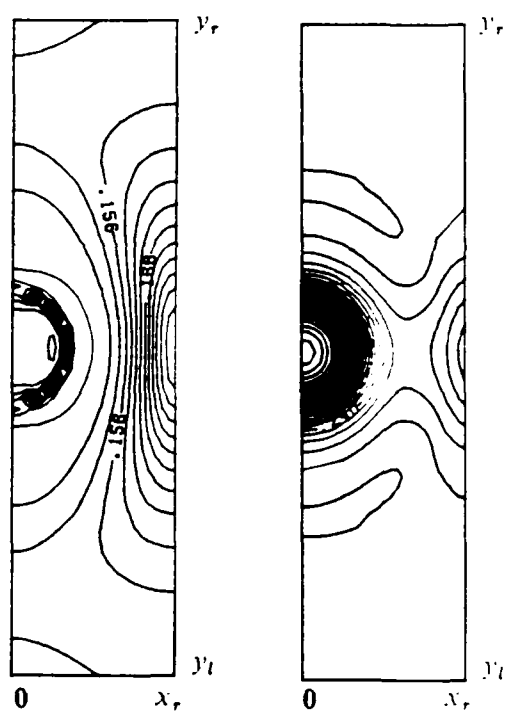


b.  $y-z$  plane at  $x/D = 1.5$ .



c.  $x-z$  plane at  $y = 0$ .

Figure 16. The velocity vector fields for the normal impinging jet at  $t = 9.4$ .



a. Top wall.

b. Ground plane.

Figure 17. The pressure contours in the  $x-y$  plane at  $t = 9.4$ .

### 5.3 The Normal Impinging Jet in Crossflow

The effect of crossflow on the dynamics of fluid motion in the impinging jet was studied by imposing a crossflow velocity at the inflow boundary at  $y/D = -3.0$ . Two types of simulations were performed. In the first simulation, the solution obtained at the end of the simulation with the normal impinging jet (Section 5.2) was used to initialize the flow field and then the crossflow was introduced. The second simulation was started with no flow in the computational domain and with the crossflow and the jet profile given in Equation (10) imposed simultaneously at  $t = 0$ . In terms of the flight configuration of a V/STOL aircraft in ground effect, these two scenarios correspond approximately to the cases in which (a) the aircraft executes a forward motion after hovering above the ground, and (b) the aircraft moves forward as soon as it lifts off the ground. Although the simulations were not carried out for a sufficient length of time to reach a quasi-stationary state, the results shown below indicate that the flow field associated with these two flight situations can be quite different. A constant crossflow velocity,  $v_o = V_c/U = 0.4$ , where  $V_c$  is the crossflow velocity, was used in all the simulations. The effect of varying the crossflow velocity will be studied in more detail in the next phase. Due to the computer and resource restrictions of the Phase I study, the effect of forcing was studied only for the latter case and only a few forcing cycles were performed.

Note that the presence of the fountain modifies the flow field significantly, a phenomenon that is absent in most of the earlier experimental and numerical studies of jets in crossflow.

#### 5.3.1 Forward Motion after Hovering (Case A)

To simulate this configuration, the crossflow was imposed at the inflow boundary at  $y/D = -3.0$  on the solution obtained for the normal impingement case described in Section 5.2. The crossflow was increased from  $v_o = 0$  to  $v_o = 0.4$  within 25 time steps, thereby simulating a rapid initial acceleration from stationary hover to forward motion at a constant velocity  $v_o$ . The simulation was continued without any external excitation and the data were obtained in detail at the end of the simulation. Due to time and resource constraints, the computation was not carried out for a sufficient length of time to reach a steady state. However, analysis of the data indicated that the solution was converging and would eventually reach a steady state. Some representative results are presented and analyzed here.

Figure 18a shows the three-dimensional perspective of the total vorticity  $|\omega|$  in the flow field at the end of this simulation. The jet had already impinged on the ground and the lift-off of the vortex ring into the fountain had begun (Figure 14) when the crossflow was initiated. The crossflow quickly forces back the forward part of the vortex ring on the ground (cf. Section 5.2, Figure 15a) and wraps the structure around the jet, since the front part of the impinging jet acts as an obstacle to the cross stream and thus the crossflow must go around it. The rear portion of the jet is also spread in the positive  $y$ -direction due to the crossflow.

To visualize the flow field in more detail, Figures 18b and 18c show the  $|\omega_x|$  and  $|\omega_y|$  components, respectively, in the same three-dimensional perspective. The  $|\omega_x|$  component dominates the vorticity in the ring ahead of the jet and in the ring behind it on the ground plane, whereas the vorticity in the fountain regions is dominated by the  $|\omega_y|$  component. It has been shown in earlier experimental studies (e.g., Andreopoulos and Rodi<sup>4</sup>) that the dynamics of the vorticity redistribution is quite complex for jets in crossflow. Further interpretation of the vorticity redistribution mechanism is given in some detail in the next section.

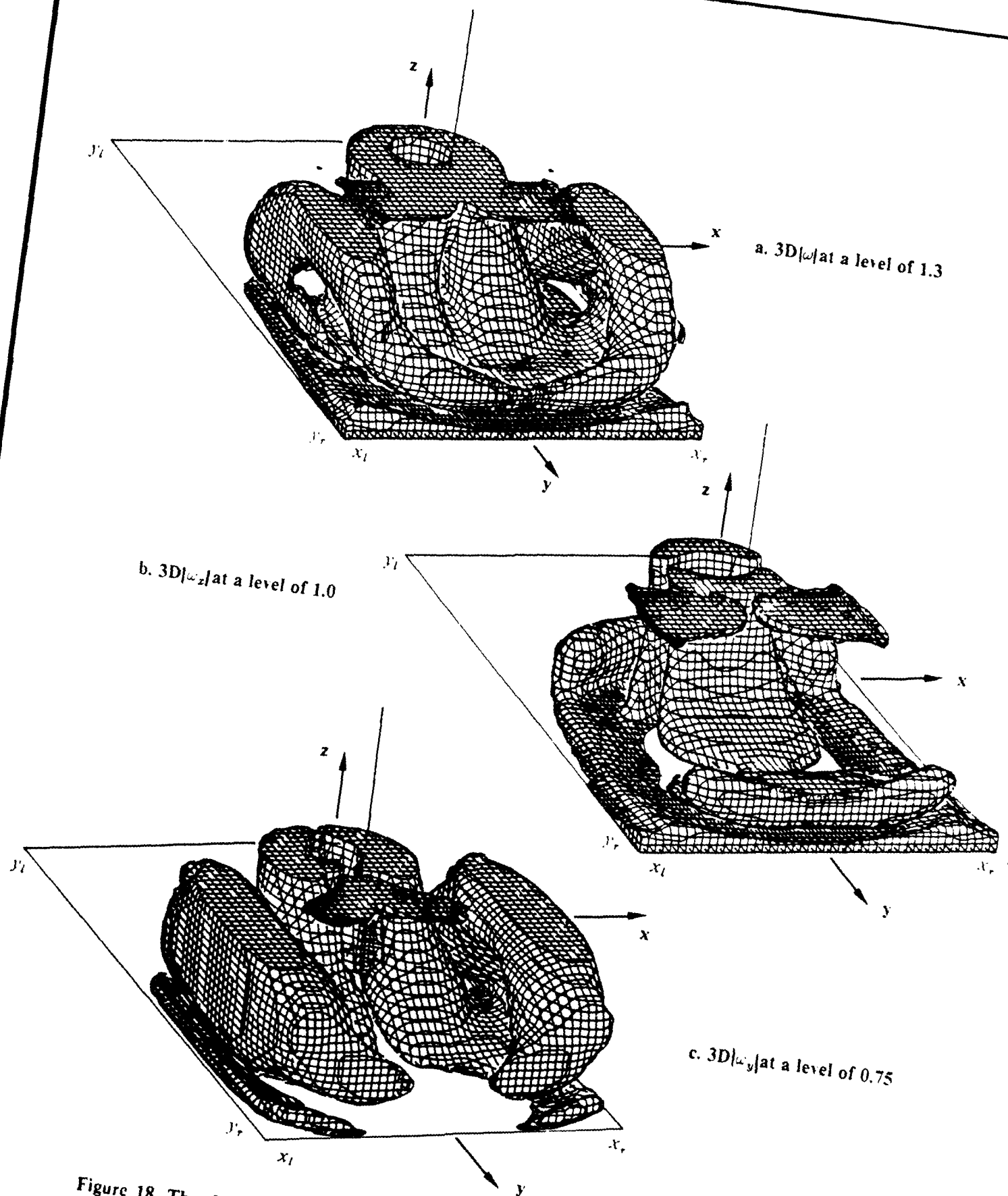


Figure 18. The three-dimensional perspective of the vorticity fields for normal impinging jet with crossflow (case A) at  $t = 13.1$ .

Figures 19a and 19b show the  $x$ -vorticity in the  $y$ - $z$  plane at  $x = 0$  and the  $y$ -vorticity in the  $x$ - $z$  plane at  $y = 0$ , respectively. The forward-moving part of the original vortical ring (Figure 15a) has been pushed back due to the crossflow and is now embedded near the jet impingement region. The jet itself is now inclined in the positive  $y$ -direction and significant secondary vorticity (dotted contours) is now present below the primary vortical region in the wall jet for  $y/D > 0$ . Part of the secondary vorticity in this region is now due to the vorticity in the ring ahead of the jet being forced back by the crossflow. In the plane of the fountain (Figure 19b), the vortical structure seen in the fountain axis for the normal impinging case (cf. Figure 15b) is now located away from the fountain axis. This is another effect of the crossflow on the fountain which results in adding a  $v$ -component of the velocity to the primarily  $w$ -component of velocity in the fountain upwash. The structures in the plane  $y/D = 1.5$  are more complex, as seen in Figure 19c. In this figure, note that the vorticity near the ground is associated with the diffused jet shear layer which has spread in the positive  $y$ -direction due to crossflow. The vortical structures near the top wall are part of the cross-sectional view of the vortex ring in the fountain. Figures 18 and 19 should be used together to visualize the complex flow field.

Figure 20 shows some representative velocity vector fields and the pressure field. Figure 20a shows the velocity field in the  $y$ - $z$  plane at  $x = 0$  corresponding to the vorticity field shown in Figure 19a. The crossflow at  $y/D = -3.0$  is clearly seen and the formation of the recirculation ahead of the jet is also observable. This recirculation is associated with the vortex seen in the vorticity field (Figure 19a). Due to the addition of the crossflow component, the outflow velocity in the wall jet region is increased. Notice also that the stagnation point is moved downstream of the  $y = 0$  location where it originally was before the crossflow was started. The symmetric fan-like upwash for the normal impingement case (Figure 16b) at the plane of the fountain at  $x/D = 1.5$  is no longer present with crossflow, as can be seen in Figure 20b. The upflow is now skewed in the positive  $y$ -direction due to the addition of the crossflow velocity to the upwash velocity, causing the flow to turn downstream. This would result in a much weaker lift-off effect (if any) on the top wall.

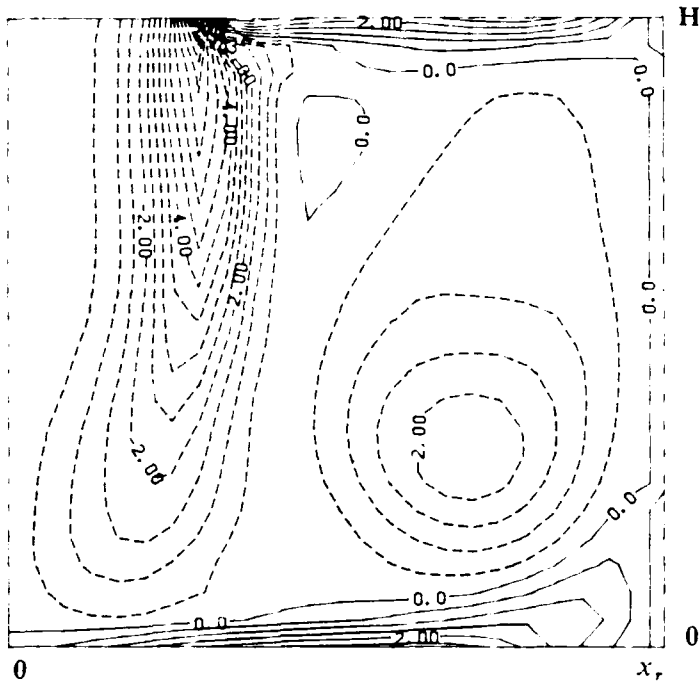
The pressure contours in the  $y$ - $z$  plane shown in Figure 20c illustrate the skewness in the positive  $y$ -direction due to crossflow. There is a low-pressure region associated with the vortex ahead of the jet. The stagnation point is no longer on the jet center line and is moved by about  $0.27D$  to the right of the  $y = 0$  location.

Figures 20d and 20e show the velocity vector field in the  $x$ - $z$  plane at  $y = 0$  and  $y/D = 1.5$ , respectively. The recirculation observed for the normal impingement case (Figure 16c) is no longer present in the center plane, and the upwash velocity in the fountain is considerably weaker. This is not surprising since, as mentioned earlier, the crossflow in the  $y$ -direction enforces a net velocity in that direction which is out of the frame of this figure. Halfway to the outflow at  $y/D = 1.5$ , we see significant recirculation due to the complex vortex motion observed in Figure 19c. The upwash in the fountain region is quite strong in this plane.

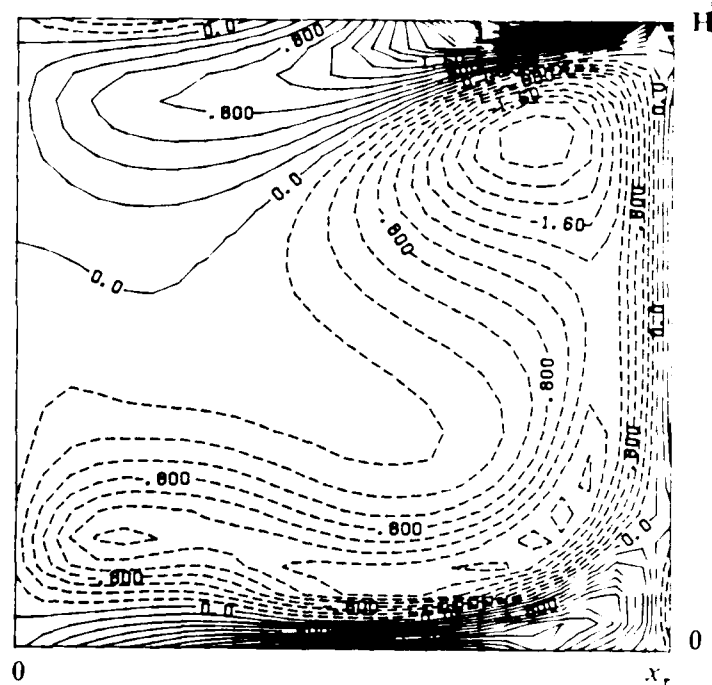
Figure 21 shows some representative velocity profiles in the flow field. For comparison, the velocity profiles for the normal impingement case are also shown in these figures. Figure 21a shows the  $v$ -component profiles in the  $y$ - $z$  plane at  $x = 0$ . For the normal impingement case, the velocity profiles are symmetric about the  $y = 0$  location, with the wall jet growing uniformly toward both outflow boundaries. With crossflow, the profiles at all the locations show motion primarily in the positive  $y$ -direction. The wall boundary layer due to the crossflow can be seen in this figure. The incoming crossflow velocity profile in the potential flow region is uniform across the entire  $H/D$  at  $y/D = -2.33$



a.  $x$ -vorticity in the  $y$ - $z$  plane at  $x = 0$ .

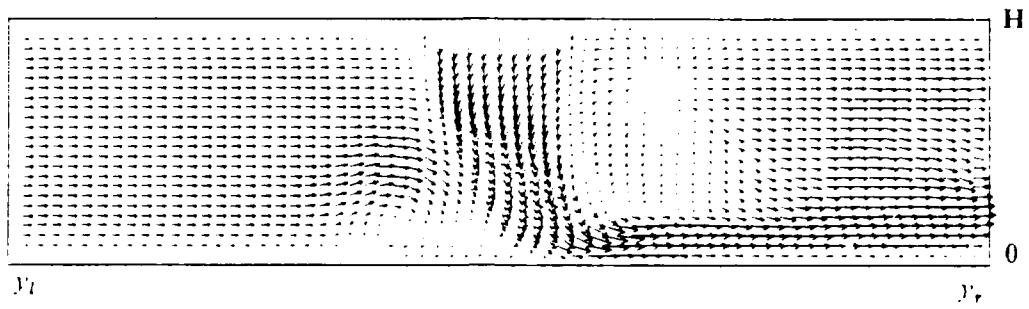


b.  $y$ -vorticity in the  $x$ - $z$  plane at  $y = 0$ .

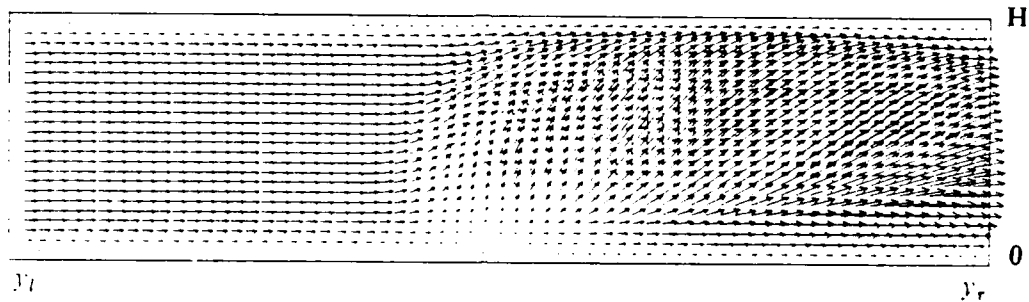


c.  $y$ -vorticity in the  $x$ - $z$  plane at  $y/D = 1.5$ .

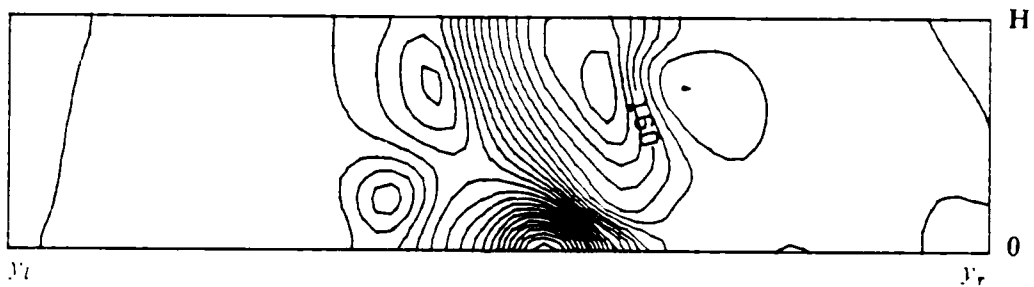
Figure 19. The vorticity contour fields for normal impinging jet with crossflow (case A) at  $t = 13.1$ . Contour interval for figures 19a and 19b is 0.5 and for figure 19c is 0.2.



a. Velocity vectors in the  $y-z$  plane at  $x = 0$ .

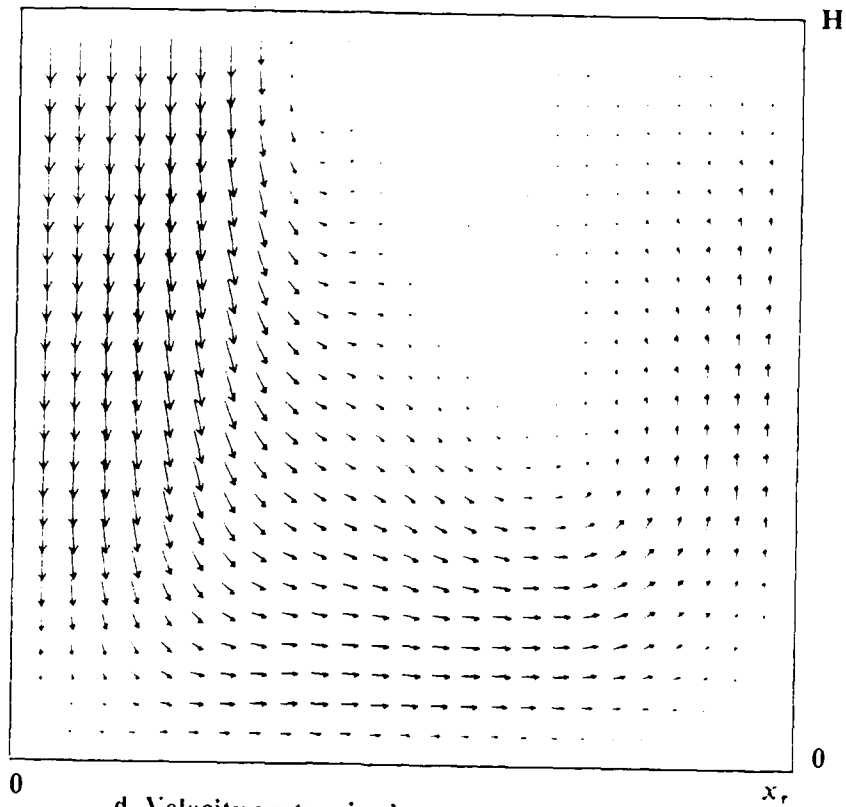


b. Velocity vectors in the  $y-z$  plane at  $x/D = 1.5$ .

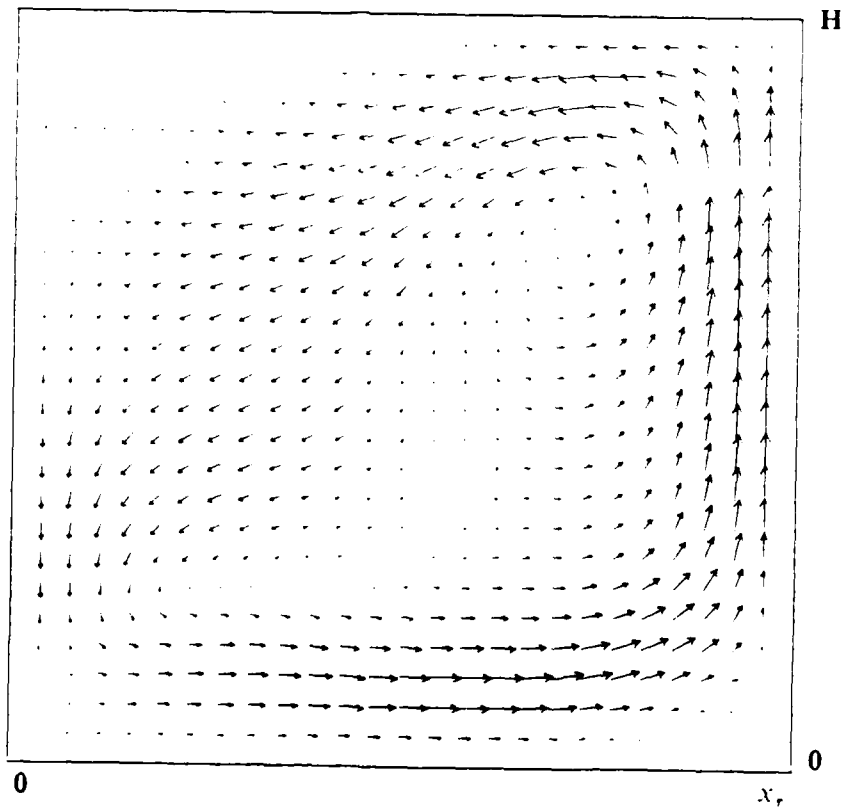


c. Pressure contours in the  $y-z$  plane at  $x = 0$ .

Figure 20. The velocity vector fields and pressure contours for normal impinging jet with crossflow (case A) at  $t = 13.1$ .



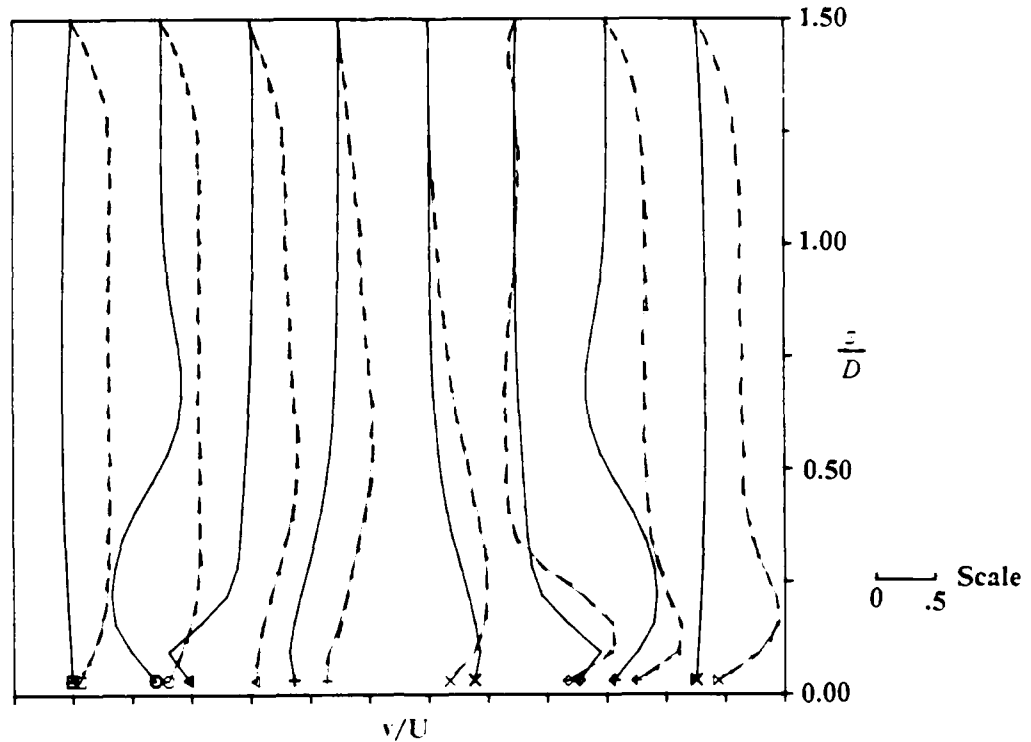
d. Velocity vectors in the  $x-z$  plane at  $y = 0$ .



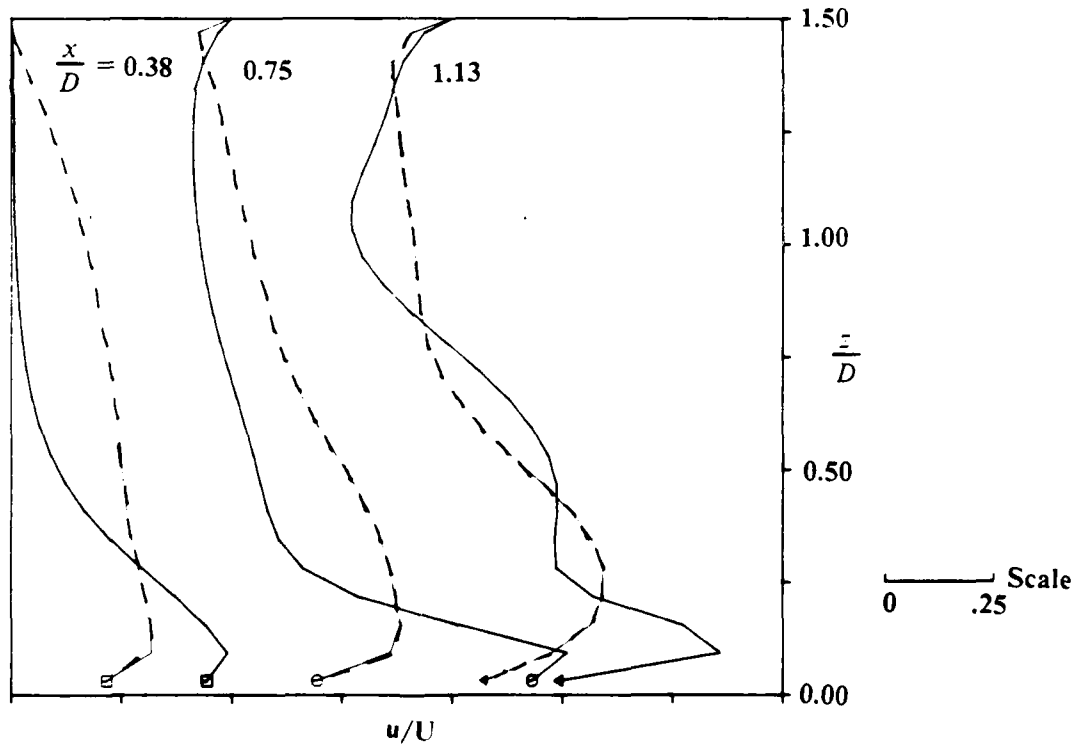
e. Velocity vectors in the  $x-z$  plane at  $y/D = 1.5$ .

Figure 20. The velocity vector fields and pressure contours for normal impinging jet with crossflow (case A) at  $t = 13.1$  (Cont.)

$$\frac{y}{D} = -2.33 \quad -1.67 \quad -1.00 \quad -0.33 \quad 0.33 \quad 1.00 \quad 1.67 \quad 2.33$$



a.  $v$ -velocity profiles in the  $y-z$  plane at  $x=0$ .



b.  $u$ -velocity profiles in the  $x-z$  plane at  $y=0$ .

Figure 21. The comparison between the velocity profiles in the flowfield for the normal impinging jet at  $t=9.4$  and the normal impinging jet with crossflow at  $t=13.1$ .

———— Without Crossflow      - - - - With Crossflow

but becomes nonuniform with increasing  $y/D$ . This is the result of the reversal of the fluid in the wall jet in the region  $y/D < 0$  to the positive  $y$ -direction. The wall boundary layer grows larger for the case with crossflow for  $y/D > 1.5$  since now the crossflow velocity component is added to the velocity in the wall boundary layer. All these features occurred as expected and clearly show the effect of crossflow.

Figure 21b shows the  $u$ -velocity component in the  $x$ - $z$  plane at  $y = 0$ . In this plane, the profiles are quite different. The normal impingement velocity profiles are now more developed than in the case with crossflow, with significant reverse flow near the top wall due to the upwash spreading effect. With crossflow, however, most of the fluid is forced to move to the outflow ( $y$ - $z$  plane) direction and thus the motion toward the fountain region in the  $x$ - $z$  plane is reduced. This then results in reduced  $u$ -velocities as seen in this figure. Consequently, the upward motion in the fountain is weakened and the reverse wall jet on the top wall is also reduced.

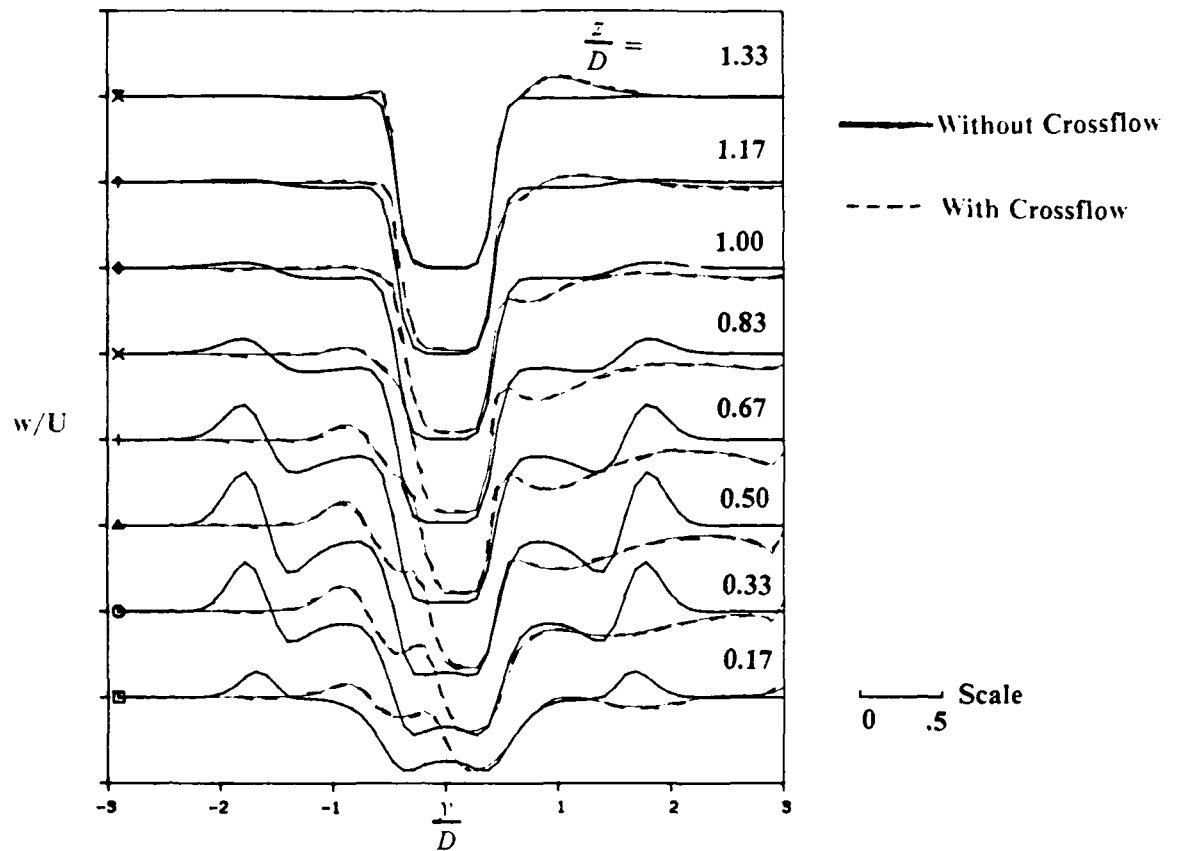
Finally, Figure 21c shows the  $w$ -velocity in the  $y$ - $z$  plane at  $x = 0$ . The velocity profiles in the jet for the normal impingement case is again symmetric and the spreading of the jet is clearly seen. Near the initial jet exit region ( $z/H > 0.75$ ), the effect of crossflow is insignificant since the jet peak velocity is 2.5 times the crossflow velocity. As the jet approaches the ground plane, however, the peak velocity in the jet potential core decreases as it spreads and thus, closer to the ground, the crossflow velocity is of the same order as the  $w$ -component. This causes the jet to bend toward the positive  $y$ -direction, and the spreading character of the jet is modified by the crossflow. The crossflow also forces the jet to impinge a short distance downstream of the normal impingement location.

In this section, we have described some of the effects of crossflow on the fluid motion of a normal impinging jet. The characteristic changes in the features of vortical and fluid motion due to crossflow were highlighted through comparison with the reference case of normal impingement without crossflow. Although the simulations were not carried out for a sufficient length of time to reach a quasi-stationary state, the general features of the initial modification of the flow field are in good qualitative agreement with experimental observations.

### 5.3.2 Forward Motion without Hovering (Case B)

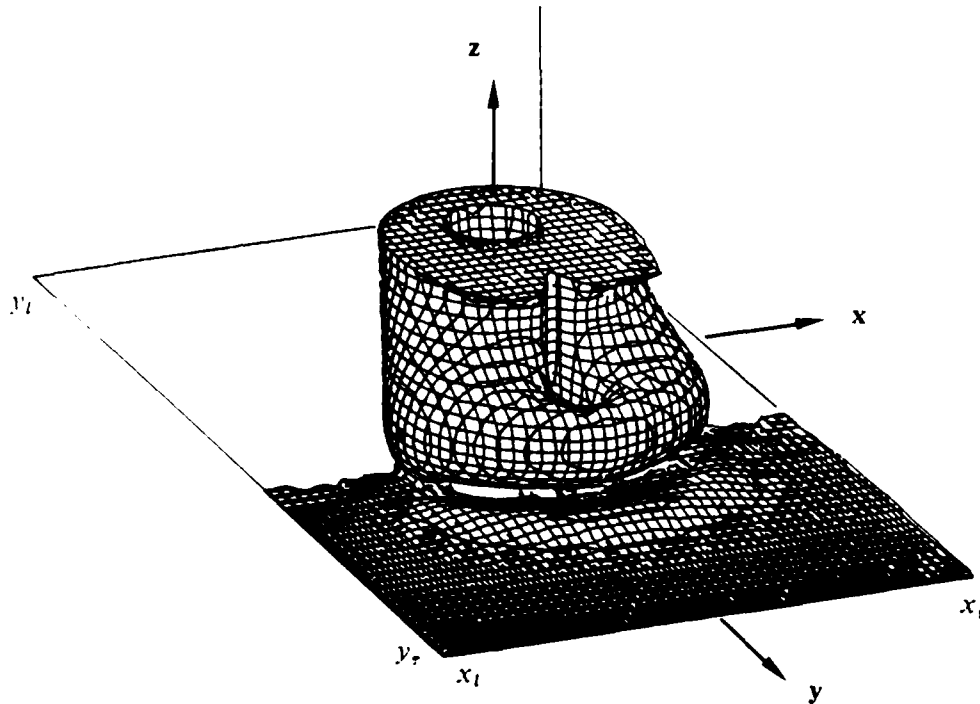
For this flight configuration, the crossflow was begun at  $t = 0$ , which is when the jet comes out of the jet exit plane at  $z/H = 1$ . The crossflow was again ramped to the steady value as before. Since the crossflow velocity is relatively weaker than the jet velocity and since the jet-to-ground distance is quite small for this simulation, the jet still impinges on the ground. However, the flow field for this case develops in quite a different manner than in the simulation discussed in Section 5.3.1. These differences are highlighted below.

Figure 22a shows the three-dimensional perspective of the total vorticity in the jet at the time the jet has reached the ground. There is no clear indication of the starting vortex observed in the earlier simulation, and the jet shear layer is now wrapped behind the jet. This can be seen more clearly in Figures 22b and 22c, which show the  $x$ -vorticity in the  $y$ - $z$  plane at  $x = 0$  and the  $y$ -vorticity in the  $x$ - $z$  plane at  $y = 0$ , respectively. Due to the crossflow, the jet shear layer is inclined in the front and more spread out in the back (Figure 22b). The vortex seen ahead of the jet in Figure 19a is no longer present since now the vortex ring does not exist on the ground. There is also no indication of the fountain, which was expected since the wall jet spreading on the ground plane has not yet occurred.



c.  $w$ -velocity profiles in the  $y$ - $z$  plane at  $x = 0$ .

Figure 21. The comparison between the velocity profiles in the flowfield for the normal impinging jet at  $t = 9.4$  and the normal impinging jet with crossflow at  $t = 13.1$ . (Cont.)

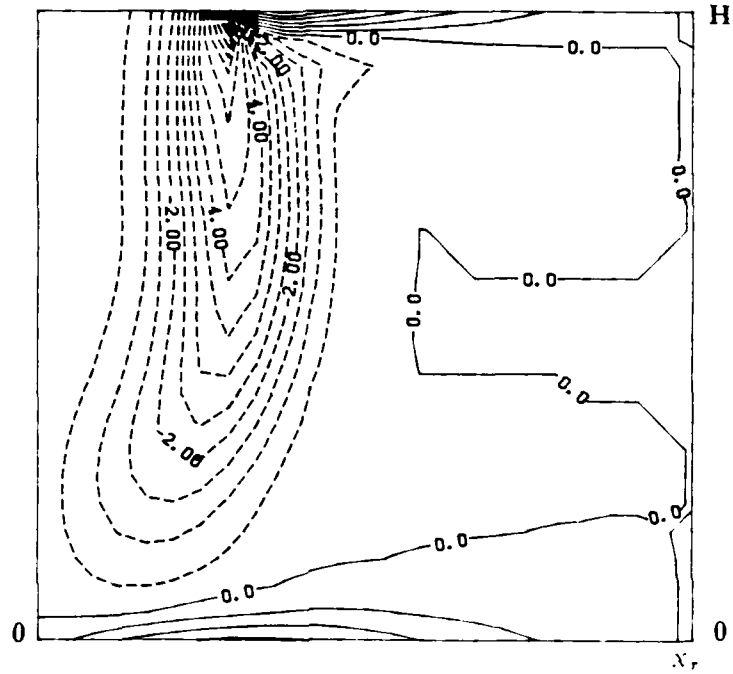


a. 3D total vorticity,  $|\omega|$  at a level of 1.3

Figure 22. The vorticity fields for the normal impinging jet with crossflow (case B) at  $t = 3.8$ .

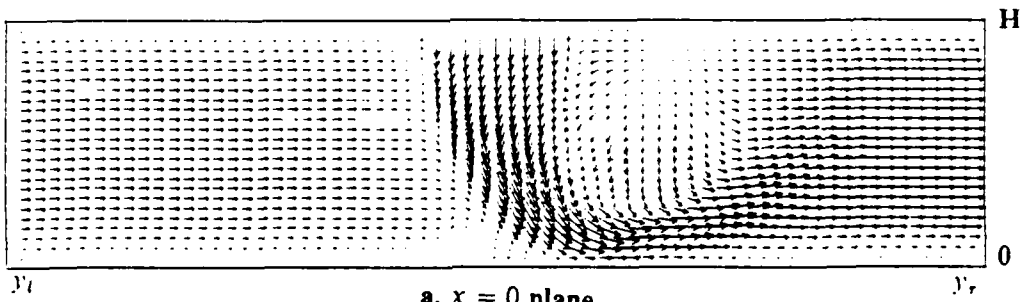


b.  $x$ -vorticity in the  $y$ - $z$  plane at  $x = 0$ . Contour interval is 0.5.

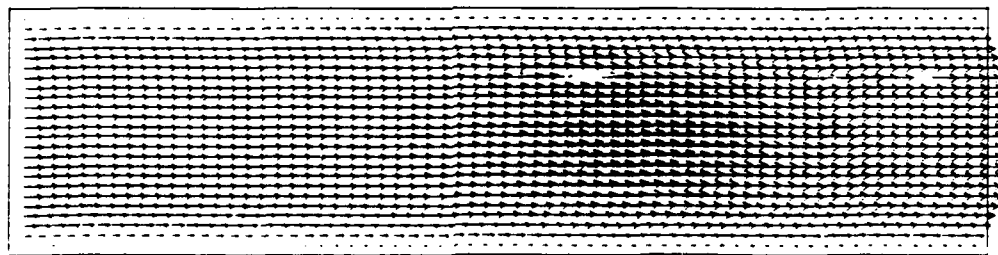


c.  $y$ -vorticity in the  $x$ - $z$  plane at  $y = 0$ . Contour interval is 0.5.

Figure 22. The vorticity fields for the normal impinging jet with crossflow (case B) at  $t = 3.8$  (cont.).



a.  $x = 0$  plane.



b.  $x/D = 1.5$  plane.

Figure 23. The velocity vector fields in the  $y$ - $z$  plane for normal impinging jet with crossflow (case B) at  $t = 3.8$ .

The bending of the jet due to crossflow seen in Figure 22b is also clearly seen in the velocity vector field in the same plane shown in Figure 23a. Although not very clear in this figure, there is a small recirculation region ahead of the jet near the impingement point. The velocity vector field in the plane of the fountain at  $x/D = 1.5$  is shown in Figure 23b. This figure shows that the fluid flow in this plane is primarily in the outflow direction with no significant upwash.

The computations were then continued with external excitation at the same Strouhal number of 0.47 as before. A forcing amplitude of  $0.1U$  was used and the computations were continued for approximately four forcing cycles. The data for the last forcing cycle were then analyzed in detail.

Figure 24a shows the three-dimensional perspective of the vorticity in the jet at the end of the forced simulation. Comparison with Figure 18 from the earlier study of the crossflow immediately reveals significant differences. For example, the fountain does not form at all. The motion toward the fountain axis is completely inhibited by the crossflow and most of the fluid is swept out to the outflow direction. Therefore, in this case there will be no lift-off effect of the fountain. There is a clear indication of the counterrotating vortical structure formed by the jet due to cross flow. This is quite similar to the kidney-shaped structures observed for free jets in crossflow,<sup>4,22,41</sup> which have been studied in great detail in the past. As discussed below, however, the close proximity of the ground plane modifies the shape. The wrapping of the vortical structure around the jet is also seen in this figure. This feature is similar to that observed in the earlier simulation (see Figure 18).

To visualize the streamwise ( $\omega_y$ ) vortices formed due to crossflow, Figure 24b shows the  $|\omega_y|$  component in the same perspective view. Comparing this figure to Figure 24a, which shows the total vorticity, it becomes quite apparent that the  $|\omega_y|$  component of the vorticity dominates the entire flow field. This is in contrast to the earlier simulation, where the presence of the fountain results in redistribution of the total vorticity into both the  $x$ - and  $y$ -components (Figures 18b and 18c).

To illustrate the vortex motion in the jet, Figures 25a and 25b show the  $x$ -vorticities in the  $y$ - $z$  plane at  $x = 0$  half a forcing cycle apart. The impinging jet is swept back, similar to that observed in the earlier simulation (Figure 19a). Vortex shedding again occurs at the forcing frequency; however, the motion in the shear layer facing the crossflow is not very clear. The effect of the crossflow is to compress the shear layer in the direction of the crossflow, and some of the vorticity in the jet shear layer facing the crossflow is carried into the wall jet. The vortical ring that is shed due to forcing is highly skewed to the outflow direction and is elongated in the wall jet region. Notice the apparent termination of the wall jet around  $y/D = 2$ . This is not actually occurring and is due to the fact that further downstream the  $\omega_x$  component is much weaker than the contour interval used for this figure. Furthermore, as shown earlier (Figure 24b), most of the vorticity is contained in the  $\omega_y$  component and thus rapid depletion of the  $\omega_x$  component is not surprising. In fact, it appears that the three-dimensional redistribution of the total vorticity in the flow field is quite complex, as seen in experiments,<sup>4</sup> and more detailed simulations are required to understand the detailed dynamics of the vortical motion in this type of flow field.

The  $y$ -vorticity in the  $x$ - $z$  plane at  $y = 0$  and  $y/D = 1.5$  is shown in Figures 25c and 25d, respectively. Notice the complete absence of a fountain in the  $y = 0$  plane. In fact, it appears that the shed vortex reaches the ground, is then surrounded by the crossflow, and thus is trapped at the ground. Subsequently, this vortex ring is lifted off the ground in the outflow direction, as can be seen in the three-dimensional perspective (Figure 24). Visualization at various other times in the forcing cycle have shown that the picture in Figure 25c does not change significantly.

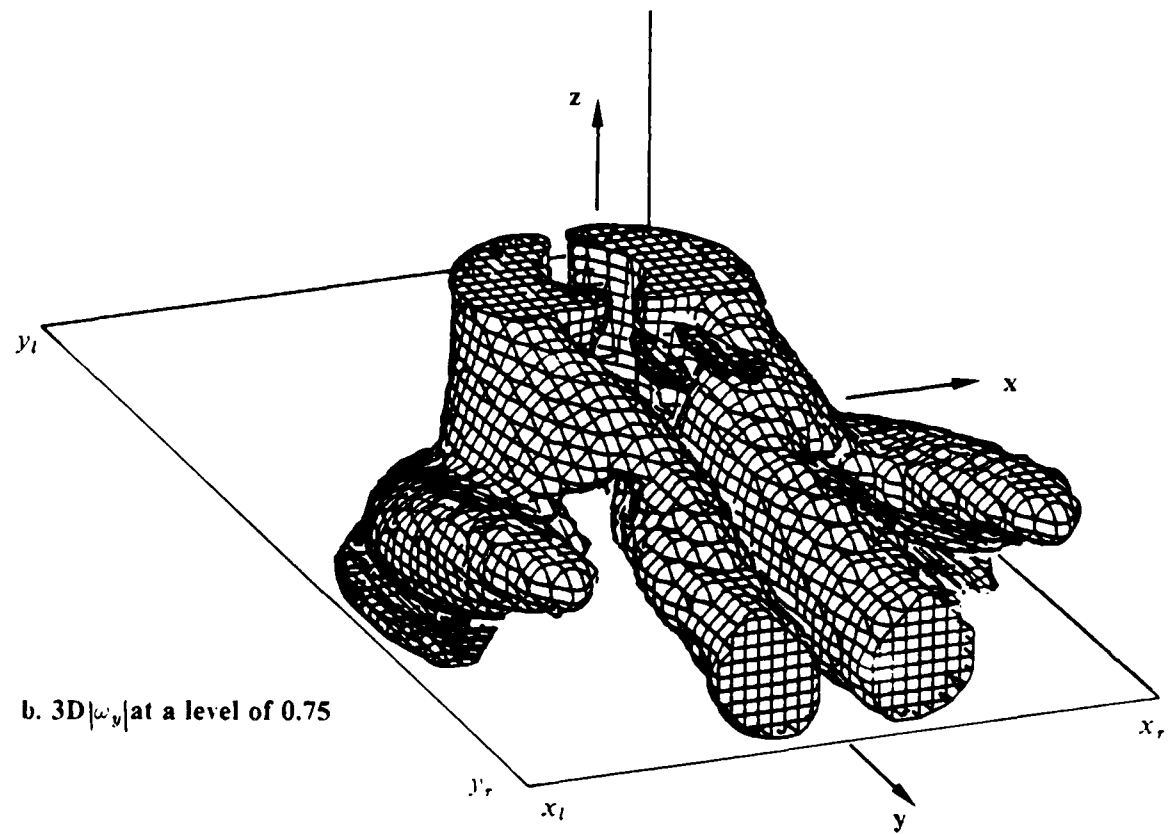
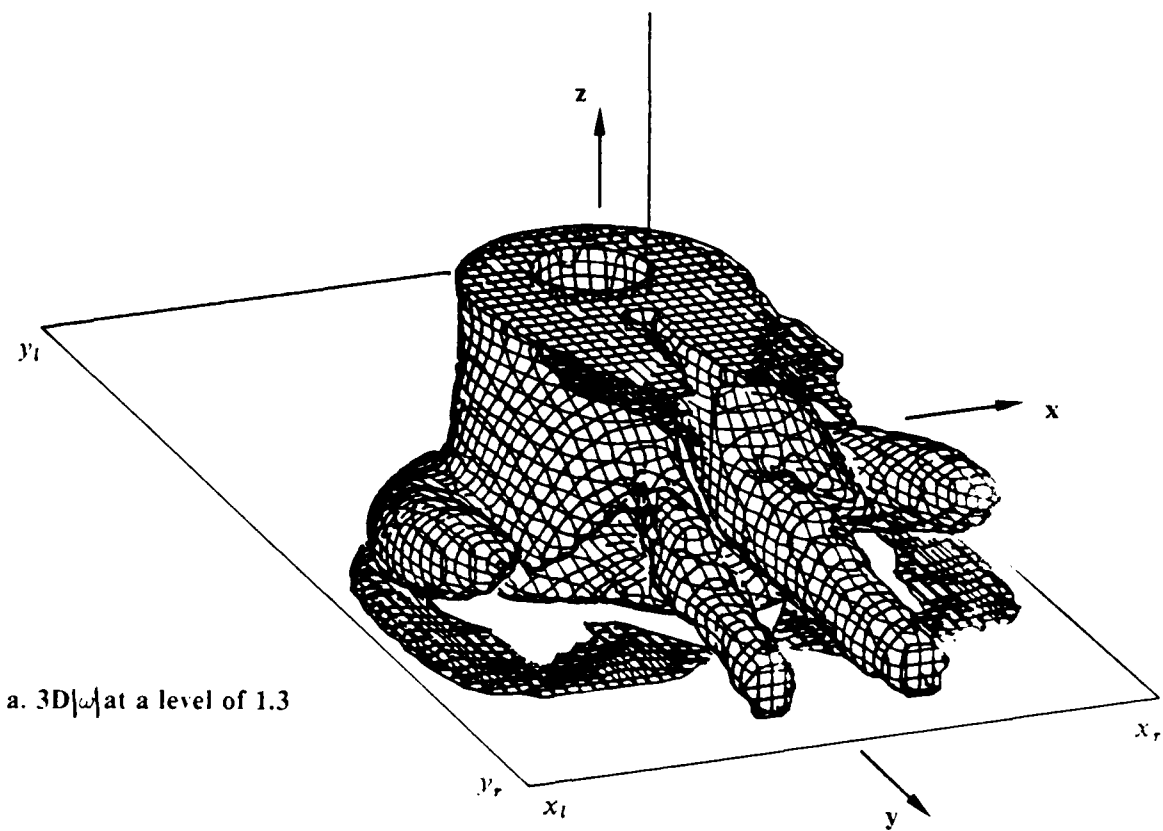
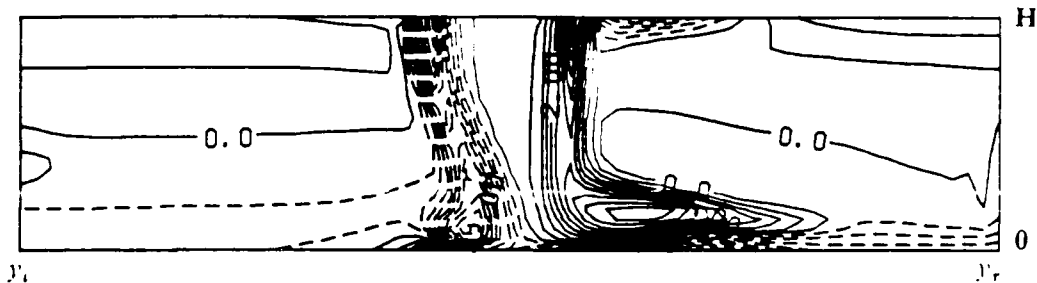
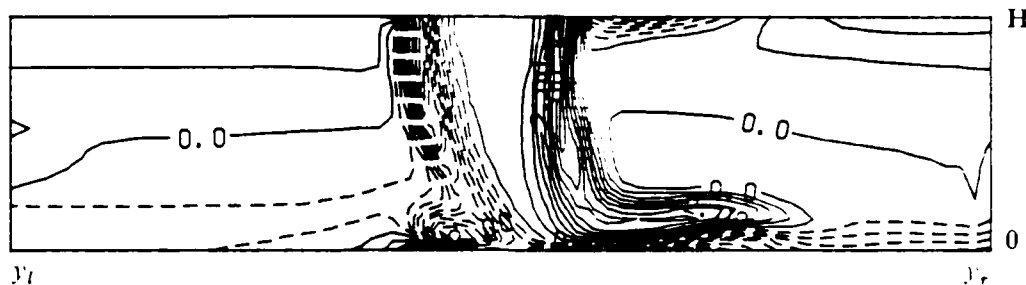


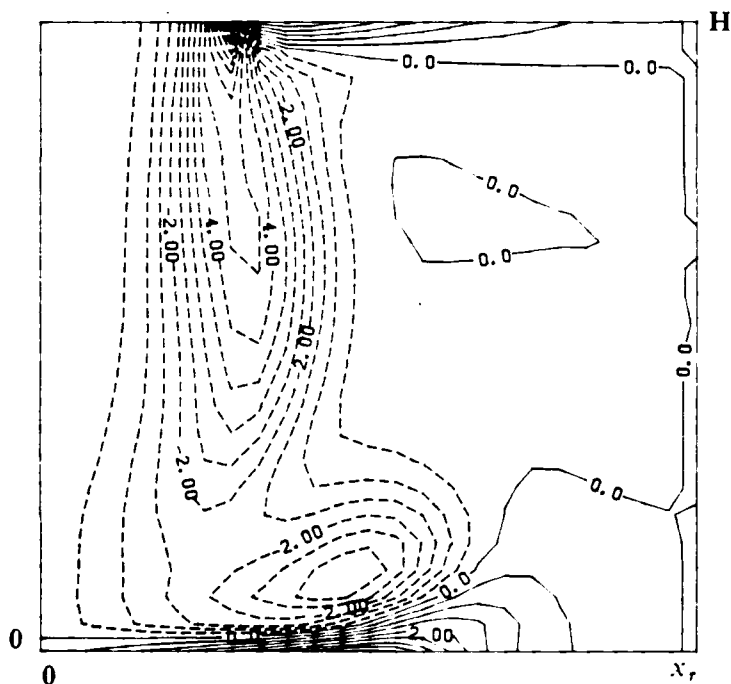
Figure 24. The three-dimensional perspective of the vorticity for normal impinging jet with crossflow (case B) at  $t = 13.1$ . Jet forced at  $St = 0.47$ .



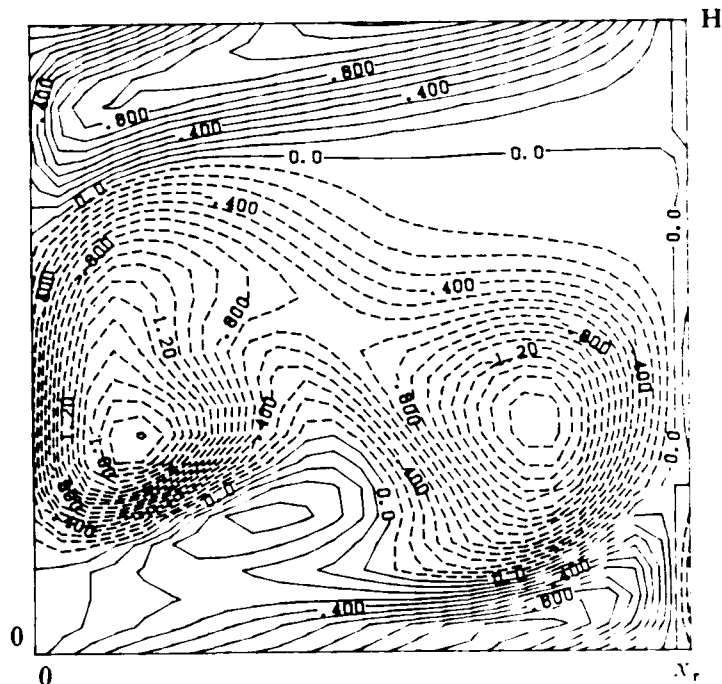
a.  $x$ -vorticity in the  $y$ - $z$  plane at  $x = 0$  at  $t = 10.8$ .



b.  $x$ -vorticity in the  $y$ - $z$  plane at  $x = 0$  at  $t = 12.2$ .



c.  $y$ -vorticity in the  $x$ - $z$  plane at  $y = 0$  at  $t = 12.2$ .



d.  $y$ -vorticity in the  $x$ - $z$  plane at  $y/D = 1.5$  at  $t = 12.2$ .

Figure 25. The vorticity contours in the flow field for the forced normal impinging jet with crossflow (case B). Contour interval is 0.5 for figures 25a-25c and 0.1 for figure 25d.

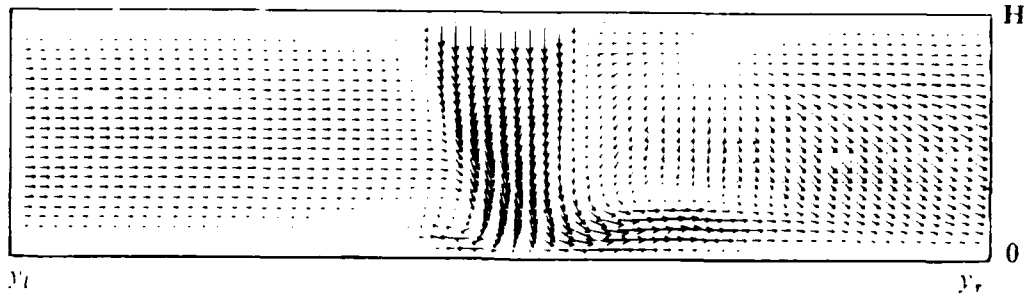
The  $y$ -vorticity in the  $y/D = 1.5$  plane (Figure 25d) shows complex vortical motion occurring at this location. The two vortical structures seen in this figure *should not* be confused with the two streamwise vortex tubes seen in Figure 24. This is because the full jet in Figure 24 is shown by flipping the computed  $0 < x/D < 1.5$  domain to the  $-1.5 < x/D < 0$  domain by using the symmetry condition at  $x = 0$ . In the present figure (Figure 25d), only one-half of the full jet is shown (i.e.,  $0 < x/D < 1.5$ ). Thus, the vortical structure on the left in this figure corresponds to the streamwise vortex tube in Figure 24, and the structure on the right is the cross-sectional image of the curved vortex ring from the front of the jet. The kidney-shaped structure in Figure 24b would be formed by the vortex to the right of the  $x = 0$  axis and *its image* to the left of the  $x = 0$  axis. Furthermore, due to symmetry, it is clear that the image will have *positive*  $\omega_y$  vorticity, which is opposite to the *negative*  $\omega_y$  vorticity in this figure. By reviewing this figure along with the three-dimensional perspectives shown in Figure 24, these features can be visualized.

Figure 26 shows the velocity vector fields in the various planes for this simulation. Figures 26a and 26b are at the same times as shown in Figures 25a and 25b. The presence of a rotating region ahead of the jet is clearly seen. However, through comparison with the vorticity contours at the same location and time, it is clear that whereas the recirculation region is quite large, the associated  $|\omega_x|$  vorticity in this region is quite small. In experimental studies, the presence of a *vortex* is usually identified from the streakline patterns. This corresponds to the velocity vector field as shown in these figures. However, as mentioned earlier, to identify this region as a vortical region would not be correct, as can be seen by comparing Figure 25 with this figure.

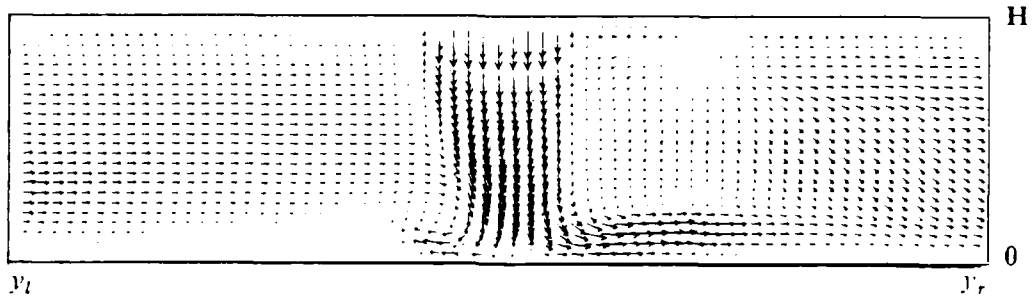
In the plane of the fountain at  $x/D = 1.5$  (Figure 26c), the flow is mostly in the outflow direction and thus there is no significant upwash occurring. Although there is some upward motion in the flow field, this motion is turned back to the outflow direction as the outflow boundary is approached.

Figures 26d and 26e show the velocity vector field in the  $x$ - $z$  plane at  $y = 0$  and  $y/D = 1.5$ , respectively, and correspond to the vorticity fields shown in Figures 25c and 25d. It can be seen that the impinging jet starts to spread toward the fountain but, due to the effect of the crossflow, the velocity vectors change direction and are predominantly in the  $y$ -direction, which is out of the frame of this view. The recirculation caused by the streamwise vorticity behind the jet and the vortex ring from the ground in the  $x$ - $z$  plane can be seen in Figure 26e quite clearly. Again, the recirculation on the left near the  $x = 0$  axis corresponds to the streamwise vortex tube related to the kidney-shaped structures observed in the vorticity plots; the motion on the right is due to the vortex ring lifting off the ground. Furthermore, due to symmetry at  $x = 0$ , the recirculation to the left of the  $x = 0$  line would be opposite to the recirculation observed to the right of the  $x = 0$  axis; thus, the recirculation pattern associated with the streamwise vortex tubes is counterrotating. This is again in good agreement with experimental observations.<sup>4,22</sup>

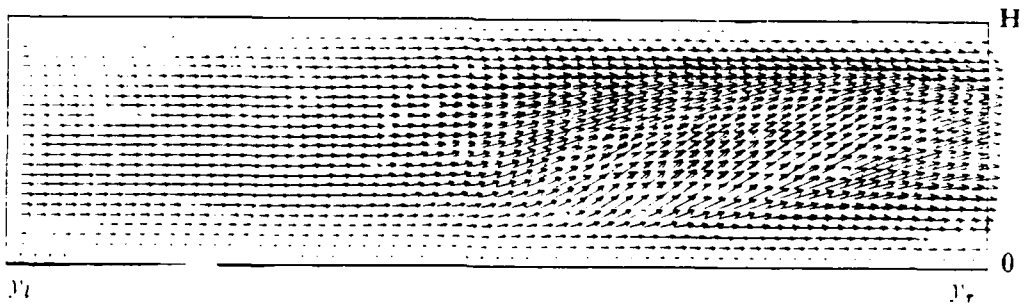
Figures 27a and 27b show the pressure contours in the  $y$ - $z$  plane at  $x = 0$  at the same times as are shown in Figures 25 and 26. The peak stagnation pressure occurs slightly downstream of the jet centerline (i.e.,  $y = 0$ ) at a location  $0.21D$ . This is quite similar to the value obtained even when there is a fountain present (Figure 20c). The peak value and the location are not significantly affected by the forcing. The pressure contours in the  $x$ - $y$  plane at  $z/H = 0$  (i.e., the ground plane) are shown in Figure 27c. The compression in the front of the jet due to crossflow can be seen. This is again as expected from previous experimental observations.



a.  $y-z$  plane at  $x = 0$  at  $t = 10.8$ .



b.  $y-z$  plane at  $x = 0$  at  $t = 12.2$ .



c.  $y-z$  plane at  $x/D = 1.5$  at  $t = 12.2$ .

Figure 26. The velocity vector fields in the flow field for the forced normal impinging jet with crossflow (case B).

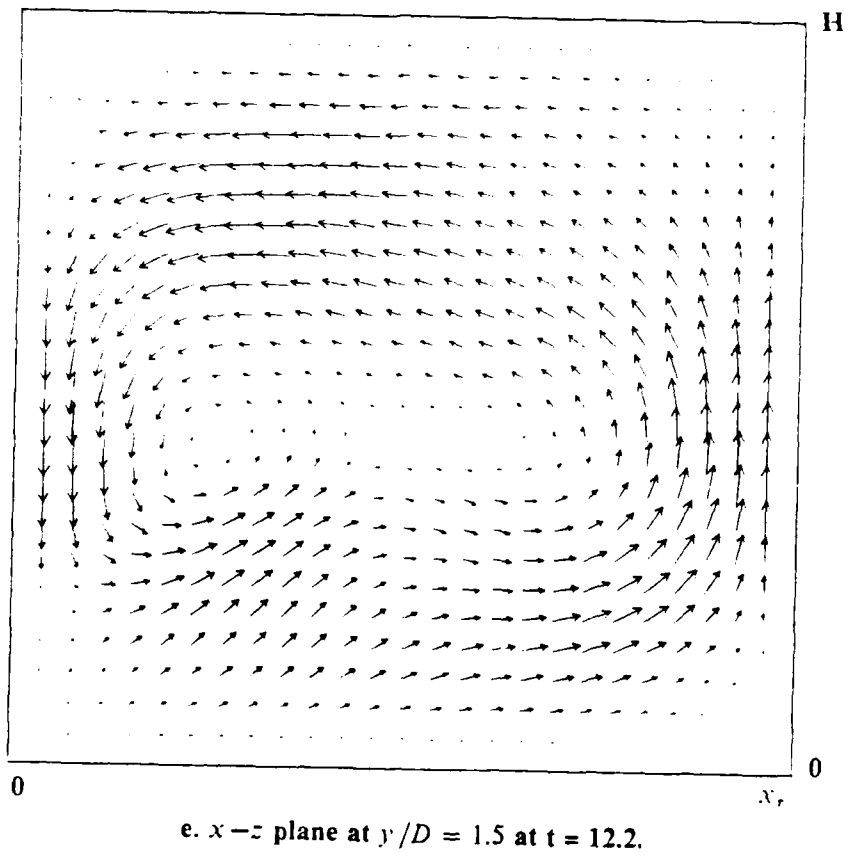
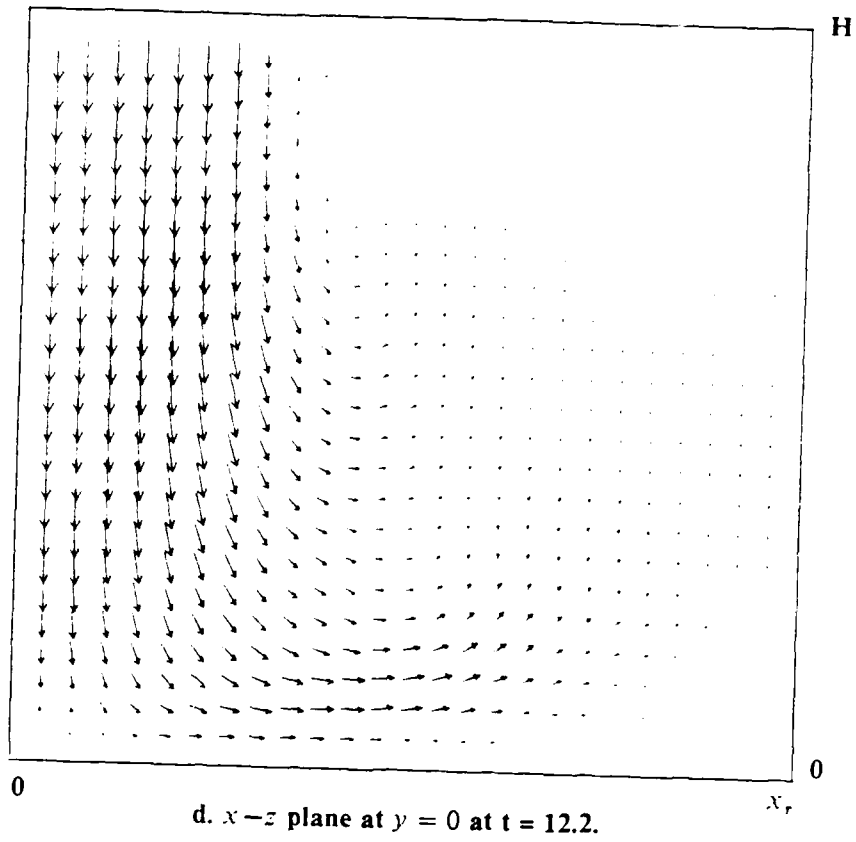
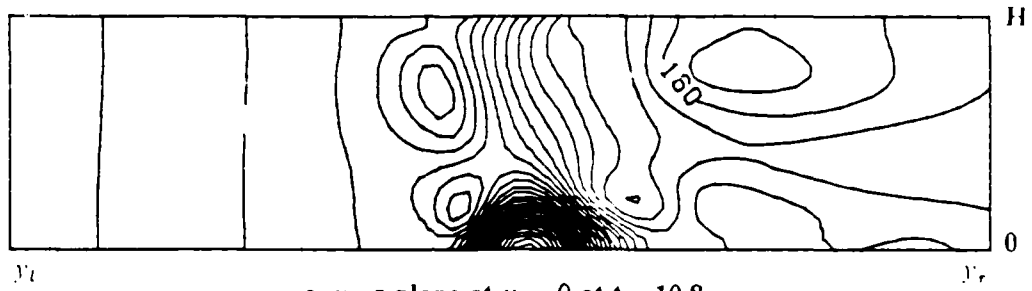
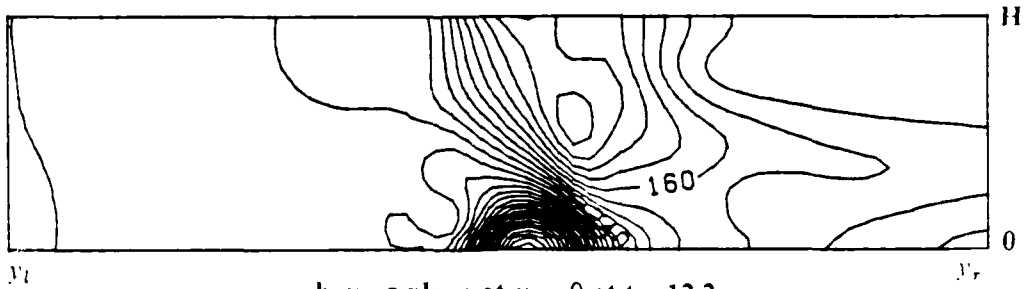


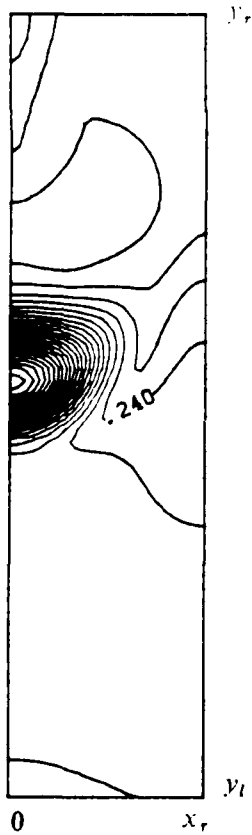
Figure 26. The velocity vector fields in the flow field for the forced normal impinging jet with crossflow (cont.).



a.  $y-z$  plane at  $x = 0$  at  $t = 10.8$ .



b.  $y-z$  plane at  $x = 0$  at  $t = 12.2$ .



c.  $x-y$  plane at  $z/H = 0.0$  at  $t = 12.2$ .

Figure 27. The pressure contours in the flow field for the forced normal impinging jet with crossflow (case B). Contour interval is 0.02.

Typical velocity profiles in the flow field are shown in Figure 28. Figure 28a shows the  $v$ -velocity profiles in the  $y$ - $z$  plane at  $x = 0$  for the two times shown earlier. The incoming crossflow velocity is unaffected by the effect of forcing of the impinging jet, as was expected. At around  $y/D = 0.33$ , there is definite negative  $v$ -velocity near the wall. This is related to the recirculation region seen in the velocity vector diagrams. In the positive  $y$ -direction, the wall jet growth is similar to the growth observed in the earlier simulation (cf. Section 5.3.1).

Figure 28b shows the corresponding  $u$ -velocity profiles in the  $x$ - $z$  plane at  $y = 0$ . The wall jet grows toward the fountain axis, but due to the crossflow effect, the peak values are quite small. There is not much evidence of the reverse wall jet on the top wall near  $x/D = 1.17$ , which is close to the fountain axis at  $x/D = 1.5$ .

Figure 28c shows the  $w$ -velocity profiles in the impinging jet for the two times of the forcing cycle. The effect of forcing does not significantly affect the jet velocity profile except near the potential core. The spreading of the jet is quite clear and is similar to that observed earlier. In the upstream direction ( $y/D < 0$ ), there are hardly any noticeable differences in the velocity. In the downstream direction ( $y/D > 0$ ), there is some positive  $w$ -velocity near the ground which may be related to the lift-off of the vortex ring, as seen in the three-dimensional perspective.

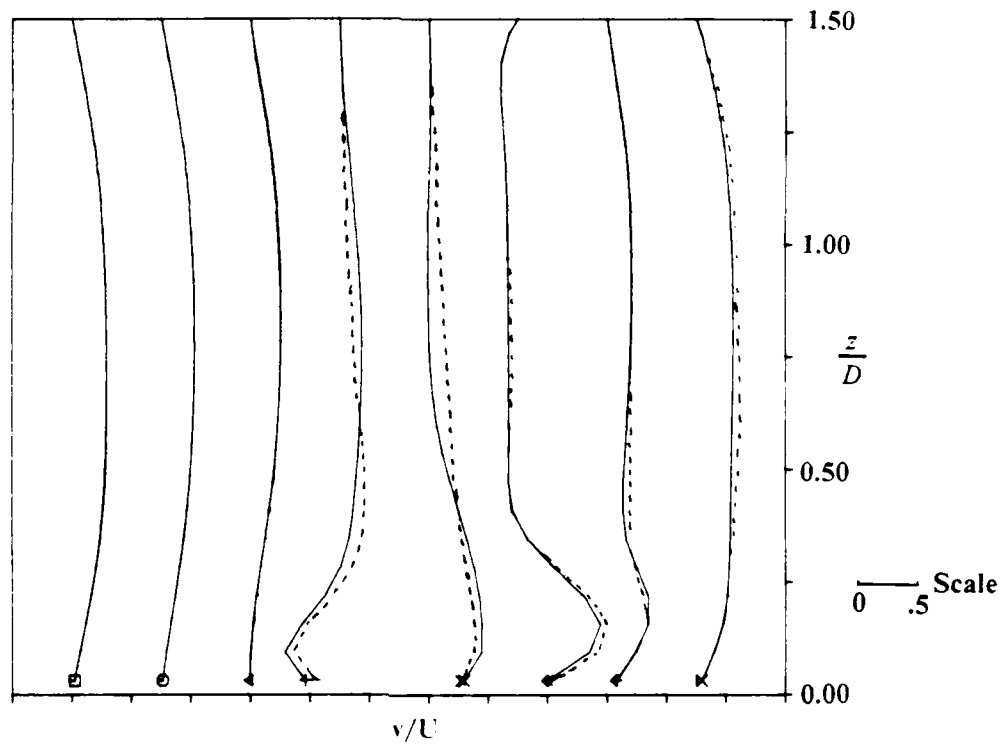
Finally, Figure 29 compares the wall pressure distribution in the  $y$ - $z$  plane at  $x = 0$  for the forcing case to that for the normal impingement case (Section 5.2). The peak pressure at the stagnation point for the case with crossflow is shifted downstream of the normal impingement case. The peak values are slightly affected by the forcing. Near  $y/D = -0.2$ , there is an increase in the pressure. Comparison with the velocity vector figures indicates that this increase is related to the recirculation region seen ahead of the impinging jet. The pressure is higher in the upstream region ( $y/D < 0$ ) when compared to the downstream region ( $y/D > 0$ ). This is partly due to the slowdown of the crossflow as the jet is reached, resulting in an adverse pressure gradient in the region  $y/D < 0$ , whereas downstream of the jet impingement region, the crossflow velocity component is added to the wall jet.

#### 5.4 The Normal Impinging Jet in Crossflow with Moving Ground Plane

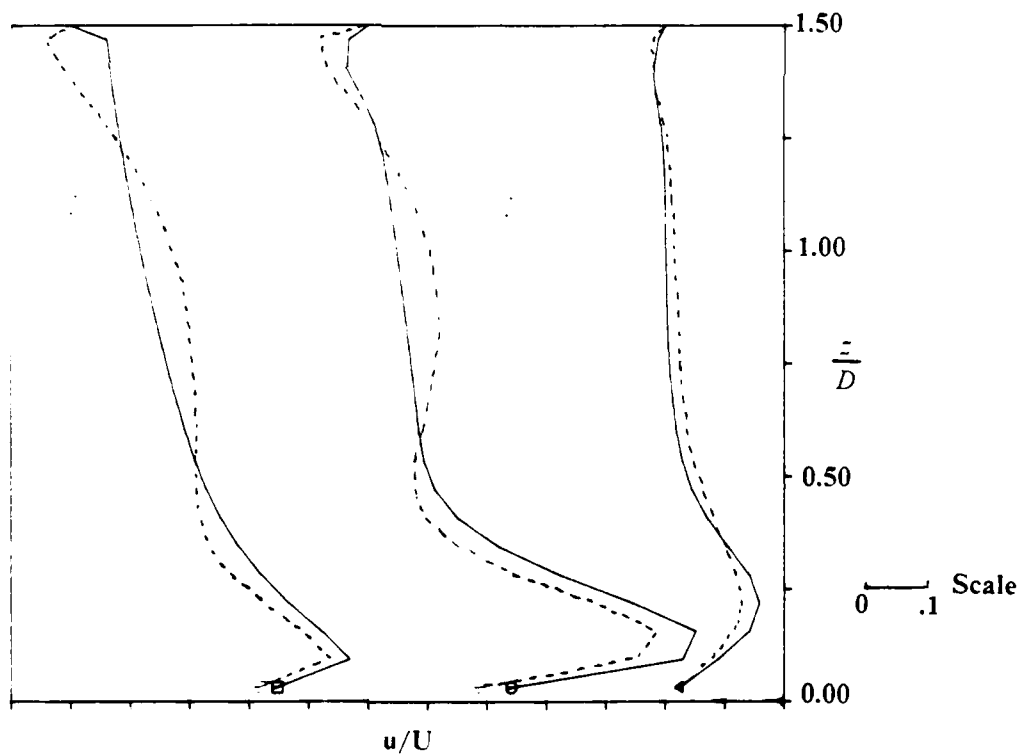
A simulation was also carried out for the case when the ground plane is also moving at the same speed as the incoming crossflow. As mentioned before, this is more representative of a V/STOL aircraft in forward motion. The cases discussed in Section 5.3 correspond more closely to the case of an experimental study in a wind tunnel where the ground plane is fixed. As reported in the literature, there are some significant differences between the two cases that must be taken into account before the wind tunnel data can be utilized to describe the effects of crossflow in actual flight situations.

The simulation performed in this case paralleled the case discussed in Section 5.3.1, in which the crossflow was begun after the jet had impinged on the ground. The results were acquired at the same time as in Section 5.3.1 so that a direct comparison of the differences in the flow field can be made.

The major difference is expected to be near the wall region since in the present case the ground moves with the same velocity as the crossflow and thus no wall boundary layer is present. We must point out that only preliminary conclusions can be derived from this study since the low grid resolution near the wall precludes detailed analysis of the flow there. High-resolution simulations must be performed for the cases described in Section 5.3.1 and in this section before the details of the differences can be understood. As shown below, however, even with low-resolution computations, significant differences are observed that are in remarkable agreement with experimental observations.

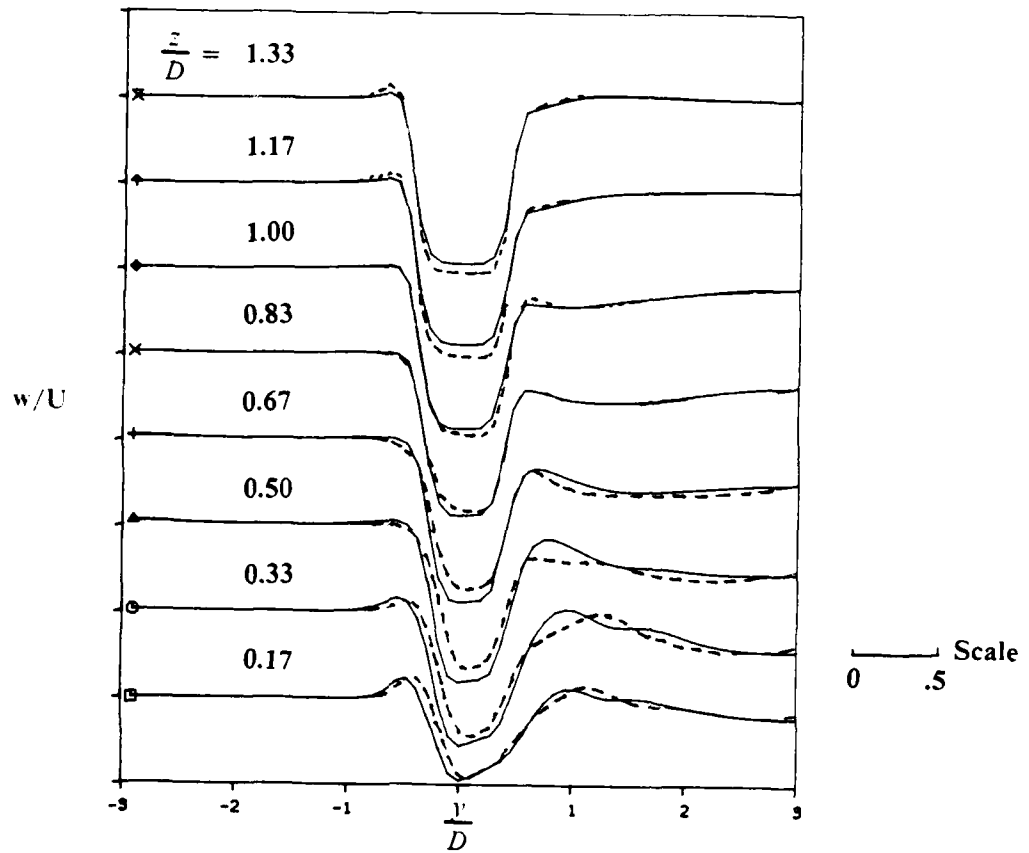


a.  $v$ -velocity profiles in the  $y-z$  plane at  $x = 0$ .



b.  $u$ -velocity profiles in the  $x-z$  plane at  $y = 0$ .

Figure 28. The velocity profiles in the flow field for the forced normal impinging jet with crossflow (case B). - - -  $t = 10.8$  —  $t = 12.2$



c.  $w$ -velocity profiles in the  $y$ - $z$  plane at  $x = 0$ .

Figure 28. The velocity profiles in the flow field for the forced normal impinging jet with crossflow (cont.). ---  $t = 10.8$  —  $t = 12.2$

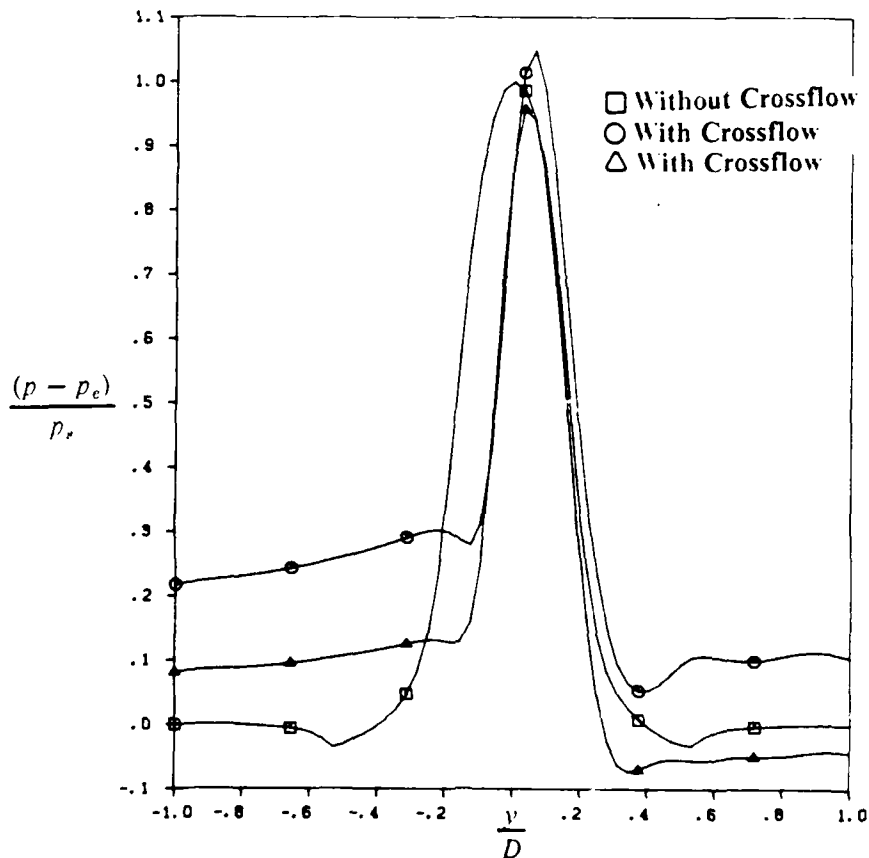


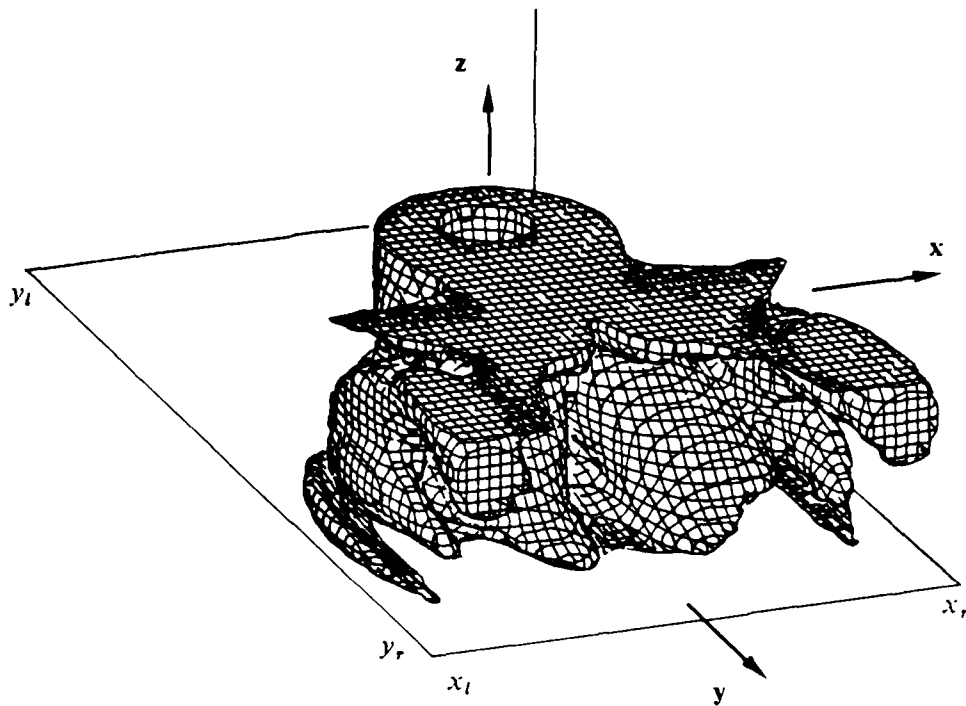
Figure 29. The ground pressure variation for the forced normal impinging jet with crossflow (case B). □  $t = 9.4$  ○  $t = 10.8$  △  $t = 12.2$

Figure 30a shows the three-dimensional vorticity field for the case with a moving wall at the same instant shown in Figure 18a and using the same vorticity level and viewing angle. Figures 30b and 30c show the  $|\omega_x|$  and  $|\omega_y|$  components, respectively, for the moving wall case. Comparison with the earlier simulation without the moving wall (Figure 18) reveals significant differences. Note that the "star-shaped" vorticity on the top is related to the vorticity on the top wall. As expected, there is very little vorticity present in the near wall region due to the wall motion. The vortex ring in the wall jet seen in the earlier simulation without a moving wall is no longer present. The spreading of the impinging jet shear layer now shows a two-lobed structure. The character of the fountain is also changed significantly. For example, the  $|\omega_y|$  component shows that the structures in the fountain are pushed farther in the positive  $y$ -direction and the vortical regions in the fountain do not extend to the ground. This is understandable, since there is no viscous boundary layer on the ground and thus the "inviscid" wall layer acts as a boundary for the vorticity in the flow field.

Figure 31a shows the  $x$ -vorticity in the  $y$ - $z$  plane at  $x = 0$ . Figure 31b shows the corresponding velocity vector field. Comparison with the earlier simulation without the moving wall (Figures 19a and 20a, respectively) shows that the effect of the moving wall is to reduce the vortical structure ahead of the jet. The jet shear layer bends by approximately the same amount even with the moving wall. This is understandable because the dynamics of the impinging jet should not be significantly affected by the moving wall except in the near wall region. Furthermore, there is no vorticity in the wall region due to the absence of the wall boundary layer. The velocity vector field clearly shows that there is no wall boundary layer present and that the recirculating region ahead of the impinging jet is reduced in size considerably. This is exactly the observation made in the experimental studies, where it was shown that, in the symmetry plane, the vortex ahead of the impinging jet is reduced by about 30 percent due to the moving wall.<sup>28</sup> The present computations indicate a good agreement with this experimental observation. Figure 31c shows the velocity vector field in the  $y$ - $z$  plane at  $x/D = 1.5$ . There is clearly an inviscid layer present near the wall, in contrast to the wall boundary layer seen when the wall was not moving. This inviscid layer acts as a boundary in the plane of the fountain and, as mentioned earlier, does not allow the fountain to evolve in the near wall region.

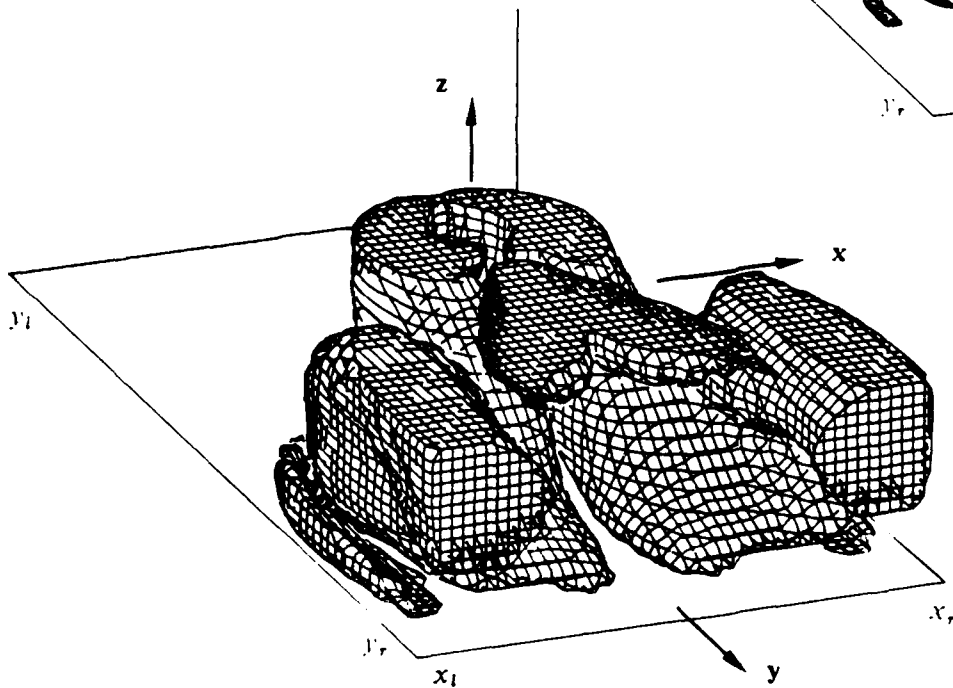
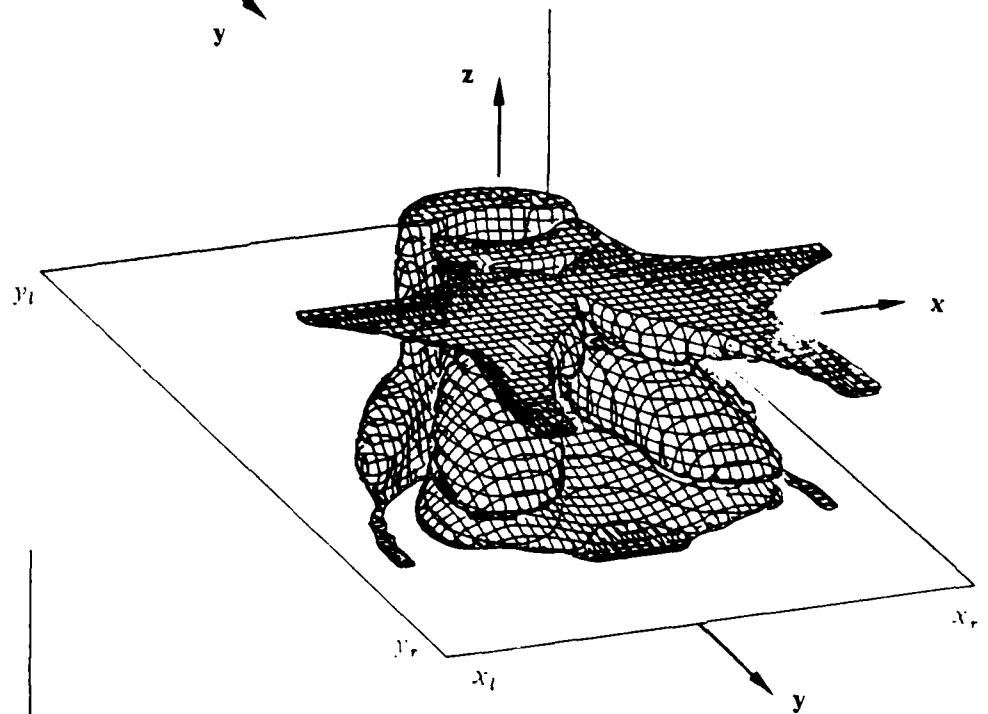
Figures 32a and 32b show the  $y$ -vorticity contours in the  $x$ - $z$  plane at  $y = 0$  and  $y/D = 1.5$ , respectively. In comparing these figures with the equivalent figures without the moving wall (Figures 19b and 19c), it is clear that there is no vortical structure in the fountain axis at  $y = 0$ . This is due to the fact that the fountain is pushed farther downstream due to the motion of the inviscid layer. This was also seen in Figure 30. The vortical structures in the  $y/D = 1.5$  plane are more complex with the moving wall. The core of the vortex in the fountain is now closer to the wall, as seen on the right side of this figure. The structure on the left is the image of the vortical layer behind the impinging jet and is associated with the spreading observed in Figure 30. Note that there is some positive  $\omega_y$  vorticity between the two structures. This is possibly due to the wall inviscid layer being engulfed by the vortical motions in the fountain region and the jet shear region.

Figures 32c and 32d show the corresponding velocity vector fields in the  $y$ - $z$  plane at  $y = 0$  and  $y/D = 1.5$ , respectively. The velocity field in the  $y = 0$  plane shows negligible upward motion in the fountain, and there are no significant indications of the wall jet near the ground wall. This is again a result of the wall motion in the  $y$ -direction, which causes the flow field in the near wall region to move primarily in the positive  $y$ -direction. In the  $y/D = 1.5$  plane, the recirculation due to the vortical motion seen in Figure 32b can be seen. There is some fluid motion to the fountain region (i.e.,  $x/D = 1.5$ ) near the wall, but it is relatively quite weak.



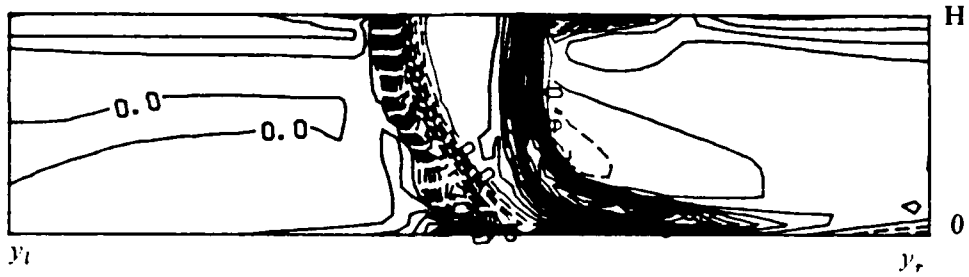
a.  $3D|\omega|$  at a level of 1.3

b.  $3D|\omega_x|$  at a level of 1.0

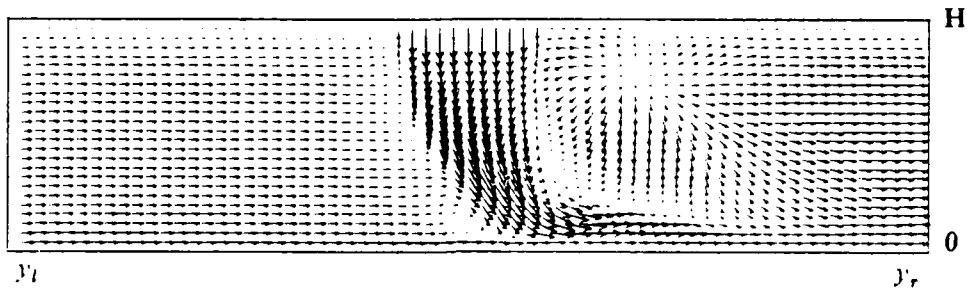


c.  $3D|\omega_y|$  at a level of 0.75

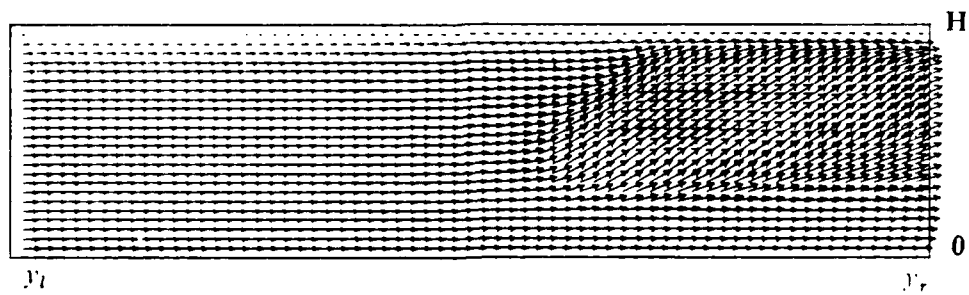
Figure 30. The three-dimensional perspective of the vorticity field for the normal impinging jet with crossflow and with the moving ground plane at  $t = 13.1$ .



a.  $x$ -vorticity contours at  $x = 0$ . Contour interval is 0.5.



b. Velocity vector field at  $x = 0$ .



c. Velocity vector field at  $x/D = 1.5$ .

Figure 31. The vorticity and velocity fields in the  $y-z$  plane for the normal impinging jet with crossflow and with the moving ground plane at  $t = 13.1$ .

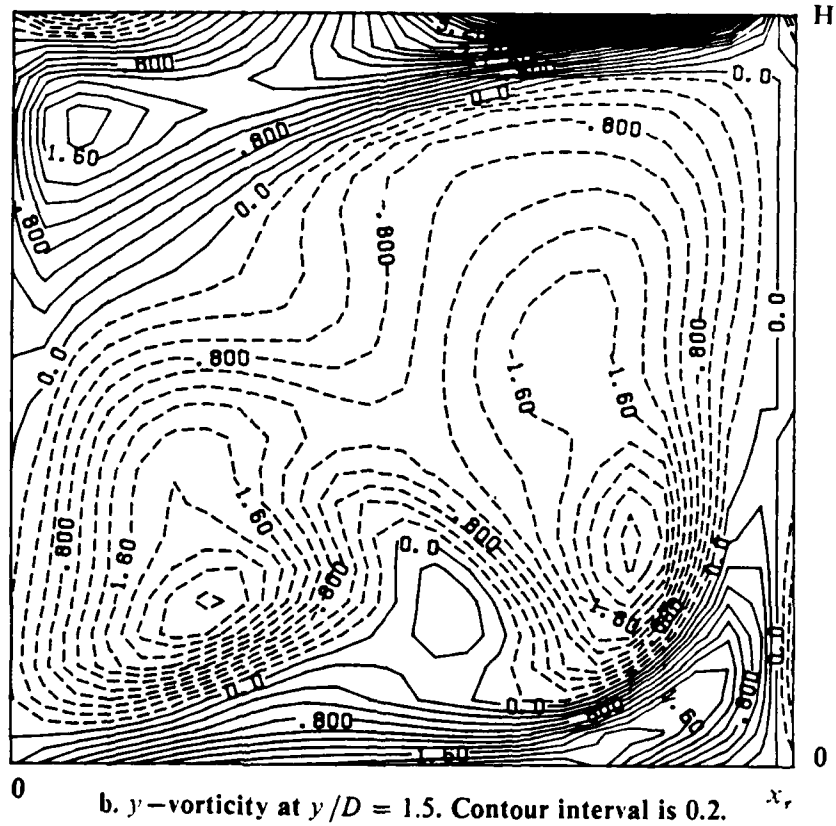
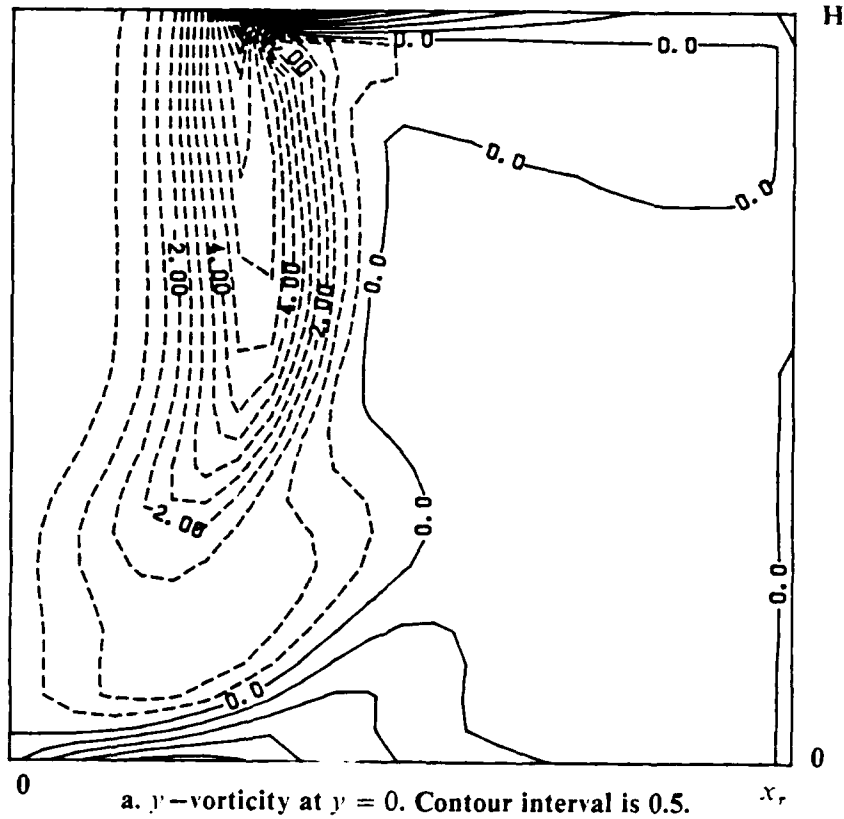
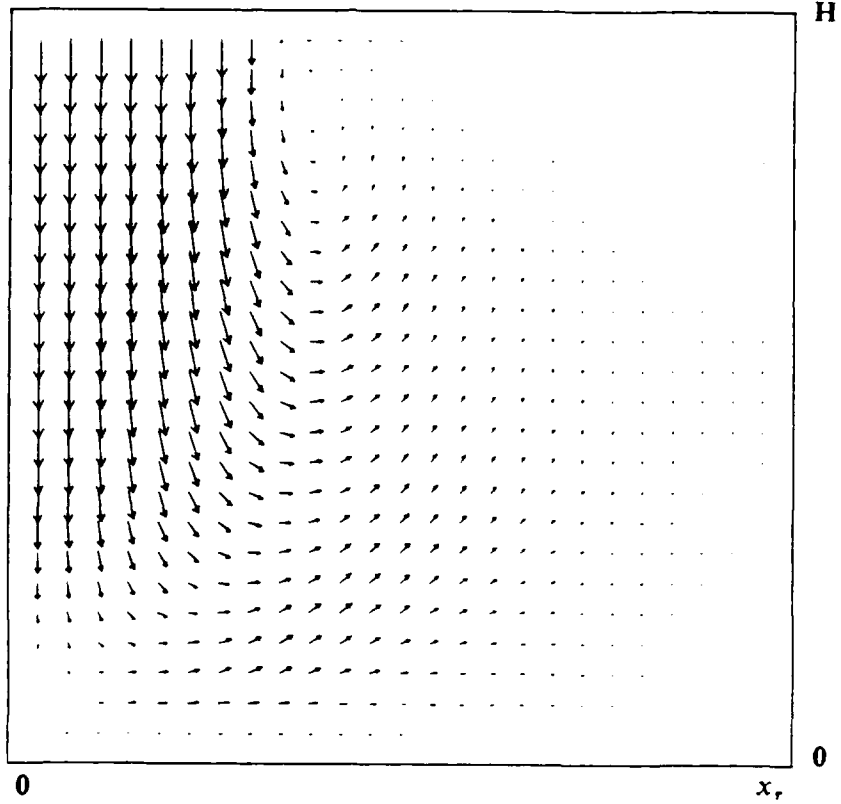
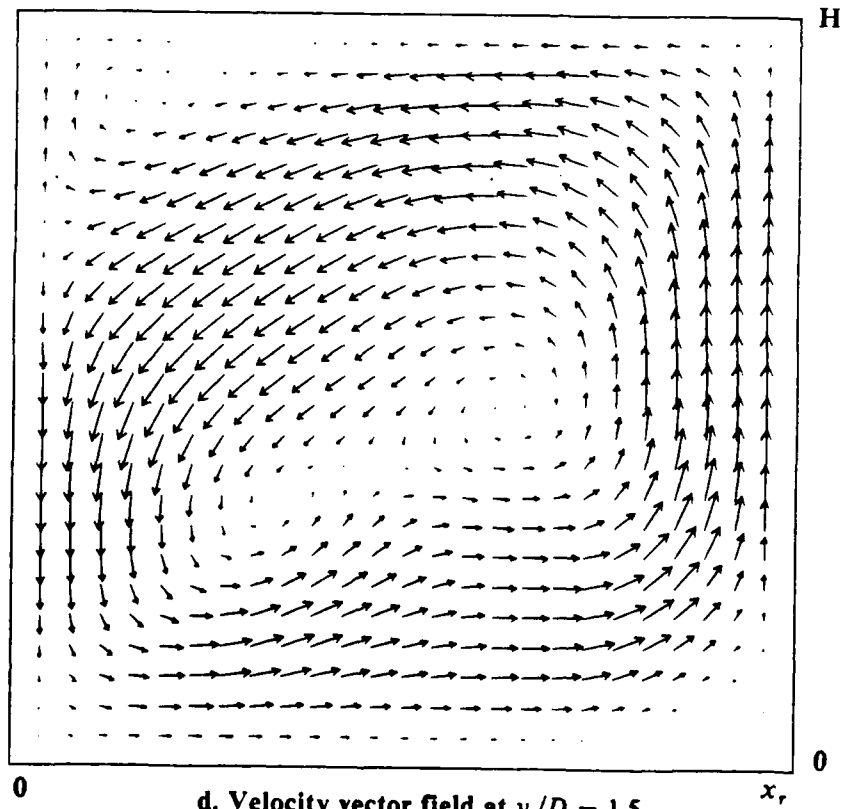


Figure 32. The vorticity and velocity fields in the  $x-z$  plane for the normal impinging jet with crossflow and with the moving ground plane at  $t = 13.1$ .



c. Velocity vector field at  $y = 0$ .



d. Velocity vector field at  $y/D = 1.5$ .

Figure 32. The vorticity and velocity fields in the  $x-z$  plane for the normal impinging jet with crossflow and with the moving ground plane at  $t = 13.1$  (cont.).

Figures 33a and 33b show the pressure contours on the top and bottom walls, respectively. There is a low-pressure region on the top wall in the jet shear layer, and the effect of crossflow is to spread the pressure contours. Note that the pressure increases in the plane of the fountain but the high pressure is shifted further toward the outflow ( $y/D > 2$ ). This is the region where the fountain reaches the top wall, and the shift downstream is due to the crossflow. The pressure contours on the bottom wall show that the stagnation pressure occurs downstream of the  $y = 0$  location by about  $0.28D$ , and again the compression effect of the crossflow can be seen. There is a low-pressure region behind the jet.

Figure 34 shows typical velocity profiles in the flow field. The velocity profiles for the case with a nonmoving wall (Section 5.3.1) at the same time is also shown in these figures to allow a direct comparison and interpretation of the effect of a moving wall. Figure 34a shows the  $v$ -velocity profiles in the  $y$ - $z$  plane at  $x = 0$ . The lack of a wall boundary layer for the moving wall case can be clearly seen in this figure. Further away from the wall, the motion in the positive  $y$ -direction is not affected significantly by the moving wall. Figure 34b shows the  $u$ -velocity profiles in the  $x$ - $z$  plane at  $y = 0$ . As mentioned earlier, the moving wall causes significant motion toward the outflow in the  $y$ -direction. Thus, the wall jet region in the direction of the fountain axis is quite weak. Another result is that there is no significant upwash, which in turn results in a reduced reverse flow on the top wall.

Figure 34c shows the  $w$ -velocity profiles in the  $y$ - $z$  plane at  $x = 0$ . The impinging jet is not affected significantly by the moving wall, and the sweepback of the jet due to crossflow occurs in nearly the same manner as without a moving wall. Ahead of the jet, however, there was significant upwash (positive  $w$ -velocity) for the nonmoving wall case, which was shown earlier to be associated with the vortex ahead of the jet. The moving wall case, on the other hand, shows much smaller upward motion, and this upwash is also located closer to the jet itself. This reduced motion is related to the smaller vortical structure and recirculation seen in earlier figures and is consistent with experimental observations.

Finally, Figure 35 shows the wall pressure distribution in the  $y$ - $z$  plane at  $x = 0$  for three cases. The normal impingement case and the nonmoving wall case are compared in this figure with the moving wall case. The location of the peak stagnation pressure on the wall with crossflow occurs at almost the same location with and without the moving wall. In general, the pressure variation on the wall is not significantly affected by the moving wall.

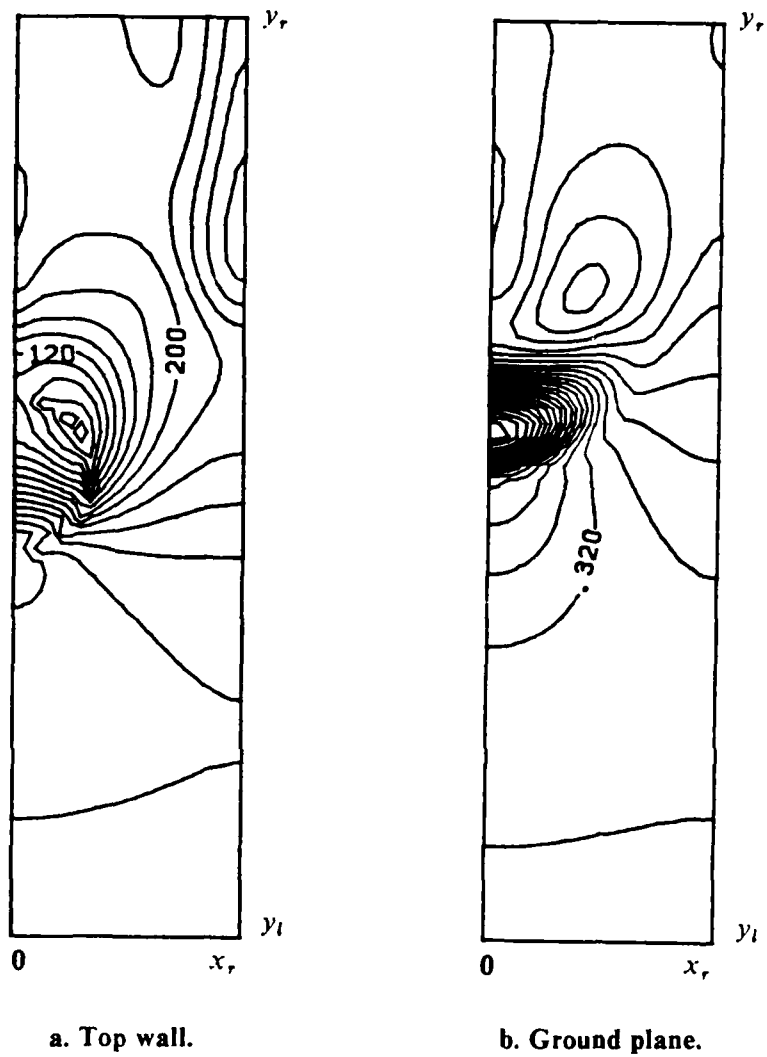
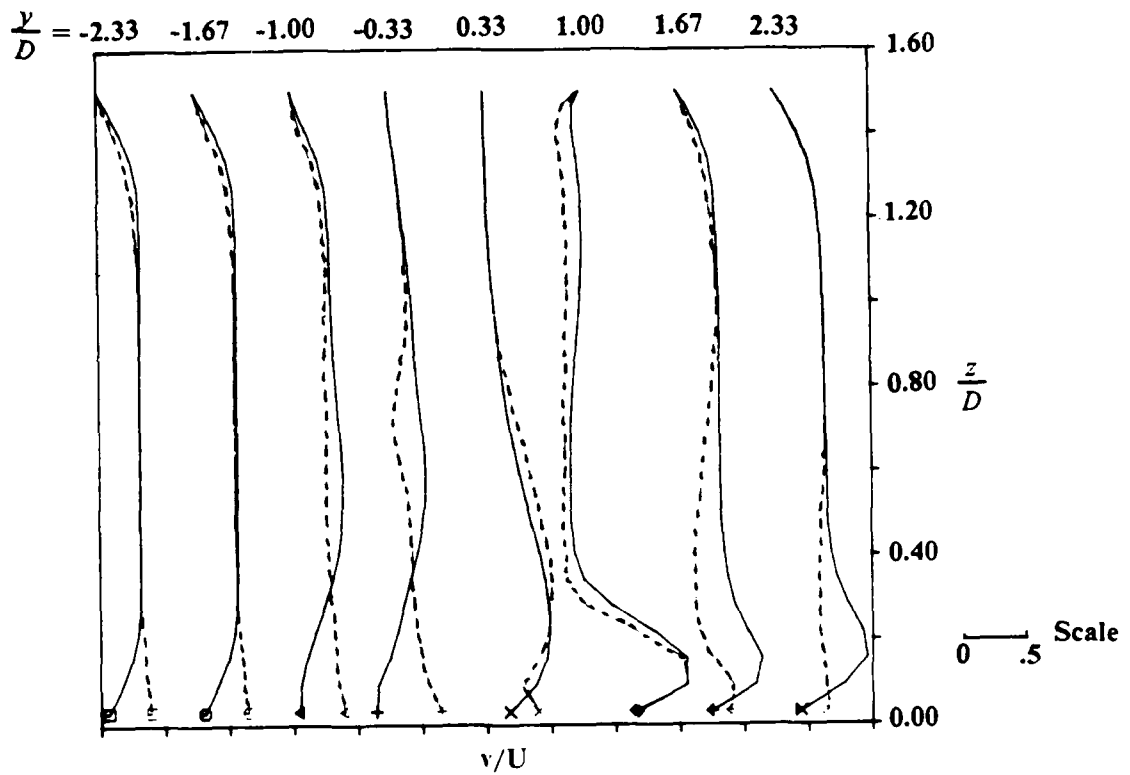
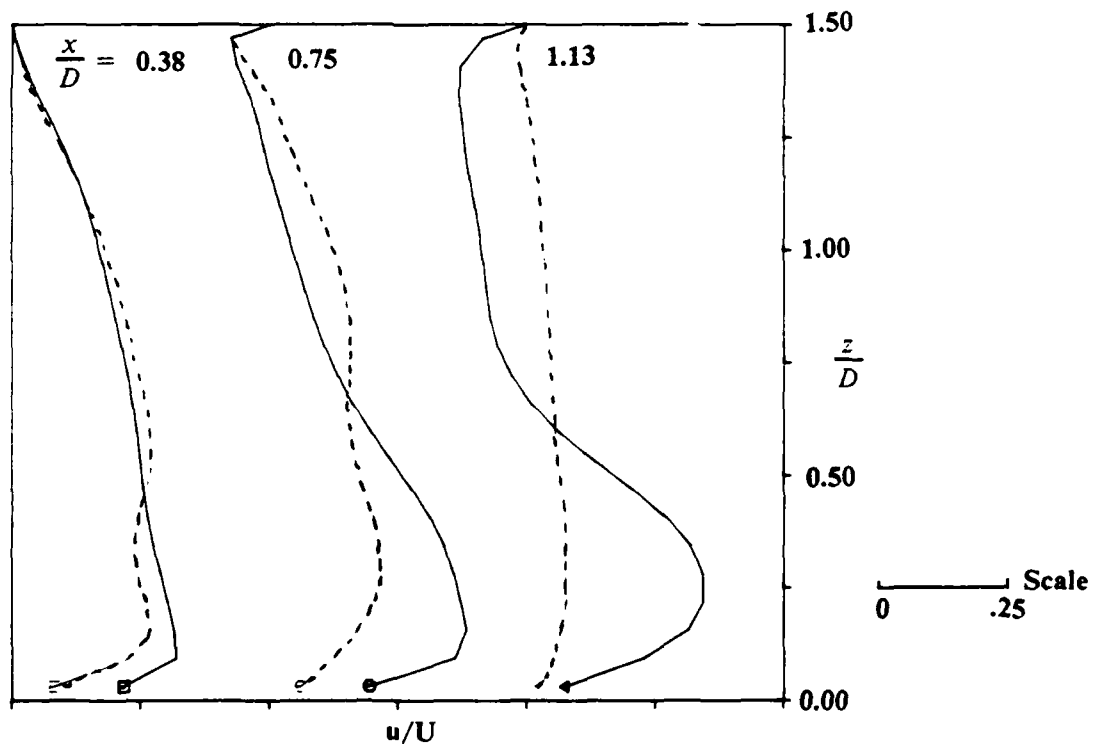


Figure 33. The pressure contours in the  $x$ - $y$  plane for the normal impinging jet with crossflow and with the moving ground plane at  $t = 13.1$ . Contour interval is 0.02.



a.  $v$ -velocity profiles in the  $y-z$  plane at  $x = 0$ .



b.  $u$ -velocity profiles in the  $x-y$  plane at  $y = 0$ .

Figure 34. The comparison between the velocity profiles for the cases with and without the moving ground plane for the normal impinging jet with crossflow at  $t = 13.1$ .

— With Crossflow (Case A)      - - - With Crossflow and moving ground

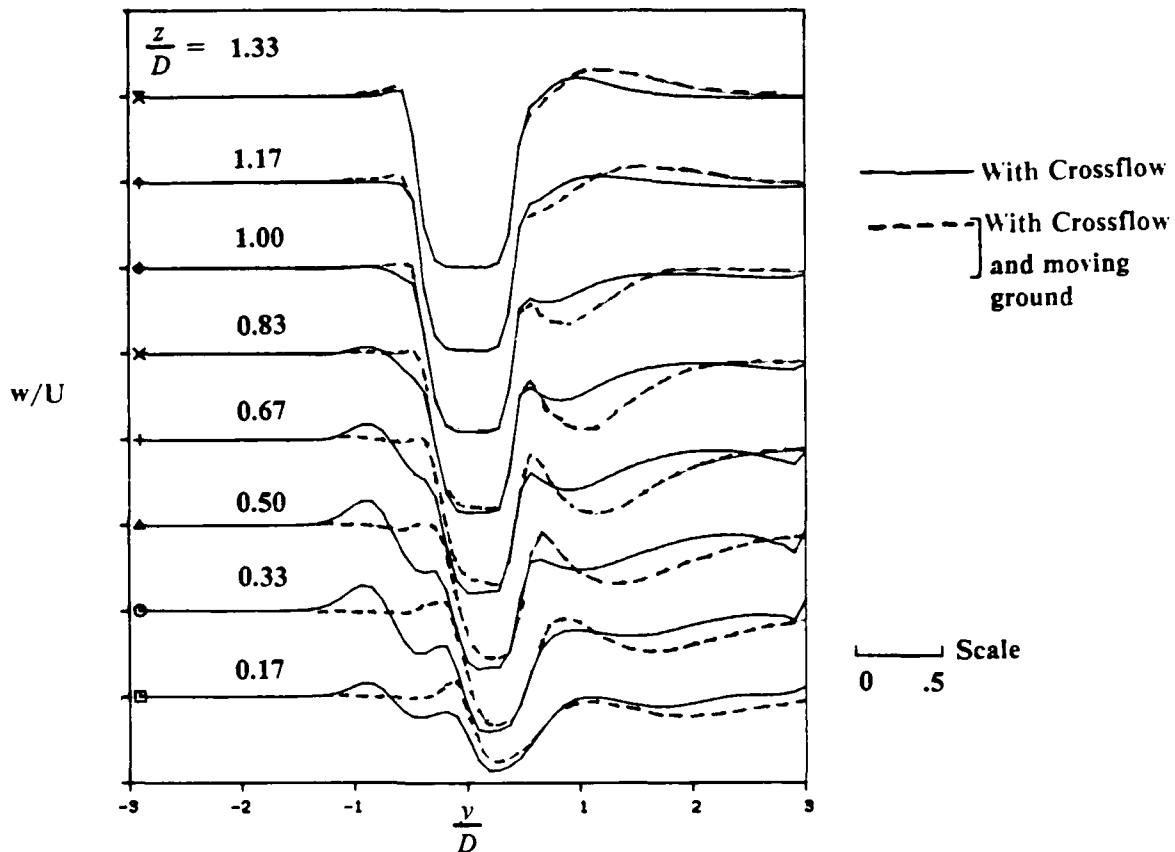


Figure 34. (cont.) c.  $w$ -velocity profiles in the  $y$ - $z$  plane at  $x = 0$ .

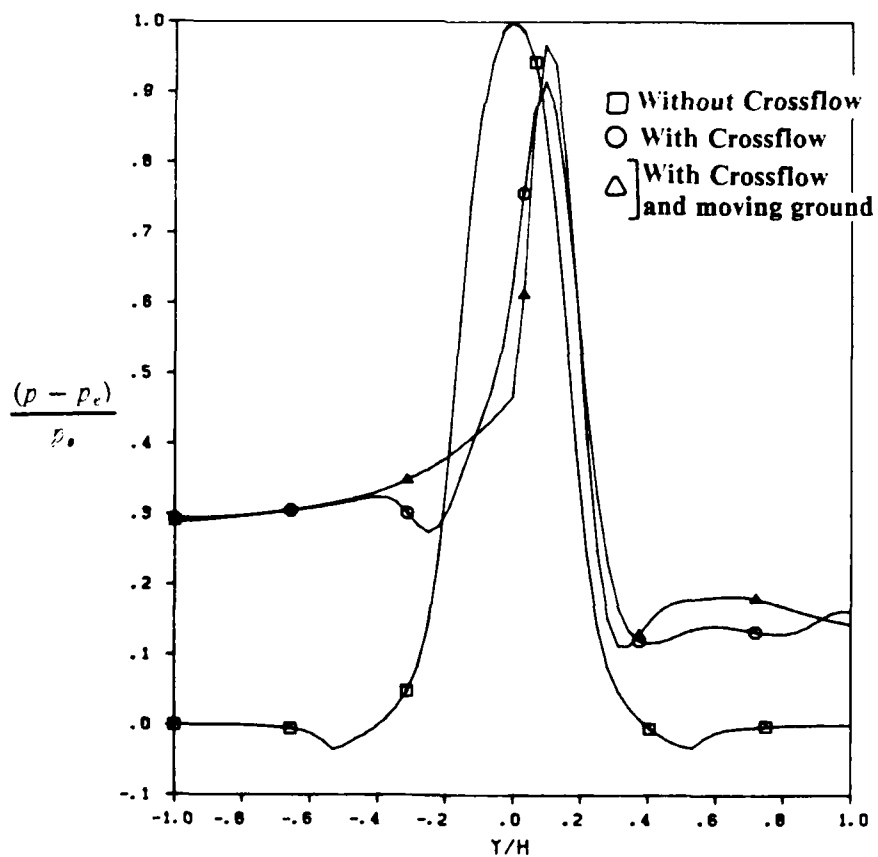


Figure 35. The comparison between the ground pressure variation for the cases with and without moving ground plane for the normal impinging jet with crossflow at  $t = 13.1$ .

## 6. CONCLUSIONS AND RECOMMENDATIONS

This report presents the results of large-eddy simulations of various flow fields associated with impinging jets. The results clearly indicate that the primary technical objectives of the Phase I study have been successfully achieved. The original LES code for studying normal impinging jets was successfully modified to simulate inclined jets, normal impinging jets in crossflow, and normal impinging jets in crossflow with a moving ground plane. Thus, we now have a simulation capability that can be used to study the detailed dynamics of fluid motion associated with various flight configurations of a V/STOL aircraft in ground effect. These modifications were accomplished in such a manner that the combination of various flight situations can also be simulated. For example, a V/STOL aircraft in pitch while in transition from hover to forward motion can also be simulated.

Other interesting situations that can be simulated are the effects of forward acceleration while moving from hover to climb, and of forward deceleration while in transition from forward motion to hover. Another possible configuration is an aircraft undergoing an unsteady pitching motion. The modifications carried out in Phase I were made to take these features into account. Although these flight situations were not simulated in this Phase I study, the success of the present computations leaves no doubt of the possibility of studying flow fields associated with such complex flight configurations. It is worth pointing out here, however, that these highly unsteady V/STOL motions occur at very high frequency, whereas the large-scale vortical motion occurs at much lower frequency. Therefore, parametric variation of the impingement angle or the forward speed will probably be sufficient to understand the complex dynamics of the fluid flow. Thus, the LES capability demonstrated in this Phase I study may provide a new numerical "experimental" tool that can be utilized to understand the dynamics of the flow field in a systematic manner.

The basic numerical scheme was used in earlier studies to investigate the effect of coherent and random excitation of normal impinging jets. The results were shown to agree quite well with experimental observations and thus the validity of the basic code was demonstrated. In the present Phase I study, only coarse mesh calculations were possible due to resource limitations. However, the grid was chosen so that some comparison with experimental data could be accomplished. The results presented in this report clearly demonstrate that this LES code is capable of reproducing features in the flow field that are in good qualitative agreement with some of the experimental observations.

The approach taken in this study was to investigate the motion of large-scale structures in the flow field by exciting the impinging jet at a prescribed frequency in the jet preferred range. This ensures that the large structures generated in the impinging jet will be controlled by the forcing frequency and that the natural instability of the flow will be suppressed, resulting in a "clean" numerical experiment.

The simulation of the inclined impinging jet showed some good agreement with experimental observations. The oblique impingement causes a significant portion of the jet fluid to be transported in the direction of inclination. Theoretical estimates indicate that about 80 percent of the mass is transported in the forward direction.<sup>15,17</sup> The jet impingement point is behind the jet center line for the oblique impingement case, which is in agreement with experimental observations. In addition, the shift forward from the center ( $y = 0$ ) location for the normal impingement case was also determined to agree closely with the experimental value. It was also demonstrated that the stagnation streamline for the oblique impingement case has nonzero vorticity in contrast to the nonrotational stagnation streamline for the normal impingement case. This agreed with past experimental and theoretical observations.<sup>17,18</sup>

The effect of forcing is that large coherent vortical rings are shed at the forcing frequency. The phase speed of these structures in the jet was estimated to be around  $0.6U$ , which again agrees with experimental values.<sup>3</sup> The presence of the fountain formed by the collision of the wall jets changes the dynamics of the structures in the wall region, as was observed earlier in the normal impinging jet studies. The fountain is skewed in the direction of inclination, which would result in a nonsymmetric upwash and consequently an unequal lift-off effect on the top wall.

The effect of crossflow with and without a moving wall was also studied, and the results are again in agreement with some experimental observations. For example, the experimentally observed<sup>4</sup> formation of counterrotating structures behind the impinging jet was also numerically computed. However, it was shown that the effect of the proximity of the fountain (which is absent in most of the experimental studies) can modify the dynamics of the vortical motion significantly. The streamline compression ahead of the jet due to crossflow was also demonstrated and was in qualitative agreement with experimental observations.

The impinging jet acts as an obstacle to the crossflow, causing the crossflow to go around it. The ring vortex ahead of the impinging jet is pushed back and significant three-dimensional vortex stretching occurs due to crossflow. The total vorticity in the flow field is redistributed in a very complex manner, as was also determined in experimental studies.<sup>4,41</sup> However, this redistribution is quite different if the fountain is formed (Section 5.3.1) as compared to the case when the crossflow is initiated before the fountain is formed (Section 5.3.2). More detailed and long-time simulations are necessary to evaluate the dynamics of the large-scale motion under crossflow. These aspects will be considered in more detail in the next phase.

The effect of allowing the ground plane to move is that the wall boundary layer is absent and an inviscid layer is present close to the wall. This results in the reduction of the vortex size and strength ahead of the impinging jet, which again agrees with experimental observations.<sup>27,28</sup> The computations of impinging jets in crossflow with a moving ground plane presented in this study appear to be the first attempt to numerically simulate these flow fields. The preliminary results obtained indicate good qualitative agreement with experimental observations.

In conclusion, the LES capability developed and demonstrated in this Phase I study clearly shows that all the technical objectives of the study have been successfully achieved. The numerical code can now simulate a variety of V/STOL flight situations in ground effect. These include pitch up or down, forward motion at a steady velocity and under forward acceleration/deceleration. The effect of the moving ground plane can also be modeled by the LES code. The jet-to-ground distance and the lateral spacing between the impinging jets can also be varied to study the effects of lift-off and the dynamics of the fountain. Most of these configurations can also be combined to study realistic V/STOL flight in ground effect. For example, an actual flight profile of the V/STOL near the ground may be composed of a lift-off from the ground, a pitch-up followed by a rapid acceleration to a constant velocity with which the aircraft would climb out of ground effect. The LES code demonstrated in this Phase I study can be used to study most of this flight profile in a spatially and temporally accurate manner. The dynamics of large-scale vortical structures in the impinging jets, the wall jets and in the fountain can be evaluated as demonstrated here.

Further simulations using high grid resolution are required to understand the various features of the complex flow field associated with V/STOL flows, especially at high Reynolds numbers. The effect of varying the jet-to-ground distance,  $H$ , and the spacing between the impinging jets must also

be evaluated since these parameters control the dynamics of the fountain, which in turn controls the lift-off effect on the V/STOL aircraft. Another important aspect of V/STOL aircraft in ground effect is the entrainment of dust from the ground, which can be reingested into the engine intakes and possibly cause engine malfunctions. In principle, by linking a "particle tracking" algorithm to the LES code, it would be possible to study the motion of "particles" injected from the ground in order to better understand the entrainment mechanism. These aspects can be considered in the next phase.

Finally, it must be emphasized that the large-eddy simulation technique provides all the flow variables of interest, including properties such as vorticity, which is difficult, if not impossible, to measure experimentally. In principle, with proper data management, these properties can be recorded in the entire computational domain for the entire time length of the simulation. Thus, additional information such as the turbulent kinetic energy and Reynolds stress variations in the flow field can be computed, as demonstrated in an earlier study.<sup>10</sup> The temporal record of the velocity and pressure fluctuations in the flow can also be used for spectral analysis, which can provide additional information on the frequency content of the fluctuations. Detailed analysis of the computed results and comparison with experimental data can then be carried out, as will be proposed for the next phase.

## REFERENCES

1. NASA SP-218, "Analysis of a Jet in a Subsonic Crosswind," Proc. of Symposium, NASA Langley Research Center, Sept. 9-10, 1969.
2. Kuhn, R. E., "V/STOL and STOL Ground Effects and Testing Techniques," NASA Conference Publication No. 2462, pp. 1-145, August, 1985.
3. Didden, N. and Ho, C.-M., "Unsteady Separation in a Boundary Layer Produced by an Impinging Jet," *J. Fluid Mech.*, Vol. 160, November 1985.
4. Andreopoulos, J. and Rodi, W., "Experimental Investigation of Jets in Crossflow," *J. Fluid Mech.*, Vol. 138, pp. 93-127, 1984.
5. Donaldson, C. D. and Snedeker, R. S., "A Study of Free Jet Impingement: Part I - Mean Properties of Free and Impinging Jets," *J. Fluid Mech.*, Vol. 45, pp. 281-319, 1971.
6. Ho, C.-M. and Nasseir, N. S., "Dynamics of an Impinging Jet, Part I: The Feedback Phenomenon," *J. Fluid Mech.*, Vol. 105, pp. 119-142, 1981.
7. Nasseir, N. S. and Ho, C.-M., "Dynamics of an Impinging Jet, Part 2: Noise Generation," *J. Fluid Mech.*, Vol. 116, pp. 379-391, 1982.
8. Gutmark, E., Wolfshtein, M., and Wagnanski, I., "The Plane Turbulent Impinging Jet," *J. Fluid Mech.*, Vol. 88, pp. 737-756, 1978.
9. Rizk, M. R. and Menon, S., "Large-Eddy Simulations of Axisymmetric Excitation Effects on a Row of Impinging Jets," *Phys. Fluids*, Vol. 31, pp. 1892-1903, 1988.
10. Menon, S. and Rizk, M. R., "Large-Eddy Simulations of Three-Dimensional Forced Impinging Jets: Azimuthal and Random Excitation Effects," to be submitted to *Phys. Fluids*, 1989.
11. Foss, J. F. and Kleis, S. J., "Mean Flow Characteristics for the Oblique Impingement of an Axisymmetric Jet," *AIAA J.*, Vol. 14, pp. 705-706.
12. Siclari, M. J., Hill, W. G. Jr., and Jenkins, R. C., "Stagnation Line and Upwash Formation of Two Impinging Jets," *AIAA J.*, Vol. 19, pp. 1286-1293, 1981.
13. Schach, W., "The Deflection of a Free Liquid Jet on a Flat Plane," *Ingenieur-Archiv*, Vol. 5, pp. 245-265, 1934.
14. Taylor, G., "Formation of Thin Flat Sheets of Water," *Proc. Roy. Soc. A.*, Vol. 254, pp. 1-17, 1960.
15. Taylor, G., "IV. Oblique Impact of a Jet on a Plane Surface," *Phil. Trans. Roy. Soc. (London)*, Vol. 260A, pp. 965-100, 1966.
16. Rubel, A., "Computations of the Oblique Impingement of Round Jets Upon a Plane Wall," *AIAA J.*, Vol. 19, pp. 863-871, 1981.
17. Rubel, A., "Oblique Impingement of a Round Jet on a Plane Surface," *AIAA J.*, Vol. 20, pp. 1756-1758, 1982.
18. Hayes, W. D., "Rotational Stagnation Point Flow," *J. Fluid Mech.*, Vol. 19, pp. 366-374, 1964.

19. Keffer, J. F. and Baines, W. D., "The Round Turbulent Jet in a Crosswind," *J. Fluid Mech.*, Vol. 15, pp. 481-496, 1963.
20. Kamotani, Y. and Greber, I., "Experiments on a Turbulent Jet in a Cross Flow," *AIAA J.*, Vol. 10, pp. 1425-1429, 1972.
21. Patanker, S. V., Basu, D. K., and Alpay, S. A., "Prediction of the Three-Dimensional Velocity Field of a Deflected Turbulent Jet," *J. Fluid Engg.*, pp. 758-762, 1977.
22. Crabb, D., Durao, D. F. G., and Whitelaw, J. H., "A Round Jet Normal to a Crossflow." *J. Fluid Engg.*, Vol. 103, pp. 142-153, 1981.
23. Claus, R. W., "Analytical Calculation of a Single Jet in Crossflow and Comparison with Experiments," AIAA-83-0238, 1983.
24. Wu, J. M., Vakili, A. D., and Yu, F. M., "Investigation of the Interacting Flow of Non-Symmetric Jets in Cross Flow," AIAA Paper No. 86-0280, 1986.
25. Cimbala, J. M., Stinebring, D. R., Treaster, A. L., and Billet, M. L., "Experimental Investigation of a Jet Impinging on a Ground Plane in the Presence of a Crossflow," NADC Report 87019-60, March 1987.
26. Barata, J., Durao, D., and McGuirk, J., "Numerical Study of Single Impinging Jets through a Crossflow," AIAA Paper No. 89-0449, 1989.
27. Kemmerly, G. T., Paulson, J. W. Jr., and Compton, M., "Exploratory Evaluation of a Moving Model Technique for Measurement of Dynamic Ground Effects," *J. of Aircraft*, Vol. 25, pp. 557-562, 1988.
28. Stewart, V. and Kemmerly, G. T., "Characteristics of the Ground Vortex Formed by a Jet Moving over a Fixed Ground Plane," AIAA Paper No. 89-0650, 1989.
29. Rizk, M. R. and Menon, S., "Large-Eddy Simulations of Axisymmetric and Azimuthal Excitation Effects on a VTOL Upwash Fountain," accepted for publication in *Phys. Fluids*, 1989.
30. Smagorinsky, J., "General Circulation Experiments with the Primitive Equations," *Mon. Weather Rev.*, Vol. 19, pp. 99-164, 1963.
31. Deardorff, J. W., "A Numerical Study of Three-Dimensional Turbulent Channel Flow at Large Reynolds Numbers," *J. Fluid Mech.*, Vol. 41, pp. 453-480, 1970.
32. Spalding, D. B., "A Single Formula for the Law of the Wall," *J. Appl. Mech.*, Vol. 28, pp. 455-458, 1961.
33. Leonard, B. P., "A Stable and Accurate Convective Modeling Procedure Based on Quadratic Upstream Interpolation," *Computer Methods in Appl. Mech. and Eng.*, Vol. 19, pp. 59-98, 1979.
34. Davis, R. W. and Moore, E. F., "A Numerical Study of Vortex Shedding from Rectangles," *J. Fluid Mech.*, Vol. 116, pp. 475-506, 1982.
35. Crow, S. C. and Champagne, F. H., "Orderly Structure in Jet Turbulence," *J. Fluid Mech.*, Vol. 48, pp. 547-591, 1971.

36. Brown, G. L. and Roshko, A., "On Density Effects and Large Structure in Turbulent Mixing Layers," *J. Fluid Mech.*, Vol. 64, pp. 775-816, 1974.
37. Gutmark, E. and Ho, C.-M., "Preferred Modes and the Spreading Rates of Jets," *Phys. Fluids*, Vol. 26, pp. 2932-2938, 1983.
38. Chan, Y. Y., "Wavelike Eddies in a Turbulent Jet," *AIAA Journal*. Vol. 15, pp. 992-1001, 1977.
39. Zaman, K. B. M. Q. and Hussain, A. K. M. F., "Vortex Pairing in a Circular Jet Under Controlled Excitation: Part I - General Jet Response," *J. Fluid Mech.*, Vol. 101, pp. 449-491, 1980.
40. Batchelor, G. K. and Gill, E. A., "Analysis of the Stability of Axisymmetric Jets," *J Fluid Mech.*, Vol. 14, pp. 529-551, 1962.
41. Andreopoulos, J., "On the Structure of Jets in Crossflow," *J. Fluid Mech.*, Vol. 157, pp. 163-197, 1985.